Finite element methods for fourth order axisymmetric geometric evolution equations

John W. Barrett[a], Harald Garcke[b], Robert Nürnberg[a,*]

[a]*Department of Mathematics, Imperial College London, London, SW7 2AZ, UK*
[b]*Fakultät für Mathematik, Universität Regensburg, 93040 Regensburg, Germany*

Abstract

Fourth order curvature driven interface evolution equations frequently appear in the natural sciences. Often axisymmetric geometries are of interest, and in this situation numerical computations are much more efficient. We will introduce and analyze several new finite element schemes for fourth order geometric evolution equations in an axisymmetric setting, and for selected schemes we will show existence, uniqueness and stability results. The presented schemes have very good mesh and stability properties, as will be demonstrated by several numerical examples.

Keywords: surface diffusion, Willmore flow, Helfrich flow, finite elements, axisymmetry, tangential movement.

1. Introduction

The motion of interfaces driven by a law for the normal velocity, which involves the surface Laplacian of curvature quantities, plays an important role in many applications. The resulting differential equations are parabolic and of fourth order. Prominent examples are the surface diffusion flow, which models phase changes due to diffusion along an interface, see [39, 16]. In this evolution law the normal velocity of the interface is given by the surface Laplacian of the mean curvature.

Typical membrane energies involve the curvature of the membrane. In the simplest models the Willmore functional, which is just the integrated squared mean curvature, is an appropriate energy, see [46]. Recently, in particular, biomembranes have been the focus of research and in this case more complex energies, like the Canham-Helfrich energy, are of interest, see [17, 33, 42] for details. Taking the L^2–gradient flow of such an energy also leads to a fourth order geometric evolution equation involving the surface Laplacian of the mean curvature and cubic nonlinearities in the curvature, see [43, 36]. In the case of biological membranes also more complex laws, taking volume and surface constraints or a coupling to fluid flow into account, are of relevance, see [5, 9] and the references therein.

In this paper we introduce new numerical schemes for axisymmetric versions of these flows. This is a very relevant issue as in many situations axisymmetric shapes appear and reducing the computations to a spatially one-dimensional problem greatly reduces the computational complexity. Schemes for the axisymmetric problem also have the benefit that mesh degeneracies, which for other schemes frequently happen during the evolution, can be avoided. We will also introduce schemes which make use of the tangential degrees of freedom in order to obtain good mesh properties. Some of these schemes even have the property that mesh points equidistribute during the evolution.

We now specify the interface evolution laws studied in this paper in more detail. Let $(\mathcal{S}(t))_{t\geq 0} \subset \mathbb{R}^3$ be a family of smooth, oriented hypersurfaces, which we later assume to be axisymmetric. The mean curvature flow for $\mathcal{S}(t)$ is given by the evolution law

$$\mathcal{V}_S = k_m \qquad \text{on } \mathcal{S}(t),\tag{1.1}$$

and it is the L^2–gradient flow for for the surface area. Here $\mathcal{V}_S$ denotes the normal velocity of $\mathcal{S}(t)$ in the direction of the normal $\vec{n}_S$. Moreover, k_m is the mean curvature of $\mathcal{S}(t)$, i.e. the sum of the principal curvatures of $\mathcal{S}(t)$. For the methods derived in this paper the identity

$$\Delta_S \vec{\text{id}} = k_m \, \vec{n}_S \qquad \text{on } \mathcal{S}(t) \tag{1.2}$$

will be crucial, where Δ_S is the Laplace–Beltrami operator on $\mathcal{S}(t)$ and $\vec{\text{id}}$ denotes the identity function in $\mathbb{R}^3$. A derivation of the identity (1.2) can be found in e.g. [24]. In this paper we will consider fourth order analogues of the second order geometric evolution equation (1.1).

The surface diffusion flow for $\mathcal{S}(t)$ is given by the evolution law

$$\mathcal{V}_S = -\Delta_S \, k_m \qquad \text{on } \mathcal{S}(t) \,. \tag{1.3}$$

This law was introduced by Mullins, [39], in order to describe thermal grooving and this evolution law also has important applications in epitaxial growth, see e.g. [32, 1].

A flow combining surface diffusion and surface attachment limited kinetics introduced in [16], and analyzed in [29], is given by

$$\mathcal{V}_S = -\Delta_S \left(\frac{1}{\alpha} - \frac{1}{\xi} \Delta_S \right)^{-1} k_m \quad \text{on } \mathcal{S}(t) \,, \tag{1.4}$$

where $\alpha, \xi \in \mathbb{R}_{>0}$ are given parameters. This flow can be written as

$$\mathcal{V}_S = -\Delta_S \, y \,, \qquad \left(-\frac{1}{\xi} \Delta_S + \frac{1}{\alpha} \right) y = k_m \quad \text{on } \mathcal{S}(t) \,, \tag{1.5}$$

and in the limit of fast attachment kinetics $\xi \to \infty$ and $\alpha = 1$, we recover surface diffusion, (1.3). In the limit of fast surface diffusion $\alpha \to \infty$ and $\xi = 1$ we recover conserved mean curvature flow,

$$\mathcal{V}_S = k_m - \frac{\int_S k_m \, \mathrm{d}\mathcal{H}^2}{\int_S 1 \, \mathrm{d}\mathcal{H}^2} \quad \text{on } \mathcal{S}(t) \,,$$

with $\mathcal{H}^2$ being the surface measure. A discussion of these limits can be found in [45]. Hence, for general values α, $\xi \in \mathbb{R}_{>0}$, the intermediate flow (1.4) interpolates between surface diffusion and conserved mean curvature flow, see e.g. [29] and [4, p. 4282] for more details.

We now define the generalized Willmore energy of the surface $\mathcal{S}(t)$ as

$$\tfrac{1}{2} \int_{\mathcal{S}(t)} (k_m - \overline{\varkappa})^2 \, \mathrm{d}\mathcal{H}^2 \,, \tag{1.6}$$

where $\overline{\varkappa} \in \mathbb{R}$ is a given constant, the so-called spontaneous curvature. On $\mathcal{S}(t)$, Willmore flow, i.e. the L^2–gradient flow for (1.6), is given by

$$\mathcal{V}_S = -\Delta_S \, k_m - (k_m - \overline{\varkappa}) \, |\nabla_S \vec{n}_S|^2 + \tfrac{1}{2} (k_m - \overline{\varkappa})^2 \, k_m = -\Delta_S \, k_m + 2 \, (k_m - \overline{\varkappa}) \, k_g - \tfrac{1}{2} (k_m^2 - \overline{\varkappa}^2) \, k_m \qquad \text{on } \mathcal{S}(t) \,. \tag{1.7}$$

Here $\nabla_S \vec{n}_S$ is the Weingarten map and k_g is the Gaussian curvature of $\mathcal{S}(t)$, i.e. it is the product of the two principal curvatures. We also consider Helfrich flow, which is the volume and surface area preserving variant of (1.7).

In this paper, we consider the case that $\mathcal{S}(t)$ is an axisymmetric surface, that is rotationally symmetric with respect to the x_2–axis. We further assume that $\mathcal{S}(t)$ is made up of a single connected component, with or without boundary. Clearly, in the latter case the boundary $\partial\mathcal{S}(t)$ of $\mathcal{S}(t)$ consists of either one or two circles that each lie within a hyperplane that is parallel to the $x_1 - x_3$–plane. For the evolving family of surfaces we allow for the following types of boundary conditions. A boundary circle may assumed to be fixed, it may be allowed to move vertically along the boundary of a fixed infinite cylinder that is aligned with the axis of rotation, or it may be allowed to expand and shrink within a hyperplane that is parallel to the $x_1 - x_3$–plane. Depending on the postulated free energy, certain angle conditions will arise where $\mathcal{S}(t)$ meets the external boundary. If the free energy is just surface area, $\mathcal{H}^2(\mathcal{S}(t))$, then a
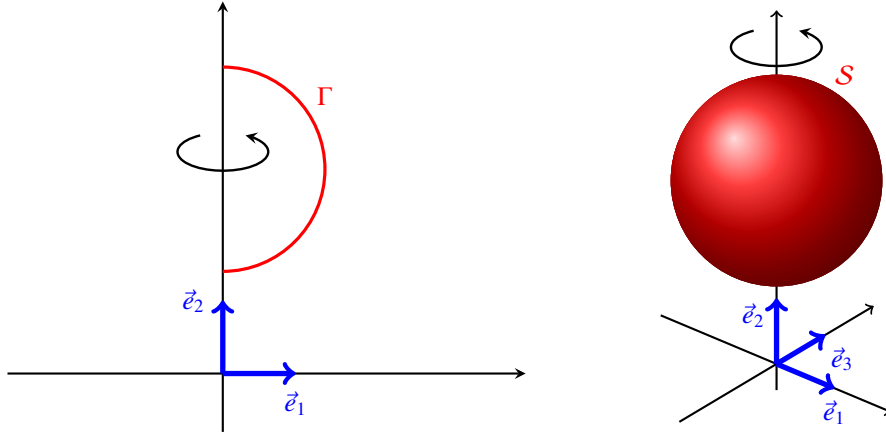
2

Figure 1: Sketch of Γ and $\mathcal{S}$, as well as the unit vectors $\vec{e}_1$, $\vec{e}_2$ and $\vec{e}_3$.

$90°$ degree contact angle condition arises. We refer to Section 2 below for further details, in particular with regard to more general contact angles.

Numerical analysis of geometric evolution equations has been an active field in the last thirty years and we refer to [24] for an overview. Approaches using parametric finite element methods have heavily relied on ideas of Gerd Dziuk, who first used a weak formulation of (1.2) in order to compute the mean curvature, see [26, 27]. The present authors have used the tangential degrees of freedom to improve the mesh quality during the evolution of discretized curvature flows, see [2, 3, 4, 5]. There has been interest in numerical schemes for axisymmetric schemes for geometric evolution equations both for second and for fourth order flows, see [41, 40, 14, 19, 20, 23, 25, 44, 47]. However, the literature on numerical analysis of such schemes is sparse. For exceptions we refer to [23, 25] in the context of graph formulations for surface diffusion and Willmore flow, respectively. Axisymmetric versions of geometric flows have also been treated analytically and questions regarding stability and singularity formation have been studied, see [34, 28, 13, 18, 35]. We also refer to [21, 22], who discuss the relation between the axisymmetric Willmore flow and the elastic flow in hyperbolic space.

The structure of this work is as follows. In Section 2 we introduce weak formulations for fourth order axisymmetric geometric flows, which all involve a splitting into two second order equations. The weak formulations are essential for the discretization with the help of piecewise linear, continuous finite elements. Spatially discretized semidiscrete schemes, based on these weak formulations, are introduced in Section 3. Fully discrete schemes are introduced in Section 4 and for some of the schemes existence, uniqueness and stability results are shown. Finally, in Section 5 numerical results for surface diffusion, for the intermediate law (1.4), for Willmore flow and for Helfrich flow are presented. The results demonstrate the stability and good mesh properties discussed in the preceding sections and the ideas presented in this paper hence have the potential to work also for more complex dynamics like the evolution of biomembranes in flows, see e.g. the setting in [9].

2. Weak formulations

Let $\mathbb{R}/\mathbb{Z}$ be the periodic interval $[0, 1]$, and set

$$I = \mathbb{R}/\mathbb{Z}, \text{ with } \partial I = \emptyset, \quad \text{or} \quad I = (0, 1), \text{ with } \partial I = \{0, 1\}.$$

We consider the axisymmetric situation, where $\vec{x}(t) : \overline{I} \to \mathbb{R}^2$ is a parameterization of $\Gamma(t)$. Throughout $\Gamma(t)$ represents the generating curve of a surface $\mathcal{S}(t)$ that is axisymmetric with respect to the x_2–axis, see Figure 1. In particular, on defining

$$\vec{\Pi}_3^3(r, z, \theta) = (r \cos \theta, z, r \sin \theta)^T \quad \text{for} \quad r \in \mathbb{R}_{\geq 0}, \, z \in \mathbb{R}, \, \theta \in [0, 2\pi]$$

and

$$\Pi_2^3(r, z) = \{\vec{\Pi}_3^3(r, z, \theta) : \theta \in [0, 2\pi)\},$$

3

we have that

$$S(t) = \bigcup_{(r,z)^T \in \Gamma(t)} \Pi_2^3(r,z) = \bigcup_{\rho \in \overline{I}} \Pi_2^3(\vec{x}(\rho,t)) . \tag{2.1}$$

Here we allow $\Gamma(t)$ to be either a closed curve, parameterized over $\mathbb{R}/\mathbb{Z}$, which corresponds to $S(t)$ being a genus-1 surface without boundary. Or $\Gamma(t)$ may be an open curve, parameterized over $[0,1]$. Then $\Gamma(t)$ has two endpoints, and each endpoint can either correspond to an interior point of $S(t)$, or to a boundary circle of $S(t)$. Endpoints of $\Gamma(t)$ that correspond to an interior point of the surface $S(t)$ are attached to the x_2–axis, on which they can freely move up and down. For example, if both endpoints of $\Gamma(t)$ are attached to the x_2–axis, then $S(t)$ is a genus-0 surface without boundary. If only one end of $\Gamma(t)$ is attached to the x_2–axis, then $S(t)$ is an open surface with boundary, where the boundary consists of a single connected component. If no endpoint of $\Gamma(t)$ is attached to the x_2–axis, then $S(t)$ is an open surface with boundary, where the boundary consists of two connected components.

In particular, we always assume that, for all $t \in [0,T]$,

$$\vec{x}(\rho,t) \cdot \vec{e}_1 > 0 \quad \forall \, \rho \in \overline{I} \setminus \partial_0 I , \tag{2.2a}$$

$$\vec{x}(\rho,t) \cdot \vec{e}_1 = 0 \quad \forall \, \rho \in \partial_0 I , \tag{2.2b}$$

$$\vec{x}_t(\rho,t) \cdot \vec{e}_i = 0 \quad \forall \, \rho \in \partial_i I , \; i = 1,2 , \tag{2.2c}$$

$$\vec{x}_t(\rho,t) = \vec{0} \quad \forall \, \rho \in \partial_D I , \tag{2.2d}$$

where $\partial_D I \cup \bigcup_{i=0}^{2} \partial_i I = \partial I$ is a disjoint partitioning of ∂I, with $\partial_0 I$ denoting the subset of boundary points of I that correspond to endpoints of $\Gamma(t)$ attached to the x_2–axis. Moreover, $\partial_D I \cup \bigcup_{i=1}^{2} \partial_i I$ denotes the subset of boundary points of I that model components of the boundary of $S(t)$. Here endpoints in $\partial_D I$ correspond to fixed boundary circles of $S(t)$, that lie within a hyperplane parallel to the $x_1 - x_3$–plane $\mathbb{R} \times \{0\} \times \mathbb{R}$. Endpoints in $\partial_1 I$ correspond to boundary circles of $S(t)$ that can move freely along the boundary of an infinite cylinder that is aligned with the axis of rotation. Endpoints in $\partial_2 I$ correspond to boundary circles of $S(t)$ that can expand/shrink freely within a hyperplane parallel to the $x_1 - x_3$–plane $\mathbb{R} \times \{0\} \times \mathbb{R}$. See Table 1 for a visualization of the different types of boundary nodes.

On assuming that

$$|\vec{x}_\rho| \geq c_0 > 0 \qquad \forall \, \rho \in \overline{I} , \tag{2.3}$$

we introduce the arclength s of the curve, i.e. $\partial_s = |\vec{x}_\rho|^{-1} \, \partial_\rho$, and set

$$\vec{\tau}(\rho,t) = \vec{x}_s(\rho,t) = \frac{\vec{x}_\rho(\rho,t)}{|\vec{x}_\rho(\rho,t)|} \quad \text{and} \quad \vec{\nu}(\rho,t) = -[\vec{\tau}(\rho,t)]^\perp , \tag{2.4}$$

where $(\cdot)^\perp$ denotes a clockwise rotation by $\frac{\pi}{2}$.

On recalling (2.1), we observe that the normal $\vec{\mathrm{n}}_S$ on $S(t)$ is given by

$$\vec{\mathrm{n}}_S(\vec{\Pi}_3^3(\vec{x}(\rho,t),\theta)) = \vec{\nu}_S(\rho,\theta,t) = \begin{pmatrix} (\vec{\nu}(\rho,t) \cdot \vec{e}_1) \, \cos\theta \\ \vec{\nu}(\rho,t) \cdot \vec{e}_2 \\ (\vec{\nu}(\rho,t) \cdot \vec{e}_1) \, \sin\theta \end{pmatrix} \quad \text{for} \quad \rho \in \overline{I}, \; \theta \in [0, 2\pi) \tag{2.5}$$

and $t \in [0,T]$. Similarly, the normal velocity $\mathcal{V}_S$ of $S(t)$ in the direction $\vec{\mathrm{n}}_S$ is given by

$$\mathcal{V}_S = \vec{x}_t(\rho,t) \cdot \vec{\nu}(\rho,t) \quad \text{on } \Pi_2^3(\vec{x}(\rho,t)) \subset S(t), \quad \forall \, \rho \in \overline{I}, \; t \in [0,T] .$$
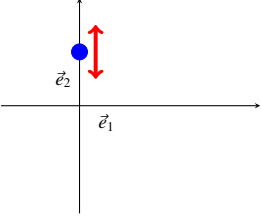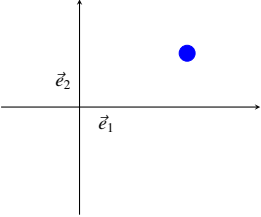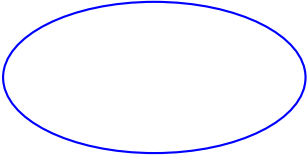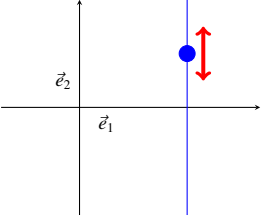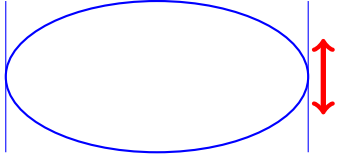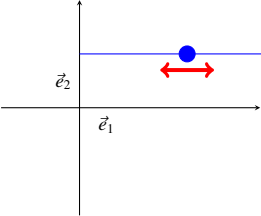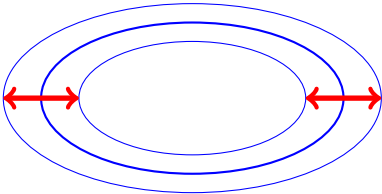
For the curvature $\varkappa$ of $\Gamma(t)$ it holds that

$$\varkappa \vec{\nu} = \vec{\varkappa} = \vec{\tau}_s = \frac{1}{|\vec{x}_\rho|} \left[\frac{\vec{x}_\rho}{|\vec{x}_\rho|} \right]_\rho . \tag{2.6}$$

An important role in this paper is played by the surface area of the surface $S(t)$, which is equal to

$$\mathcal{H}^2(S(t)) = A(\vec{x}(t)) = 2\pi \int_I \vec{x}(\rho,t) \cdot \vec{e}_1 \, |\vec{x}_\rho(\rho,t)| \, \mathrm{d}\rho . \tag{2.7}$$

Table 1: The different types of boundary nodes enforced by (2.2b)–(2.2d).

∂I	$\partial \Gamma$	$\partial \mathcal{S}$
$\partial_0 I$		N/A
$\partial_D I$		
$\partial_1 I$		
$\partial_2 I$	5	

Often the surface area, $A(\vec{x}(t))$, will play the role of the free energy in our paper. But for an open surface $\mathcal{S}(t)$, with boundary $\partial\mathcal{S}(t)$, we consider contact energy contributions which are discussed in [31], see also [6, (2.21)]. In the axisymmetric setting the relevant energy is given by

$$E(\vec{x}(t)) = A(\vec{x}(t)) + 2\pi \sum_{p\in\partial_1 I} \widehat{\varrho}_{\partial\mathcal{S}}^{(p)} (\vec{x}(p,t).\vec{e}_1)\, \vec{x}(p,t).\vec{e}_2 + \pi \sum_{p\in\partial_2 I} \widehat{\varrho}_{\partial\mathcal{S}}^{(p)} (\vec{x}(p,t).\vec{e}_1)^2 , \tag{2.8}$$

where we recall from (2.2c) that, for $i = 1, 2$, either $\partial_i I = \emptyset$, $\{0\}$, $\{1\}$ or $\{0, 1\}$. In the above $\widehat{\varrho}_{\partial\mathcal{S}}^{(p)} \in \mathbb{R}$, for $p \in \{0, 1\}$, are given constants. Here $\widehat{\varrho}_{\partial\mathcal{S}}^{(p)}$, for $p \in \partial_1 I$, denotes the change in contact energy density in the direction of $-\vec{e}_2$, that the two phases separated by the interface $\mathcal{S}(t)$ have with the infinite cylinder at the boundary circle of $\mathcal{S}(t)$ represented by $\vec{x}(p,t)$. Similarly, $\widehat{\varrho}_{\partial\mathcal{S}}^{(p)}$, for $p \in \partial_2 I$, denotes the change in contact energy density in the direction of $-\vec{e}_1$, that the two phases separated by the interface $\mathcal{S}(t)$ have with the hyperplane $\mathbb{R} \times \{0\}\mathbb{R}$ at the boundary circle of $\mathcal{S}(t)$ represented by $\vec{x}(p,t)$. These changes in contact energy lead to the contact angle conditions

$$(-1)^p\, \vec{\tau}(p,t).\vec{e}_2 = \widehat{\varrho}_{\partial\mathcal{S}}^{(p)} \qquad p \in \partial_1 I , \tag{2.9a}$$

$$(-1)^p\, \vec{\tau}(p,t).\vec{e}_1 = \widehat{\varrho}_{\partial\mathcal{S}}^{(p)} \qquad p \in \partial_2 I , \tag{2.9b}$$

for all $t \in (0, T)$. In most cases, the contact energies are assumed to be the same, so that $\widehat{\varrho}_{\partial\mathcal{S}}^{(0)} = \widehat{\varrho}_{\partial\mathcal{S}}^{(1)} = 0$, which leads to $90°$ contact angle conditions in (2.9), and means that (2.8) collapses to (2.7). See [6] for more details on contact angles and contact energies. We note that a necessary condition to admit a solution to (2.9a) or to (2.9b) is that $|\widehat{\varrho}_{\partial\mathcal{S}}^{(p)}| \leq 1$, but we do allow for more general values in (2.8). In addition, we observe that the energy (2.8) is not bounded from below if $\widehat{\varrho}_{\partial\mathcal{S}}^{(p)} \neq 0$ for $p \in \partial_1 I$ or if $\widehat{\varrho}_{\partial\mathcal{S}}^{(p)} < 0$ for $p \in \partial_2 I$.

For later use we note that

$$\frac{d}{dt} E(\vec{x}(t)) = 2\pi \int_I \left[\vec{x}_t.\vec{e}_1 + \vec{x}.\vec{e}_1 \frac{(\vec{x}_t)_\rho.\vec{x}_\rho}{|\vec{x}_\rho|^2} \right] |\vec{x}_\rho|\, d\rho + 2\pi \sum_{p\in\partial_1 I} \widehat{\varrho}_{\partial\mathcal{S}}^{(p)} \left[(\vec{x}_t(p,t).\vec{e}_1)\, \vec{x}(p,t).\vec{e}_2 + (\vec{x}(p,t).\vec{e}_1)\, \vec{x}_t(p,t).\vec{e}_2 \right]$$
$$+ 2\pi \sum_{p\in\partial_2 I} \widehat{\varrho}_{\partial\mathcal{S}}^{(p)} (\vec{x}(p,t).\vec{e}_1)\, \vec{x}_t(p,t).\vec{e}_1 . \tag{2.10}$$

Moreover, we recall that expressions for the mean curvature and the Gaussian curvature of $\mathcal{S}(t)$ are given by

$$\varkappa_S = \varkappa - \frac{\vec{\nu}.\vec{e}_1}{\vec{x}.\vec{e}_1} \quad \text{and} \quad \mathcal{K}_S = -\varkappa \frac{\vec{\nu}.\vec{e}_1}{\vec{x}.\vec{e}_1} \quad \text{on } \overline{I}, \tag{2.11}$$

respectively; see e.g. [20, (6)]. More precisely, if k_m and k_g denote the mean and Gaussian curvatures of $\mathcal{S}(t)$, then

$$k_m = \varkappa_S(\rho,t) \quad \text{and} \quad k_g = \mathcal{K}_S(\rho,t) \quad \text{on } \Pi_2^3(\vec{x}(\rho,t)) \subset \mathcal{S}(t), \quad \forall \rho \in \overline{I},\ t \in [0,T] . \tag{2.12}$$

In the literature, the two terms making up $\varkappa_S$ in (2.11) are often referred to as in-plane and azimuthal curvatures, respectively, with their sum being equal to the mean curvature. We note that combining (2.11) and (2.6) yields that

$$\varkappa_S \vec{\nu} = \varkappa \vec{\nu} - \frac{\vec{\nu}.\vec{e}_1}{\vec{x}.\vec{e}_1} \vec{\nu} = \frac{1}{|\vec{x}_\rho|} \left[\frac{\vec{x}_\rho}{|\vec{x}_\rho|} \right]_\rho - \frac{\vec{\nu}.\vec{e}_1}{\vec{x}.\vec{e}_1} \vec{\nu}, \tag{2.13}$$

see also (B.4) in Appendix Appendix B. It follows from (2.13) that

$$(\vec{x}.\vec{e}_1)\, \varkappa_S \vec{\nu} = (\vec{x}.\vec{e}_1)\, \vec{\tau}_s + (\vec{\tau}.\vec{e}_1)\, \vec{\tau} - \vec{e}_1 = [(\vec{x}.\vec{e}_1)\, \vec{\tau}]_s - \vec{e}_1 = [(\vec{x}.\vec{e}_1)\, \vec{x}_s]_s - \vec{e}_1 . \tag{2.14}$$

A weak formulation of (2.14) will form the basis of our stable approximations for surface diffusion, (1.3), and the intermediate flow (1.4). Clearly, for a smooth surface with bounded mean curvature it follows from (2.13) that

$$\vec{\nu}(\rho,t).\vec{e}_1 = 0 \qquad \forall \rho \in \partial_0 I, \quad \forall t \in [0,T], \tag{2.15}$$

which is clearly equivalent to

$$\vec{x}_\rho(\rho,t).\vec{e}_2 = 0 \qquad \forall \rho \in \partial_0 I, \quad \forall t \in [0,T]. \tag{2.16}$$

6

A precise derivation of (2.16) in the context of a weak formulation of (2.13) can be found in [12, Appendix A].

We observe that it follows from (2.15) and (2.6) that

$$\lim_{\rho \to \rho_0} \frac{\vec{v}(\rho,t).\vec{e}_1}{\vec{x}(\rho,t).\vec{e}_1} = \lim_{\rho \to \rho_0} \frac{\vec{v}_\rho(\rho,t).\vec{e}_1}{\vec{x}_\rho(\rho,t).\vec{e}_1} = \vec{v}_s(\rho_0,t).\vec{\tau}(\rho_0,t) = -\varkappa(\rho_0,t) \qquad \forall \rho_0 \in \partial_0 I, \ \forall t \in [0,T]. \tag{2.17}$$

2.1. Surface diffusion

On recalling (B.3) from Appendix Appendix B, we note that in the axisymmetric parameterization of $\mathcal{S}(t)$, the flow (1.3) can be written as

$$(\vec{x}.\vec{e}_1)\,\vec{x}_t.\vec{v} = -\left[\vec{x}.\vec{e}_1\,[\varkappa_S]_s\right]_s \qquad \text{on } I, \tag{2.18}$$

with, on recalling (2.2b)–(2.2d),

$$\vec{x}_t(\rho,t).\vec{e}_1 = 0 \quad \forall \rho \in \partial_0 I, \quad \vec{x}_t(\rho,t).\vec{e}_i = 0 \quad \forall \rho \in \partial_i I, \ i=1,2, \quad \vec{x}_t(\rho,t) = \vec{0} \quad \forall \rho \in \partial_D I, \qquad \forall t \in [0,T], \tag{2.19}$$

as well as (2.16), (2.9) and

$$(\varkappa_S)_\rho(\rho,t) = \left(\varkappa - \frac{\vec{v}.\vec{e}_1}{\vec{x}.\vec{e}_1}\right)_\rho (\rho,t) = 0 \qquad \forall \rho \in \partial I, \qquad \forall t \in (0,T]. \tag{2.20}$$

Here (2.20) for $\rho \in \partial_0 I$ ensures that the radially symmetric function k_m, recall (2.12), on $\mathcal{S}(t)$ induced by $\varkappa_S(t)$ is differentiable. For $\rho \in \partial_1 I \cup \partial_2 I \cup \partial_D I$ the condition (2.20) can be interpreted as a no-flux condition. We remark that (2.18) agrees with [41, (2)].

Let $\underline{V}_{\partial_0} = \{\vec{\eta} \in [H^1(I)]^2 : \vec{\eta}(\rho).\vec{e}_1 = 0 \quad \forall \rho \in \partial_0 I\}$ and $\underline{V}_\partial = \{\underline{V}_{\partial_0} : \vec{\eta}(\rho).\vec{e}_i = 0 \quad \forall \rho \in \partial_i I, \ i=1,2, \ \vec{\eta}(\rho) = \vec{0} \quad \forall \rho \in \partial_D I\}$. Then we consider the following weak formulation of (2.18) and (2.6), on recalling (2.11).

($\mathcal{E}$): Let $\vec{x}(0) \in \underline{V}_{\partial_0}$. For $t \in (0,T]$ find $\vec{x}(t) \in [H^1(I)]^2$, with $\vec{x}_t(t) \in \underline{V}_\partial$, and $\varkappa(t) \in H^1(I)$ such that

$$\int_I (\vec{x}.\vec{e}_1)\,\vec{x}_t.\vec{v}\chi\,|\vec{x}_\rho|\,\mathrm{d}\rho = \int_I \vec{x}.\vec{e}_1 \left(\varkappa - \frac{\vec{v}.\vec{e}_1}{\vec{x}.\vec{e}_1}\right)_\rho \chi_\rho\,|\vec{x}_\rho|^{-1}\,\mathrm{d}\rho \qquad \forall \chi \in H^1(I), \tag{2.21a}$$

$$\int_I \varkappa\,\vec{v}.\vec{\eta}\,|\vec{x}_\rho|\,\mathrm{d}\rho + \int_I (\vec{x}_\rho.\vec{\eta}_\rho)\,|\vec{x}_\rho|^{-1}\,\mathrm{d}\rho = -\sum_{i=1}^2 \sum_{p\in\partial_i I} \widehat{\varrho}_{\partial S}^{(p)}\,\vec{\eta}(p).\vec{e}_{3-i} \qquad \forall \vec{\eta} \in \underline{V}_\partial. \tag{2.21b}$$

We note that (2.21b) weakly imposes (2.16) and (2.9), while it is immediately clear that (2.21a) weakly imposes (2.20) on $\partial I \setminus \partial_0 I$. The degenerate weight $\vec{x}.\vec{e}_1$ on the right hand side in (2.21a) means that it is not obvious that (2.21a) weakly imposes (2.20) on $\partial_0 I$. Hence we rigorously derive in Appendix Appendix A that (2.21a) does indeed weakly impose (2.20) on $\partial_0 I$.

Let $\mathcal{L}^3$ denote the Lebesgue measure in $\mathbb{R}^3$. Then choosing $\chi = 2\pi$ in (2.21a) yields

$$\pm \frac{\mathrm{d}}{\mathrm{d}t}\mathcal{L}^3(\Omega(t)) = \int_{\mathcal{S}(t)} \mathcal{V}_S\,\mathrm{d}\mathcal{H}^2 = 2\pi \int_I (\vec{x}.\vec{e}_1)\,\vec{x}_t.\vec{v}|\vec{x}_\rho|\,\mathrm{d}\rho = 0, \tag{2.22}$$

where $\mathcal{S}(t) = \partial\Omega(t)$, and where the sign in (2.22) depends on whether $\vec{n}_S$ is the outer or inner normal to $\Omega(t)$ on $\mathcal{S}(t)$, recall (2.5). Moreover, choosing $\chi = \varkappa - \frac{\vec{v}.\vec{e}_1}{\vec{x}.\vec{e}_1}$ in (2.21a) and $\vec{\eta} = \vec{x}_t$ in (2.21b) yields, on recalling (2.10) and (2.2a), that

$$\frac{1}{2\pi}\frac{\mathrm{d}}{\mathrm{d}t}E(\vec{x}(t)) = -\int_I \vec{x}.\vec{e}_1 \left|\left[\varkappa - \frac{\vec{v}.\vec{e}_1}{\vec{x}.\vec{e}_1}\right]_\rho\right|^2 |\vec{x}_\rho|^{-1}\,\mathrm{d}\rho \leq 0. \tag{2.23}$$

It does not appear possible to mimic the proof of (2.23) on the discrete level. Hence we also introduce the following alternative formulation for surface diffusion, which treats the mean curvature $\varkappa_S(t)$ of $\mathcal{S}(t)$ as an unknown.

$(\mathcal{F})$: Let $\vec{x}(0) \in \underline{V}_{\partial_0}$. For $t \in (0, T]$ find $\vec{x}(t) \in [H^1(I)]^2$, with $\vec{x}_t(t) \in \underline{V}_\partial$, and $\varkappa_S(t) \in H^1(I)$ such that

$$\int_I (\vec{x} \cdot \vec{e}_1) \, \vec{x}_t \cdot \vec{\nu} \chi \, |\vec{x}_\rho| \, \mathrm{d}\rho = \int_I \vec{x} \cdot \vec{e}_1 \, (\varkappa_S)_\rho \, \chi_\rho \, |\vec{x}_\rho|^{-1} \, \mathrm{d}\rho \qquad \forall \, \chi \in H^1(I) \, , \tag{2.24a}$$

$$\int_I \vec{x} \cdot \vec{e}_1 \, \varkappa_S \, \vec{\nu} \cdot \vec{\eta} \, |\vec{x}_\rho| \, \mathrm{d}\rho + \int_I \left[\vec{\eta} \cdot \vec{e}_1 + \vec{x} \cdot \vec{e}_1 \, \frac{\vec{x}_\rho \cdot \vec{\eta}_\rho}{|\vec{x}_\rho|^2} \right] |\vec{x}_\rho| \, \mathrm{d}\rho = - \sum_{i=1}^{2} \sum_{p \in \partial_i I} \widehat{\varrho}_{\partial S}^{(p)} \, (\vec{x}(p, t) \cdot \vec{e}_1) \, \vec{\eta}(p) \cdot \vec{e}_{3-i} \qquad \forall \, \vec{\eta} \in \underline{V}_\partial \, . \tag{2.24b}$$

We note that (2.24b) weakly imposes (2.16) and (2.9), while (2.24a) weakly imposes (2.20), recall (2.11), where for the case $\partial_0 I \neq \emptyset$ we refer to Appendix Appendix A.

Choosing $\chi = 2\pi$ in (2.24a) yields (2.22), as before. Moreover, choosing $\chi = \varkappa_S$ in (2.24a) and $\vec{\eta} = \vec{x}_t$ in (2.24b) yields, on recalling (2.10), that

$$\frac{1}{2\pi} \frac{\mathrm{d}}{\mathrm{d}t} E(\vec{x}(t)) = - \int_I \vec{x} \cdot \vec{e}_1 \, |(\varkappa_S)_\rho|^2 \, |\vec{x}_\rho|^{-1} \, \mathrm{d}\rho \le 0 \, . \tag{2.25}$$

In contrast to (2.23), it will be possible to mimic the proof of (2.25) on the discrete level.

2.2. Intermediate evolution law

In the axisymmetric parameterization of $\mathcal{S}(t)$, the flow (1.5) can be written, similarly to (2.18), as

$$(\vec{x} \cdot \vec{e}_1) \, \vec{x}_t \cdot \vec{\nu} = - \left[\vec{x} \cdot \vec{e}_1 \, y_s \right]_s \, , \quad -\tfrac{1}{\xi} \left[\vec{x} \cdot \vec{e}_1 \, y_s \right]_s + \tfrac{1}{\alpha} \vec{x} \cdot \vec{e}_1 \, y = x \cdot \vec{e}_1 \, \varkappa_S \qquad \text{on } I \, , \tag{2.26}$$

with (2.19), as well as (2.16), (2.9) and

$$y_\rho(\rho, t) = 0 \qquad \forall \, \rho \in \partial I \, , \qquad \forall \, t \in (0, T] \, . \tag{2.27}$$

It is straightforward to adapt the formulations $(\mathcal{E})$ and $(\mathcal{F})$ to (2.26). For example, generalizing $(\mathcal{F})$ to (2.26) yields the following weak formulation.

$(\mathcal{I})$: Let $\vec{x}(0) \in \underline{V}_{\partial_0}$. For $t \in (0, T]$ find $\vec{x}(t) \in [H^1(I)]^2$, with $\vec{x}_t(t) \in \underline{V}_\partial$, and $(y(t), \varkappa_S(t)) \in [H^1(I)]^2$ such that

$$\int_I (\vec{x} \cdot \vec{e}_1) \, \vec{x}_t \cdot \vec{\nu} \chi \, |\vec{x}_\rho| \, \mathrm{d}\rho = \int_I \vec{x} \cdot \vec{e}_1 \, y_\rho \, \chi_\rho \, |\vec{x}_\rho|^{-1} \, \mathrm{d}\rho \qquad \forall \, \chi \in H^1(I) \, , \tag{2.28a}$$

$$\frac{1}{\xi} \int_I \vec{x} \cdot \vec{e}_1 \, y_\rho \, \zeta_\rho \, |\vec{x}_\rho|^{-1} \, \mathrm{d}\rho + \int_I \vec{x} \cdot \vec{e}_1 \left[\alpha^{-1} \, y - \varkappa_S \right] \zeta \, |\vec{x}_\rho| \, \mathrm{d}\rho = 0 \qquad \forall \, \zeta \in H^1(I) \, , \tag{2.28b}$$

$$\int_I \vec{x} \cdot \vec{e}_1 \, \varkappa_S \, \vec{\nu} \cdot \vec{\eta} \, |\vec{x}_\rho| \, \mathrm{d}\rho + \int_I \left[\vec{\eta} \cdot \vec{e}_1 + \vec{x} \cdot \vec{e}_1 \, \frac{\vec{x}_\rho \cdot \vec{\eta}_\rho}{|\vec{x}_\rho|^2} \right] |\vec{x}_\rho| \, \mathrm{d}\rho = - \sum_{i=1}^{2} \sum_{p \in \partial_i I} \widehat{\varrho}_{\partial S}^{(p)} \, (\vec{x}(p, t) \cdot \vec{e}_1) \, \vec{\eta}(p) \cdot \vec{e}_{3-i} \qquad \forall \, \vec{\eta} \in \underline{V}_\partial \, . \tag{2.28c}$$

The weak formulation of (2.26) corresponding to $(\mathcal{E})$ is given by (2.28a), (2.21b) and (2.28b) with $\varkappa_S$ replaced by the expression in (2.11). We note that (2.28c) weakly imposes (2.16) and (2.9), while (2.28a) and (2.28b) weakly impose (2.27), where for the case $\partial_0 I \neq \emptyset$ we refer once again to Appendix Appendix A.

Choosing $\chi = 2\pi$ in (2.28a) yields (2.22), as before. Moreover, choosing $\chi = \frac{\alpha}{\xi} \varkappa_S$ in (2.28a), $\zeta = \alpha \varkappa_S - y_s$ in (2.28b) and $\vec{\eta} = \frac{\alpha}{\xi} \vec{x}_t$ in (2.28c) yields, similarly to (2.25), that

$$\frac{\alpha}{\xi} \frac{1}{2\pi} \frac{\mathrm{d}}{\mathrm{d}t} E(\vec{x}(t)) = -\frac{\alpha}{\xi} \int_I \vec{x} \cdot \vec{e}_1 \, y_\rho \, (\varkappa_S)_\rho \, |\vec{x}_\rho|^{-1} \, \mathrm{d}\rho = -\frac{1}{\xi} \int_I \vec{x} \cdot \vec{e}_1 \, |y_\rho|^2 \, |\vec{x}_\rho|^{-1} \, \mathrm{d}\rho - \alpha \int_I \vec{x} \cdot \vec{e}_1 \, |\varkappa_S - \tfrac{1}{\alpha} y|^2 \, |\vec{x}_\rho| \, \mathrm{d}\rho \le 0 \, . \tag{2.29}$$

2.3. Willmore flow

It holds that the Willmore energy of the surface $\mathcal{S}(t)$, recall (1.6), can be written as

$$W(\vec{x}(t)) = \tfrac{1}{2} \int_{\mathcal{S}(t)} (k_m - \overline{\varkappa})^2 \, \mathrm{d}\mathcal{H}^2 = \pi \int_I \vec{x} \cdot \vec{e}_1 \, (\varkappa_S - \overline{\varkappa})^2 \, |\vec{x}_\rho| \, \mathrm{d}\rho \,,$$

see also [20, (6),(7)]. Noting once more (B.3) from Appendix Appendix B, a strong formulation for the flow (1.7) on I is given by

$$(\vec{x} \cdot \vec{e}_1) \, \vec{x}_t \cdot \vec{v} = -\left[\vec{x} \cdot \vec{e}_1 \, [\varkappa_S]_s \right]_s + 2 \, \vec{x} \cdot \vec{e}_1 \, [\varkappa_S - \overline{\varkappa}] \, \mathcal{K}_S - \tfrac{1}{2} \, \vec{x} \cdot \vec{e}_1 \left(\varkappa_S^2 - \overline{\varkappa}^2 \right) \varkappa_S \quad \text{on } I \,, \tag{2.30}$$

with (2.16), (2.20) and $\vec{x}_t(\rho, t) \cdot \vec{e}_1 = 0$ for $\rho \in \partial_0 I = \partial I$, $t \in [0, T]$. Here we stress that for Willmore flow we always assume that $\partial_0 I = \partial I$. That is because it does not appear possible to model Willmore flow for open surfaces in the weak formulation (2.31), below. The reason is that the relevant boundary conditions, i.e. clamped, Navier, semi-free or free, see e.g. [10, p. 1706], that would need to be enforced for $\vec{x}_t$, cannot be enforced through this weak formulation in the open curve case. Instead, techniques as in [10] are needed here, and we will consider the details in the forthcoming paper [11].

Then we consider the following weak formulation of (2.30) and (2.6), on recalling (2.11).

$(\mathcal{W})$: Let $\vec{x}(0) \in \underline{V}_{\partial_0}$. For $t \in (0, T]$ find $\vec{x}(t) \in [H^1(I)]^2$, with $\vec{x}_t(t) \in \underline{V}_\partial$, and $\varkappa(t) \in H^1(I)$ such that

$$\int_I (\vec{x} \cdot \vec{e}_1) \, \vec{x}_t \cdot \vec{v} \chi \, |\vec{x}_\rho| \, \mathrm{d}\rho = \int_I \vec{x} \cdot \vec{e}_1 \left[\varkappa - \frac{\vec{v} \cdot \vec{e}_1}{\vec{x} \cdot \vec{e}_1} \right]_\rho \chi \, |\vec{x}_\rho|^{-1} \, \mathrm{d}\rho - 2 \int_I \left[\varkappa - \frac{\vec{v} \cdot \vec{e}_1}{\vec{x} \cdot \vec{e}_1} - \overline{\varkappa} \right] \varkappa \vec{v} \cdot \vec{e}_1 \chi \, |\vec{x}_\rho| \, \mathrm{d}\rho$$

$$- \tfrac{1}{2} \int_I \vec{x} \cdot \vec{e}_1 \left(\left[\varkappa - \frac{\vec{v} \cdot \vec{e}_1}{\vec{x} \cdot \vec{e}_1} \right]^2 - \overline{\varkappa}^2 \right) \left[\varkappa - \frac{\vec{v} \cdot \vec{e}_1}{\vec{x} \cdot \vec{e}_1} \right] \chi \, |\vec{x}_\rho| \, \mathrm{d}\rho \qquad \forall \, \chi \in H^1(I) \,, \tag{2.31a}$$

$$\int_I \varkappa \vec{v} \cdot \vec{\eta} \, |\vec{x}_\rho| \, \mathrm{d}\rho + \int_I \vec{x}_\rho \cdot \vec{\eta}_\rho \, |\vec{x}_\rho|^{-1} \, \mathrm{d}\rho = 0 \qquad \forall \, \vec{\eta} \in \underline{V}_\partial \,. \tag{2.31b}$$

We note that the two last terms on the right hand side of (2.31a) give no contribution at the boundary $\partial I = \partial_0 I$, since $\vec{v} \cdot \vec{e}_1 = \vec{x} \cdot \vec{e}_1 = 0$ there. We also note that (2.31b) weakly imposes (2.16). Similarly to (2.21a), we note that (2.31a) weakly imposes (2.20), see [12, Appendix A] for details in the case $\rho \in \partial_0 I$.

We note that in contrast to surface diffusion, a weak formulation for Willmore flow based on $\varkappa_S$, i.e. (2.24b), has no benefits over the presented formulation (2.31). Due to the presence of Gaussian curvature, recall (1.7) and (2.11), a weak formulation based on (2.24b) would still involve the singular fraction $\frac{\vec{v} \cdot \vec{e}_1}{\vec{x} \cdot \vec{e}_1}$, since $\vec{x} \cdot \vec{e}_1 \, \mathcal{K}_S = -(\varkappa_S + \frac{\vec{v} \cdot \vec{e}_1}{\vec{x} \cdot \vec{e}_1}) \, \vec{v} \cdot \vec{e}_1$. Moreover, and in contrast to a formulation with (2.31b), discretizations based on such a formulation would exhibit tangential motion of vertices that does not lead to equidistribution, and which for linear fully discrete schemes may lead to a breakdown of the scheme.

2.3.1. Helfrich flow

Helfrich flow is given as the surface area and volume preserving variant of (1.7). Its strong formulation can be written as

$$\mathcal{V}_S = -\Delta_S k_m + 2 \, (k_m - \overline{\varkappa}) \, k_g - \tfrac{1}{2} \, (k_m^2 - \overline{\varkappa}^2) \, k_m + \lambda_A \, k_m + \lambda_V \quad \text{on } \mathcal{S}(t) \,, \tag{2.32}$$

where $(\lambda_A(t), \lambda_V(t))^T \in \mathbb{R}^2$ are chosen such that

$$\mathcal{H}^2(\mathcal{S}(t)) = \mathcal{H}^2(\mathcal{S}(0)) \,, \qquad \mathcal{L}^3(\Omega(t)) = \mathcal{L}^3(\Omega(0)) \,. \tag{2.33}$$

On writing (2.31a) as

$$\int_I (\vec{x} \cdot \vec{e}_1) \, \vec{x}_t \cdot \vec{v} \chi \, |\vec{x}_\rho| \, \mathrm{d}\rho - \int_I \vec{x} \cdot \vec{e}_1 \left[\varkappa - \frac{\vec{v} \cdot \vec{e}_1}{\vec{x} \cdot \vec{e}_1} \right]_\rho \chi \, |\vec{x}_\rho|^{-1} \, \mathrm{d}\rho = \int_I f \chi \, |\vec{x}_\rho| \, \mathrm{d}\rho$$

a weak formulation of Helfrich flow is given as follows.

$(\mathcal{W}^{A,V})$: Let $\vec{x}(0) \in \underline{V}_{\partial_0}$. For $t \in (0,T]$ find $\vec{x}(t) \in [H^1(I)]^2$, with $\vec{x}_t(t) \in \underline{V}_\partial$, and $\varkappa(t) \in H^1(I)$ such that

$$\int_I (\vec{x}.\vec{e}_1)\, \vec{x}_t.\vec{v}\, \chi\, |\vec{x}_\rho|\, \mathrm{d}\rho - \int_I \vec{x}.\vec{e}_1 \left[\varkappa - \frac{\vec{v}.\vec{e}_1}{\vec{x}.\vec{e}_1} \right]_\rho \chi_\rho\, |\vec{x}_\rho|^{-1}\, \mathrm{d}\rho$$

$$= \int_I f\, \chi\, |\vec{x}_\rho|\, \mathrm{d}\rho + \lambda_A \int_I \vec{x}.\vec{e}_1 \left[\varkappa - \frac{\vec{v}.\vec{e}_1}{\vec{x}.\vec{e}_1} \right] \chi\, |\vec{x}_\rho|\, \mathrm{d}\rho + \lambda_V \int_I \vec{x}.\vec{e}_1 \chi\, |\vec{x}_\rho|\, \mathrm{d}\rho \qquad \forall\, \chi \in H^1(I) \tag{2.34}$$

and (2.31b) hold, with $(\lambda_A(t), \lambda_V(t))^T \in \mathbb{R}^2$ chosen such that (2.33) hold.

3. Semidiscrete schemes

Let $[0,1] = \cup_{j=1}^J I_j$, $J \geq 3$, be a decomposition of $[0,1]$ into intervals given by the nodes q_j, $I_j = [q_{j-1}, q_j]$. For simplicity, and without loss of generality, we assume that the subintervals form an equipartitioning of $[0,1]$, i.e. that

$$q_j = jh, \quad \text{with} \quad h = J^{-1}, \qquad j = 0, \dots, J. \tag{3.1}$$

Clearly, if $I = \mathbb{R}/\mathbb{Z}$ we identify $0 = q_0 = q_J = 1$.

The necessary finite element spaces are defined as follows: $V^h = \{\chi \in C(\bar{I}) : \chi\,|_{I_j}$ is linear $\forall\, j = 1 \to J\}$ and $\underline{V}^h = [V^h]^2$, $\underline{V}^h_{\partial_0} = \underline{V}^h \cap \underline{V}_{\partial_0}$, $\underline{V}^h_\partial = \underline{V}^h \cap \underline{V}_\partial$. We also define $W^h = V^h$, $W^h_{\partial_0} = \{\chi \in V^h : \chi(\rho) = 0 \quad \forall\, \rho \in \partial_0 I\}$, $\underline{W}^h = \underline{V}^h$, $\underline{W}^h_{\partial_0} = [W^h_{\partial_0}]^2$. Let $\{\chi_j\}_{j=j_0}^J$ denote the standard basis of V^h, where $j_0 = 0$ if $I = (0,1)$ and $j_0 = 1$ if $I = \mathbb{R}/\mathbb{Z}$. For later use, we let $\pi^h : C(\bar{I}) \to V^h$ be the standard interpolation operator at the nodes $\{q_j\}_{j=0}^J$.

Let $(\cdot, \cdot)$ denote the L^2–inner product on I, and define the mass lumped L^2–inner product $(f,g)^h$, for two piecewise continuous functions, with possible jumps at the nodes $\{q_j\}_{j=1}^J$, via

$$(f,g)^h = \tfrac{1}{2} \sum_{j=1}^J h_j \left[(f\,g)(q_j^-) + (f\,g)(q_{j-1}^+) \right], \tag{3.2}$$

where we define $f(q_j^\pm) = \lim_{\delta \searrow 0} f(q_j \pm \delta)$. The definition (3.2) naturally extends to vector valued functions.

Let $(\vec{X}^h(t))_{t \in [0,T]}$, with $\vec{X}^h(t) \in \underline{V}^h_{\partial_0}$, be an approximation to $(\vec{x}(t))_{t \in [0,T]}$ and define $\Gamma^h(t) = \vec{X}^h(t)(\bar{I})$. Throughout this section we assume that

$$\vec{X}^h(\rho, t).\vec{e}_1 > 0 \quad \forall\, \rho \in \bar{I} \setminus \partial_0 I, \qquad \forall\, t \in [0,T].$$

Assuming that $|\vec{X}^h_\rho| > 0$ almost everywhere on I, and similarly to (2.4), we set

$$\vec{\tau}^h = \vec{X}^h_s = \frac{\vec{X}^h_\rho}{|\vec{X}^h_\rho|} \qquad \text{and} \qquad \vec{v}^h = -(\vec{\tau}^h)^\perp. \tag{3.3}$$

For later use, we let $\vec{\omega}^h \in \underline{V}^h$ be the mass-lumped L^2–projection of $\vec{v}^h$ onto $\underline{V}^h$, i.e.

$$\left(\vec{\omega}^h, \vec{\varphi}\, |\vec{X}^h_\rho| \right)^h = \left(\vec{v}^h, \vec{\varphi}\, |\vec{X}^h_\rho| \right) = \left(\vec{v}^h, \vec{\varphi}\, |\vec{X}^h_\rho| \right)^h \qquad \forall\, \vec{\varphi} \in \underline{V}^h. \tag{3.4}$$

Recall that

$$A(\vec{Z}^h) = 2\pi \left(\vec{Z}^h.\vec{e}_1, |\vec{Z}^h_\rho| \right) \quad \vec{Z}^h \in \underline{V}^h_{\partial_0} \tag{3.5}$$

and

$$E(\vec{X}^h(t)) = A(\vec{X}^h(t)) + 2\pi \sum_{p \in \partial_1 I} \widehat{\varrho}^{(p)}_{\partial S} (\vec{X}^h(p,t).\vec{e}_1)\, \vec{X}^h(p,t).\vec{e}_2 + \pi \sum_{p \in \partial_2 I} \widehat{\varrho}^{(p)}_{\partial S} (\vec{X}^h(p,t).\vec{e}_1)^2. \tag{3.6}$$

We have, similarly to (2.10), that

$$
\frac{\mathrm{d}}{\mathrm{d}t} E(\vec{X}^h(t)) = 2\pi \left(\left[\vec{X}_t^h \cdot \vec{e}_1 + \vec{X}^h \cdot \vec{e}_1 \frac{(\vec{X}_t^h)_\rho \cdot \vec{X}_\rho^h}{|\vec{X}_\rho^h|^2} \right], |\vec{X}_\rho^h| \right)
$$
$$
+ 2\pi \sum_{p \in \partial_1 I} \widehat{\varrho}_{\partial S}^{(p)} \left[(\vec{X}_t^h(p,t) \cdot \vec{e}_1) \vec{X}^h(p,t) \cdot \vec{e}_2 + (\vec{X}^h(p,t) \cdot \vec{e}_1) \vec{X}_t^h(p,t) \cdot \vec{e}_2 \right]
$$
$$
+ 2\pi \sum_{p \in \partial_2 I} \widehat{\varrho}_{\partial S}^{(p)} (\vec{X}^h(p,t) \cdot \vec{e}_1) \vec{X}_t^h(p,t) \cdot \vec{e}_1 . \tag{3.7}
$$

In view of the degeneracy on the right hand side of (2.13), and on recalling (2.17) and (3.4), we introduce, given a $\kappa^h(t) \in V^h$, the function $\mathfrak{K}^h(\kappa^h(t), t) \in V^h$ such that

$$
[\mathfrak{K}^h(\kappa^h(t), t)](q_j) = \begin{cases} \dfrac{\vec{\omega}^h(q_j, t) \cdot \vec{e}_1}{\vec{X}^h(q_j, t) \cdot \vec{e}_1} & q_j \in \overline{I} \setminus \partial_0 I , \\ -\kappa^h(q_j, t) & q_j \in \partial_0 I . \end{cases} \tag{3.8}
$$

3.1. Surface diffusion

Our semidiscrete finite element approximation of $(\mathcal{E})$, (2.21), is given as follows.

$(\mathcal{E}_h)^{(h)}$: Let $\vec{X}^h(0) \in \underline{V}_{\partial_0}^h$. For $t \in (0, T]$ find $\vec{X}^h(t) \in \underline{V}^h$, with $\vec{X}_t^h(t) \in \underline{V}_\partial^h$, and $\kappa^h(t) \in V^h$ such that

$$
\left((\vec{X}^h \cdot \vec{e}_1) \vec{X}_t^h, \chi\, \vec{\nu}^h\, |\vec{X}_\rho^h| \right)^{(h)} = \left(\vec{X}^h \cdot \vec{e}_1 \left[\kappa^h - \mathfrak{K}^h(\kappa^h) \right]_\rho , \chi_\rho\, |\vec{X}_\rho^h|^{-1} \right) \qquad \forall \chi \in V^h , \tag{3.9a}
$$

$$
\left(\kappa^h\, \vec{\nu}^h, \vec{\eta}\, |\vec{X}_\rho^h| \right)^{(h)} + \left(\vec{X}_\rho^h, \vec{\eta}_\rho\, |\vec{X}_\rho^h|^{-1} \right) = - \sum_{i=1}^{2} \sum_{p \in \partial_i I} \widehat{\varrho}_{\partial S}^{(p)} \vec{\eta}(p) \cdot \vec{e}_{3-i} \qquad \forall \vec{\eta} \in \underline{V}_\partial^h . \tag{3.9b}
$$

Here, and throughout, we use the notation $\cdot^{(h)}$ to denote an expression with or without the superscript h. I.e. the scheme $(\mathcal{E}_h)^h$ employs mass lumping on some terms, recall (3.2), while the scheme $(\mathcal{E}_h)$ employs true integration throughout. We stress that the side condition (3.9b), for $(\mathcal{E}_h)^h$, leads to an equidistribution property; see Remark 3.1 below.

For later use we observe that

$$
\mathcal{L}^3(\Omega^h(t)) = 2\pi \int_{A^h(t)} \vec{\mathrm{id}} \cdot \vec{e}_1\, \mathrm{d}\mathcal{L}^2 = \pi \int_{A^h(t)} \nabla \cdot \left[(\vec{\mathrm{id}} \cdot \vec{e}_1)^2\, \vec{e}_1 \right] \mathrm{d}\mathcal{L}^2
$$
$$
= \pi \int_{\Gamma^h(t)} (\vec{\mathrm{id}} \cdot \vec{e}_1)^2\, \vec{\nu}^h \cdot \vec{e}_1\, \mathrm{d}\mathcal{H}^1 = \pi \int_I (\vec{X}^h \cdot \vec{e}_1)^2\, \vec{\nu}^h \cdot \vec{e}_1\, |\vec{X}_\rho^h|\, \mathrm{d}\rho , \tag{3.10}
$$

where $A^h(t) \subset \mathbb{R}^2$ denotes the domain enclosed by $\Gamma^h(t) = \vec{X}^h(\overline{I})$, and where $\vec{\nu}^h(t)$ denotes the outer normal to $A^h(t)$ on $\partial A^h(t) = \Gamma^h(t)$. Of course, $\Omega^h(t) \subset \mathbb{R}^3$ denotes the domain that is enclosed by the three-dimensional axisymmetric surface $\mathcal{S}^h(t)$ that is generated by the curve $\Gamma^h(t)$, i.e. $\mathcal{S}^h(t) = \partial\Omega^h(t)$. Moreover, on recalling (2.22), we note that

$$
\frac{\mathrm{d}}{\mathrm{d}t} \mathcal{L}^3(\Omega^h(t)) = \int_{\mathcal{S}^h(t)} \mathcal{V}_{\mathcal{S}^h}^h\, \mathrm{d}\mathcal{H}^2 = 2\pi \left(\vec{X}^h \cdot \vec{e}_1, \vec{X}_t^h \cdot \vec{\nu}^h\, |\vec{X}_\rho^h| \right) , \tag{3.11}
$$

where $\mathcal{V}_{\mathcal{S}^h}^h(t)$ denotes the normal velocity of $\mathcal{S}^h(t)$ in the direction of $\vec{\nu}_{\mathcal{S}^h}^h(t)$, the outer normal to $\Omega^h(t)$ on $\mathcal{S}^h(t)$.

Choosing $\chi = 1$ in (3.9a) yields that

$$
\left(\vec{X}^h \cdot \vec{e}_1, \vec{X}_t^h \cdot \vec{\nu}^h\, |\vec{X}_\rho^h| \right)^{(h)} = 0 . \tag{3.12}
$$

Comparing (3.11) and (3.12), we observe that due to mass lumping being employed in (3.9a) for $(\mathcal{E}_h)^h$, it is not possible to prove exact volume conservation for $(\mathcal{E}_h)^h$. On the other hand, for the semidiscrete scheme $(\mathcal{E}_h)$ we obtain exact volume preservation. We note that in practice the fully discrete variants of both $(\mathcal{E}_h)^h$ and $(\mathcal{E}_h)$, for reasonable meshes, have excellent volume conserving properties.

Our semidiscrete finite element approximation of $(\mathcal{F})$, (2.24), is given as follows.

11

Table 2: Properties of the different semidiscrete schemes for the evolution laws (1.3), (1.4), (1.7) and (2.32). Note that subscripts refer to semidiscretization, whereas superscripts indicate numerical integration, recall (3.2).

scheme		flow	stability proof	equidistribution
$(\mathcal{E}_h)^h / (\mathcal{E}_h)$	(3.9)	(1.3)	no	yes / no
$(\mathcal{F}_h)^h / (\mathcal{F}_h)$	(3.13)	(1.3)	yes	no
$(\mathcal{I}_h)^h / (\mathcal{I}_h)$	(3.15)	(1.4)	yes	no
$(\mathcal{W}_h)^h$	(3.16)	(1.7)	no	yes
$(\mathcal{W}_h^{A,V})^h$	(3.17), (3.19)	(2.32)	no	yes

$(\mathcal{F}_h)^{(h)}$: Let $\vec{X}^h(0) \in \underline{V}_{\partial_0}^h$. For $t \in (0,T]$ find $\vec{X}^h(t) \in \underline{V}^h$, with $\vec{X}_t^h(t) \in \underline{V}_{\partial}^h$, and $\kappa_{\mathcal{S}}^h(t) \in V^h$ such that

$$\left((\vec{X}^h . \vec{e}_1) \vec{X}_t^h, \chi \vec{\nu}^h |\vec{X}_\rho^h| \right)^{(h)} = \left(\vec{X}^h . \vec{e}_1 \left[\kappa_{\mathcal{S}}^h \right]_\rho, \chi_\rho |\vec{X}_\rho^h|^{-1} \right) \qquad \forall \chi \in V^h, \tag{3.13a}$$

$$\left(\vec{X}^h . \vec{e}_1 \kappa_{\mathcal{S}}^h \vec{\nu}^h, \vec{\eta} |\vec{X}_\rho^h| \right)^{(h)} + \left(\vec{\eta} . \vec{e}_1, |\vec{X}_\rho^h| \right) + \left((\vec{X}^h . \vec{e}_1) \vec{X}_\rho^h, \vec{\eta}_\rho |\vec{X}_\rho^h|^{-1} \right) = -\sum_{i=1}^{2} \sum_{p \in \partial_i I} \widehat{\varrho}_{\partial \mathcal{S}}^{(p)} (\vec{X}^h(p,t) . \vec{e}_1) \vec{\eta}(p) . \vec{e}_{3-i} \qquad \forall \vec{\eta} \in \underline{V}_{\partial}^h. \tag{3.13b}$$

Choosing $\chi = 1$ in (3.13a), on recalling (3.11), yields exact volume conservation for the scheme $(\mathcal{F}_h)$. Moreover, in contrast to $(\mathcal{E}_h)^{(h)}$, it is possible to prove a stability bound for $(\mathcal{F}_h)^{(h)}$. To this end, choose $\chi = \kappa_{\mathcal{S}}^h$ in (3.13a) and $\vec{\eta} = \vec{X}_t^h$ in (3.13b) to obtain, on recalling (3.7), that

$$\frac{\mathrm{d}}{\mathrm{d}t} E(\vec{X}^h(t)) = -2\pi \left(\vec{X}^h . \vec{e}_1 |(\kappa_{\mathcal{S}}^h)_\rho|^2, |\vec{X}_\rho^h|^{-1} \right) \le 0.$$

Remark 3.1. Let $\vec{h}_j(t) = \vec{X}^h(q_j, t) - \vec{X}^h(q_{j-1}, t)$ for $j = 1, \ldots, J$, and set $\vec{h}_0 = \vec{h}_J$ if $\partial I = \emptyset$. Then, if $(\vec{X}^h(t), \kappa^h(t)) \in \underline{V}^h \times V^h$ satisfies (3.9b), for $(\mathcal{E}_h)^h$, it holds that

$$|\vec{h}_j(t)| = |\vec{h}_{j-1}(t)| \quad \text{if} \quad \vec{h}_j(t) \nparallel \vec{h}_{j-1}(t) \quad \begin{cases} j = 1, \ldots, J & \partial I = \emptyset, \\ j = 2, \ldots, J & \partial I \ne \emptyset. \end{cases} \tag{3.14}$$

The equidistribution property (3.14) can be shown by choosing $\vec{\eta} = \chi_{j-1} [\vec{\omega}^h(q_{j-1}, t)]^\perp \in \underline{V}_{\partial}^h$ in (3.9b), recall (3.4). See also [2, Remark 2.4] for more details. We stress that (3.13b), even for $(\mathcal{F}_h)^h$, does not lead to an equidistribution property for $\Gamma^h(t)$.

For the reader's convenience, Table 2 summarises the main properties of all the schemes introduced in Section 3.

3.2. Intermediate evolution law

It is straightforward to adapt the semidiscrete schemes $(\mathcal{E})^h$ and $(\mathcal{F})^{(h)}$ to the flow (1.5). For example, a semidiscrete finite element approximation of $(\mathcal{I})$, (2.28), that is based on $(\mathcal{F}_h)^{(h)}$, is given as follows.

$(\mathcal{I}_h)^{(h)}$: Let $\vec{X}^h(0) \in \underline{V}_{\partial_0}^h$. For $t \in (0,T]$ find $\vec{X}^h(t) \in \underline{V}^h$, with $\vec{X}_t^h(t) \in \underline{V}_{\partial}^h$, and $(Y^h(t), \kappa_{\mathcal{S}}^h(t)) \in [V^h]^2$ such that

$$\left((\vec{X}^h . \vec{e}_1) \vec{X}_t^h, \chi \vec{\nu}^h |\vec{X}_\rho^h| \right)^{(h)} = \left(\vec{X}^h . \vec{e}_1 Y_\rho^h, \chi_\rho |\vec{X}_\rho^h|^{-1} \right) \qquad \forall \chi \in V^h, \tag{3.15a}$$

$$\frac{1}{\xi} \left(\vec{X}^h . \vec{e}_1 Y_\rho^h, \zeta_\rho |\vec{X}_\rho^h|^{-1} \right) + \left(\vec{X}^h . \vec{e}_1 \left[\alpha^{-1} Y^h - \kappa_{\mathcal{S}}^h \right], \zeta |\vec{X}_\rho^h| \right)^{(h)} = 0 \qquad \forall \zeta \in V^h, \tag{3.15b}$$

$$\left(\vec{X}^h . \vec{e}_1 \kappa_{\mathcal{S}}^h \vec{\nu}^h, \vec{\eta} |\vec{X}_\rho^h| \right)^{(h)} + \left(\vec{\eta} . \vec{e}_1, |\vec{X}_\rho^h| \right) + \left((\vec{X}^h . \vec{e}_1) \vec{X}_\rho^h, \vec{\eta}_\rho |\vec{X}_\rho^h|^{-1} \right) = -\sum_{i=1}^{2} \sum_{p \in \partial_i I} \widehat{\varrho}_{\partial \mathcal{S}}^{(p)} (\vec{X}^h(p,t) . \vec{e}_1) \vec{\eta}(p) . \vec{e}_{3-i} \qquad \forall \vec{\eta} \in \underline{V}_{\partial}^h. \tag{3.15c}$$

Choosing $\chi = 1$ in (3.15a), on recalling (3.11), yields exact volume conservation for the scheme $(\mathcal{I}_h)$. Moreover, it is possible to prove a stability bound for $(\mathcal{I}_h)^{(h)}$. To this end, choose $\chi = \frac{\alpha}{\xi} \kappa_{\mathcal{S}}^h$ in (3.15a), $\zeta = \alpha \kappa_{\mathcal{S}}^h - Y^h$ in (3.15b) and

$\vec{\eta} = \vec{X}_t^h$ in (3.15c) to obtain, on recalling (3.7), that

$$\frac{1}{2\pi}\frac{d}{dt} E(\vec{X}^h(t)) = -\frac{1}{\alpha}\left(\vec{X}^h.\vec{e}_1\,|Y_\rho^h|^2, |\vec{X}_\rho^h|^{-1}\right) - \xi\left(\vec{X}^h.\vec{e}_1\,|\kappa_{\mathcal{S}}^h - \tfrac{1}{\alpha}\,Y^h|^2, |\vec{X}_\rho^h|\right)^{(h)} \le 0\,,$$

which is a discrete analogue of (2.29).

3.3. Willmore flow

Our semidiscrete finite element approximation of $(\mathcal{W})$, (2.31), is given as follows, where we recall that $\partial I = \partial_0 I$, and so $\vec{X}^h(t) \in \underline{V}_\partial^h$ for all $t \in [0,T]$.

$(\mathcal{W}_h)^h$: Let $\vec{X}^h(0) \in \underline{V}_\partial^h$. For $t \in (0,T]$ find $\vec{X}^h(t) \in \underline{V}^h$, with $\vec{X}_t^h(t) \in \underline{V}_\partial^h$, and $\kappa^h(t) \in V^h$ such that

$$\left((\vec{X}^h.\vec{e}_1)\,\vec{X}_t^h, \chi\,\vec{\nu}^h\,|\vec{X}_\rho^h|\right)^h - \left(\vec{X}^h.\vec{e}_1\left[\kappa^h - \mathfrak{R}^h(\kappa^h)\right]_\rho, \chi_\rho\,|\vec{X}_\rho^h|^{-1}\right) = -2\left(\left[\kappa^h - \frac{\vec{\omega}^h.\vec{e}_1}{\vec{X}^h.\vec{e}_1} - \overline{\varkappa}\right]\kappa^h\,\vec{\omega}^h.\vec{e}_1, \chi\,|\vec{X}_\rho^h|\right)^h$$

$$-\tfrac{1}{2}\left(\vec{X}^h.\vec{e}_1\left(\left[\kappa^h - \frac{\vec{\omega}^h.\vec{e}_1}{\vec{X}^h.\vec{e}_1}\right]^2 - \overline{\varkappa}^2\right)\left[\kappa^h - \frac{\vec{\omega}^h.\vec{e}_1}{\vec{X}^h.\vec{e}_1}\right], \chi\,|\vec{X}_\rho^h|\right)^h \qquad \forall \chi \in V^h, \qquad (3.16a)$$

$$\left(\kappa^h\,\vec{\nu}^h, \vec{\eta}\,|\vec{X}_\rho^h|\right)^h + \left(\vec{X}_\rho^h, \vec{\eta}_\rho\,|\vec{X}_\rho^h|^{-1}\right) = 0 \qquad \forall \vec{\eta} \in \underline{V}_\partial^h\,. \qquad (3.16b)$$

We recall from Remark 3.1 that (3.16b) leads to the equidistribution property (3.14). For this reason we only consider the variant $(\mathcal{W}_h)^h$ with mass lumping.

3.3.1. Helfrich flow

On re-writing (3.16a) as

$$\left((\vec{X}^h.\vec{e}_1)\,\vec{X}_t^h, \chi\,\vec{\nu}^h\,|\vec{X}_\rho^h|\right)^h - \left(\vec{X}^h.\vec{e}_1\left[\kappa^h - \mathfrak{R}^h(\kappa^h)\right]_\rho, \chi_\rho\,|\vec{X}_\rho^h|^{-1}\right) = \left(f^h, \chi\,|\vec{X}_\rho^h|\right)^h\,,$$

we consider the following semidiscrete finite element approximation of $(\mathcal{W}^{A,V})$, (2.34), (2.31b).

$(\mathcal{W}_h^{A,V})^h$: Let $\vec{X}^h(0) \in \underline{V}_\partial^h$. For $t \in (0,T]$ find $\vec{X}^h(t) \in \underline{V}^h$, with $\vec{X}_t^h(t) \in \underline{V}_\partial^h$, and $(\kappa^h(t), \lambda_A^h(t), \lambda_V^h(t)) \in V^h \times \mathbb{R}^2$ such that

$$\left((\vec{X}^h.\vec{e}_1)\,\vec{X}_t^h, \chi\,\vec{\nu}^h\,|\vec{X}_\rho^h|\right)^h - \left(\vec{X}^h.\vec{e}_1\left[\kappa^h - \mathfrak{R}^h(\kappa^h)\right]_\rho, \chi_\rho\,|\vec{X}_\rho^h|^{-1}\right)$$

$$= \left(f^h, \chi\,|\vec{X}_\rho^h|\right) + \lambda_A^h\left(\vec{X}^h.\vec{e}_1\left[\kappa^h - \mathfrak{R}^h(\kappa^h)\right], \chi\,|\vec{X}_\rho^h|\right)^h + \lambda_V^h\left(\vec{X}^h.\vec{e}_1, \chi\,|\vec{X}_\rho^h|\right)^h \qquad \forall \chi \in V^h\,, \qquad (3.17)$$

where $(\lambda_A^h, \lambda_V^h)^T \in \mathbb{R}^2$ are such that

$$\mathcal{H}^2(\mathcal{S}^h(t)) = \mathcal{H}^2(\mathcal{S}^h(0))\,, \qquad \mathcal{L}^3(\Omega^h(t)) = \mathcal{L}^3(\Omega^h(0))\,. \qquad (3.18)$$

Here we note that (3.18) can be equivalently formulated as

$$A(\vec{X}^h(t)) = A(\vec{X}^h(0))\,, \qquad (3.19a)$$

$$V(\vec{X}^h(t)) = V(\vec{X}^h(0))\,, \qquad V(\vec{Z}^h) = -\pi\left((\vec{Z}^h.\vec{e}_1)^2, [\vec{Z}_\rho^h]^\perp.\vec{e}_1\right) \quad \vec{Z}^h \in \underline{V}_\partial^h\,, \qquad (3.19b)$$

where we have recalled (3.5), (3.3) and (3.10).

4. Fully discrete schemes

Let $0 = t_0 < t_1 < \ldots < t_{M-1} < t_M = T$ be a partitioning of $[0,T]$ into possibly variable time steps $\Delta t_m = t_{m+1} - t_m$, $m = 0 \to M - 1$. We set $\Delta t = \max_{m=0\to M-1} \Delta t_m$. For a given $\vec{X}^m \in \underline{V}_{\partial_0}^h$ we set $\vec{\nu}^m = -\frac{[\vec{X}_\rho^m]^\perp}{|\vec{X}_\rho^m|}$. Let $\vec{\omega}^m \in \underline{V}^h$ be the natural fully discrete analogue of $\vec{\omega}^h \in \underline{V}^h$, recall (3.4).

Similarly to (3.8), and given a $\kappa^{m+1} \in V^h$, we introduce $\mathfrak{R}^m(\kappa^{m+1}) \in V^h$ such that

$$[\mathfrak{R}^m(\kappa^{m+1})](q_j) = \begin{cases} \dfrac{\vec{\omega}^m(q_j).\vec{e}_1}{\vec{X}^m(q_j).\vec{e}_1} & q_j \in \overline{I} \setminus \partial_0 I\,, \\ -\kappa^{m+1}(q_j) & q_j \in \partial_0 I\,. \end{cases}$$

13

4.1. Surface diffusion

Our fully discrete analogue of the scheme $(\mathcal{E}_h)^{(h)}$, (3.9), is given as follows.

$(\mathcal{E}_m)^{(h)}$: Let $\vec{X}^0 \in \underline{V}^h_{\partial_0}$. For $m = 0, \ldots, M-1$, find $(\delta \vec{X}^{m+1}, \kappa^{m+1}) \in \underline{V}^h_\partial \times V^h$, where $\vec{X}^{m+1} = \vec{X}^m + \delta \vec{X}^{m+1}$, such that

$$\left(\vec{X}^m . \vec{e}_1 \frac{\vec{X}^{m+1} - \vec{X}^m}{\Delta t_m}, \chi \, \vec{v}^m \, |\vec{X}^m_\rho| \right)^{(h)} = \left(\vec{X}^m . \vec{e}_1 \left[\kappa^{m+1} - \mathfrak{R}^m(\kappa^{m+1}) \right]_\rho, \chi_\rho \, |\vec{X}^m_\rho|^{-1} \right) \qquad \forall \chi \in V^h, \tag{4.1a}$$

$$\left(\kappa^{m+1} \, \vec{v}^m, \vec{\eta} \, |\vec{X}^m_\rho| \right)^{(h)} + \left(\vec{X}^{m+1}_\rho, \vec{\eta}_\rho \, |\vec{X}^m_\rho|^{-1} \right) = - \sum_{i=1}^2 \sum_{p \in \partial_i I} \widehat{\varrho}^{(p)}_{\partial S} \, \vec{\eta}(p) . \vec{e}_{3-i} \qquad \forall \vec{\eta} \in \underline{V}^h_\partial. \tag{4.1b}$$

We note that it does not appear possible to prove the existence of a unique solution to $(\mathcal{E}_m)^{(h)}$. However, despite the lack of a mathematical proof, in practice the linear system (4.1) is always invertible.

Our fully discrete analogues of the scheme $(\mathcal{F}_h)^{(h)}$, (3.13), are given as follows.

$(\mathcal{F}_m)^{(h)}$: Let $\vec{X}^0 \in \underline{V}^h_{\partial_0}$. For $m = 0, \ldots, M-1$, find $(\delta \vec{X}^{m+1}, \kappa^{m+1}_S) \in \underline{V}^h_\partial \times V^h$, where $\vec{X}^{m+1} = \vec{X}^m + \delta \vec{X}^{m+1}$, such that

$$\left(\vec{X}^m . \vec{e}_1 \frac{\vec{X}^{m+1} - \vec{X}^m}{\Delta t_m}, \chi \, \vec{v}^m \, |\vec{X}^m_\rho| \right)^{(h)} = \left(\vec{X}^m . \vec{e}_1 \left[\kappa^{m+1}_S \right]_\rho, \chi_\rho \, |\vec{X}^m_\rho|^{-1} \right) \qquad \forall \chi \in V^h, \tag{4.2a}$$

$$\left(\vec{X}^m . \vec{e}_1 \, \kappa^{m+1}_S \, \vec{v}^m, \vec{\eta} \, |\vec{X}^m_\rho| \right)^{(h)} + \left(\vec{\eta} . \vec{e}_1, |\vec{X}^m_\rho| \right) + \left((\vec{X}^m . \vec{e}_1) \, \vec{X}^{m+1}_\rho, \vec{\eta}_\rho \, |\vec{X}^m_\rho|^{-1} \right)$$

$$= - \sum_{i=1}^2 \sum_{p \in \partial_i I} \widehat{\varrho}^{(p)}_{\partial S} \, (\vec{X}^m(p) . \vec{e}_1) \, \vec{\eta}(p) . \vec{e}_{3-i} \qquad \forall \vec{\eta} \in \underline{V}^h_\partial. \tag{4.2b}$$

For the second variant, which is going to lead to systems of nonlinear equations and for which a stability result can be shown, we introduce the notation $[r]_\pm = \pm \max\{\pm r, 0\}$ for $r \in \mathbb{R}$.

$(\mathcal{F}_{m,\star})^{(h)}$: Let $\vec{X}^0 \in \underline{V}^h_{\partial_0}$. For $m = 0, \ldots, M-1$, find $(\delta \vec{X}^{m+1}, \kappa^{m+1}_S) \in \underline{V}^h_\partial \times V^h$, where $\vec{X}^{m+1} = \vec{X}^m + \delta \vec{X}^{m+1}$, such that

$$\left(\vec{X}^m . \vec{e}_1 \frac{\vec{X}^{m+1} - \vec{X}^m}{\Delta t_m}, \chi \, \vec{v}^m \, |\vec{X}^m_\rho| \right)^{(h)} = \left(\vec{X}^m . \vec{e}_1 \left[\kappa^{m+1}_S \right]_\rho, \chi_\rho \, |\vec{X}^m_\rho|^{-1} \right) \qquad \forall \chi \in V^h, \tag{4.3a}$$

$$\left(\vec{X}^m . \vec{e}_1 \, \kappa^{m+1}_S \, \vec{v}^m, \vec{\eta} \, |\vec{X}^m_\rho| \right)^{(h)} + \left(\vec{\eta} . \vec{e}_1, |\vec{X}^{m+1}_\rho| \right) + \left((\vec{X}^m . \vec{e}_1) \, \vec{X}^{m+1}_\rho, \vec{\eta}_\rho \, |\vec{X}^m_\rho|^{-1} \right)$$

$$= - \sum_{p \in \partial_1 I} \widehat{\varrho}^{(p)}_{\partial S} \, (\vec{X}^m(p) . \vec{e}_1) \, \vec{\eta}(p) . \vec{e}_2 - \sum_{p \in \partial_2 I} (([\widehat{\varrho}^{(p)}_{\partial S}]_+ \, \vec{X}^{m+1}(p) + [\widehat{\varrho}^{(p)}_{\partial S}]_- \, \vec{X}^m(p)) . \vec{e}_1) \, \vec{\eta}(p) . \vec{e}_1 \qquad \forall \vec{\eta} \in \underline{V}^h_\partial. \tag{4.3b}$$

We state the following mild assumptions.

$(\mathfrak{A})$ Let $|\vec{X}^m_\rho| > 0$ for almost all $\rho \in I$, and let $\vec{X}^m . \vec{e}_1 > 0$ for all $\rho \in \overline{I} \setminus \partial_0 I$.

$(\mathfrak{B})^{(h)}$ Let $\mathcal{Z}^{(h)} = \left\{ \left((\vec{X}^m . \vec{e}_1) \, \vec{v}^m, \chi \, |\vec{X}^m_\rho| \right)^{(h)} : \chi \in V^h \right\} \subset \mathbb{R}^2$ and assume that $\dim \operatorname{span} \mathcal{Z}^{(h)} = 2$.

Note that the assumption $(\mathfrak{B})^h$, on recalling (3.4), is equivalent to assuming that $\dim \operatorname{span}\{\vec{\omega}^m(q_j)\}_{j=1,\ldots,J} = 2$.

Lemma 4.1. *Let* $\vec{X}^m \in \underline{V}^h_{\partial_0}$ *satisfy the assumptions* $(\mathfrak{A})$ *and* $(\mathfrak{B})^{(h)}$. *Then there exists a unique solution* $(\delta \vec{X}^{m+1}, \kappa^{m+1}_S) \in \underline{V}^h_\partial \times V^h$ *to* $(\mathcal{F}_m)^{(h)}$.

Proof. As (4.2) is linear, existence follows from uniqueness. To investigate the latter, we consider the system: Find $(\delta \vec{X}, \kappa_S) \in \underline{V}^h_\partial \times V^h$ such that

$$\left(\vec{X}^m . \vec{e}_1 \frac{\delta \vec{X}}{\Delta t_m}, \chi \, \vec{v}^m \, |\vec{X}^m_\rho| \right)^{(h)} = \left(\vec{X}^m . \vec{e}_1 \, [\kappa_S]_\rho, \chi_\rho \, |\vec{X}^m_\rho|^{-1} \right) \qquad \forall \chi \in V^h, \tag{4.4a}$$

$$\left(\vec{X}^m . \vec{e}_1 \, \kappa_S \, \vec{v}^m, \vec{\eta} \, |\vec{X}^m_\rho| \right)^{(h)} + \left((\vec{X}^m . \vec{e}_1) \, (\delta \vec{X})_\rho, \vec{\eta}_\rho \, |\vec{X}^m_\rho|^{-1} \right) = 0 \qquad \forall \vec{\eta} \in \underline{V}^h_\partial. \tag{4.4b}$$

14

Choosing $\chi = \kappa_S \in V^h$ in (4.4a) and $\vec{\eta} = \delta\vec{X} \in \underline{V}^h_\partial$ in (4.4b) yields that

$$\Delta t_m \left(\vec{X}^m . \vec{e}_1 \, |(\delta\vec{X})_\rho|^2, |\vec{X}^m_\rho|^{-1} \right) + \left(\vec{X}^m . \vec{e}_1 \, |[\kappa_S]_\rho|^2, |\vec{X}^m_\rho|^{-1} \right) = 0 \,. \tag{4.5}$$

It follows from (4.5) and the assumption ($\mathfrak{A}$) that $\kappa_S = \kappa^c \in \mathbb{R}$ and $\delta\vec{X} \equiv \vec{X}^c \in \mathbb{R}^2$. Hence it follows from (4.4a) that $\vec{X}^c . \vec{z} = 0$ for all $\vec{z} \in \mathcal{Z}^{(h)}$, and so assumption ($\mathfrak{B}$)$^{(h)}$ yields that $\vec{X}^c = \vec{0}$. Similarly, it follows from (4.4b) and the fact that $\mathcal{Z}^{(h)}$ must contain a nonzero vector that $\kappa^c = 0$. Hence we have shown that (4.2) has a unique solution $(\delta\vec{X}^{m+1}, \kappa_S^{m+1}) \in \underline{V}^h_\partial \times V^h$. □

For the scheme $(\mathcal{F}_{m,\star})^{(h)}$ it does not appear possible to prove existence of a solution. However, despite the lack of a mathematical proof, in practice we are always able to find a solution with the help of a Newton method.

Theorem 4.2. *Let $\vec{X}^m \in \underline{V}^h_{\partial_0}$ satisfy the assumption ($\mathfrak{A}$), and let $(\vec{X}^{m+1}, \kappa_S^{m+1})$ be a solution to $(\mathcal{F}_{m,\star})^{(h)}$. Then it holds that*

$$E(\vec{X}^{m+1}) + 2\pi\,\Delta t_m \left(\vec{X}^m . \vec{e}_1 \, |[\kappa_S^{m+1}]_\rho|^2, |\vec{X}^m_\rho|^{-1} \right) \le E(\vec{X}^m) \,. \tag{4.6}$$

Proof. Choosing $\chi = \Delta t_m \kappa_S^{m+1}$ in (4.3a) and $\vec{\eta} = \vec{X}^{m+1} - \vec{X}^m \in \underline{V}^h_\partial$ in (4.3b) yields, on noting that $\vec{X}^m(p).\vec{e}_1 = \vec{X}^{m+1}(p).\vec{e}_1$ for $p \in \partial_1 I$, that

$$
\begin{aligned}
-\Delta t_m \left(\vec{X}^m . \vec{e}_1 \, |[\kappa_S^{m+1}]_\rho|^2, |\vec{X}^m_\rho|^{-1} \right) &= \left(\vec{X}^{m+1} - \vec{X}^m, \vec{e}_1 \, |\vec{X}^{m+1}_\rho| \right) + \left((\vec{X}^m . \vec{e}_1)\,(\vec{X}^{m+1} - \vec{X}^m)_\rho, \vec{X}^{m+1}_\rho \, |\vec{X}^m_\rho|^{-1} \right) \\
&\quad + \sum_{p \in \partial_1 I} \widehat{\varrho}^{(p)}_{\partial S}\,(\vec{X}^m(p).\vec{e}_1)\,(\vec{X}^{m+1}(p) - \vec{X}^m(p)).\vec{e}_2 \\
&\quad + \sum_{p \in \partial_2 I} ([\widehat{\varrho}^{(p)}_{\partial S}]_+ \vec{X}^{m+1}(p) + [\widehat{\varrho}^{(p)}_{\partial S}]_- \vec{X}^m(p)].\vec{e}_1)\,(\vec{X}^{m+1}(p) - \vec{X}^m(p)).\vec{e}_1 \\
&\ge \left(\vec{X}^{m+1} - \vec{X}^m, \vec{e}_1 \, |\vec{X}^{m+1}_\rho| \right) + \left(\vec{X}^m . \vec{e}_1, |\vec{X}^{m+1}_\rho| - |\vec{X}^m_\rho| \right) \\
&\quad + \sum_{p \in \partial_1 I} \widehat{\varrho}^{(p)}_{\partial S}\,(\vec{X}^m(p).\vec{e}_1)\,\vec{X}^{m+1}(p).\vec{e}_2 - \sum_{p \in \partial_1 I} \widehat{\varrho}^{(p)}_{\partial S}\,(\vec{X}^m(p).\vec{e}_1)\,\vec{X}^m(p).\vec{e}_2 \\
&\quad + \tfrac{1}{2}\sum_{p \in \partial_2 I} [\widehat{\varrho}^{(p)}_{\partial S}]_+ (\vec{X}^{m+1}(p).\vec{e}_1)^2 - \tfrac{1}{2}\sum_{p \in \partial_2 I} [\widehat{\varrho}^{(p)}_{\partial S}]_+ (\vec{X}^m(p).\vec{e}_1)^2 \\
&\quad + \tfrac{1}{2}\sum_{p \in \partial_2 I} [\widehat{\varrho}^{(p)}_{\partial S}]_- (\vec{X}^{m+1}(p).\vec{e}_1)^2 - \tfrac{1}{2}\sum_{p \in \partial_2 I} [\widehat{\varrho}^{(p)}_{\partial S}]_- (\vec{X}^m(p).\vec{e}_1)^2 \\
&= \left(\vec{X}^{m+1} . \vec{e}_1, |\vec{X}^{m+1}_\rho| \right) - \left(\vec{X}^m . \vec{e}_1, |\vec{X}^m_\rho| \right) \\
&\quad + \sum_{p \in \partial_1 I} \widehat{\varrho}^{(p)}_{\partial S}\,(\vec{X}^{m+1}(p).\vec{e}_1)\,\vec{X}^{m+1}(p).\vec{e}_2 - \sum_{p \in \partial_1 I} \widehat{\varrho}^{(p)}_{\partial S}\,(\vec{X}^m(p).\vec{e}_1)\,\vec{X}^m(p).\vec{e}_2 \\
&\quad + \tfrac{1}{2}\sum_{p \in \partial_2 I} \widehat{\varrho}^{(p)}_{\partial S}\,(\vec{X}^{m+1}(p).\vec{e}_1)^2 - \tfrac{1}{2}\sum_{p \in \partial_2 I} \widehat{\varrho}^{(p)}_{\partial S}\,(\vec{X}^m(p).\vec{e}_1)^2 \\
&= \frac{1}{2\pi}\,E(\vec{X}^{m+1}) - \frac{1}{2\pi}\,E(\vec{X}^m) \,,
\end{aligned}
$$

where we have used the two inequalities $\vec{a}.(\vec{a} - \vec{b}) \ge |\vec{b}|\,(|\vec{a}| - |\vec{b}|)$ for $\vec{a}, \vec{b} \in \mathbb{R}^2$, and $2\beta\,(\beta - \alpha) \ge \beta^2 - \alpha^2$ for $\alpha, \beta \in \mathbb{R}$. This proves the desired result (4.6). □

4.2. Intermediate evolution law

It is straightforward to adapt the schemes $(\mathcal{E}_m)^h$, $(\mathcal{F}_m)^{(h)}$ and $(\mathcal{F}_{m,\star})^{(h)}$ to the flow (1.5). For example, $(\mathcal{F}_{m,\star})^{(h)}$ can be adapted to yield the following fully discrete approximation of $(\mathcal{I}_h)^{(h)}$, (3.15).

$(\mathcal{I}_{m,\star})^{(h)}$: Let $\vec{X}^0 \in \underline{V}^h_{\partial_0}$. For $m = 0, \ldots, M-1$, find $(\delta\vec{X}^{m+1}, Y^{m+1}, \kappa_S^{m+1}) \in \underline{V}^h_\partial \times [V^h]^2$, where $\vec{X}^{m+1} = \vec{X}^m + \delta\vec{X}^{m+1}$, such that

$$\left(\vec{X}^m . \vec{e}_1 \frac{\vec{X}^{m+1} - \vec{X}^m}{\Delta t_m}, \chi \, \vec{v}^m \, |\vec{X}^m_\rho| \right)^{(h)} = \left(\vec{X}^m . \vec{e}_1 \, Y^{m+1}, \chi_\rho \, |\vec{X}^m_\rho|^{-1} \right) \qquad \forall \, \chi \in V^h, \tag{4.7a}$$

$$\frac{1}{\xi} \left(\vec{X}^m . \vec{e}_1 \, Y_\rho^{m+1}, \zeta_\rho \, |\vec{X}^m_\rho|^{-1} \right) + \left(\vec{X}^m . \vec{e}_1 \left[\alpha^{-1} \, Y^{m+1} - \kappa_S^{m+1} \right], \zeta \, |\vec{X}^m_\rho| \right)^{(h)} = 0 \qquad \forall \, \zeta \in V^h, \tag{4.7b}$$

$$\left(\vec{X}^m . \vec{e}_1 \, \kappa_S^{m+1} \, \vec{v}^m, \vec{\eta} \, |\vec{X}^m_\rho| \right)^{(h)} + \left(\vec{\eta} . \vec{e}_1, |\vec{X}^m_\rho| \right) + \left((\vec{X}^m . \vec{e}_1) \, \vec{X}^{m+1}_\rho, \vec{\eta}_\rho \, |\vec{X}^m_\rho|^{-1} \right)$$

$$= - \sum_{p \in \partial_1 I} \widehat{\vec{\varrho}}^{(p)}_{\partial S} \, (\vec{X}^m(p) . \vec{e}_1) \, \vec{\eta}(p) . \vec{e}_2 - \sum_{p \in \partial_2 I} (([\widehat{\vec{\varrho}}^{(p)}_{\partial S}]_+ \, \vec{X}^{m+1}(p) + [\widehat{\vec{\varrho}}^{(p)}_{\partial S}]_- \, \vec{X}^m(p)) . \vec{e}_1) \, \vec{\eta}(p) . \vec{e}_1 \qquad \forall \, \vec{\eta} \in \underline{V}^h_\partial. \tag{4.7c}$$

Theorem 4.3. *Let $\vec{X}^m \in \underline{V}^h_{\partial_0}$ satisfy the assumption* ($\mathfrak{A}$)*, and let* $(\vec{X}^{m+1}, Y^{m+1}, \kappa_S^{m+1})$ *be a solution to* $(\mathcal{I}_{m,\star})^{(h)}$*. Then it holds that*

$$E(\vec{X}^{m+1}) + \frac{2\pi \Delta t_m}{\alpha} \left(\vec{X}^m . \vec{e}_1 \, |[Y^{m+1}]_\rho|^2, |\vec{X}^m_\rho|^{-1} \right) + 2\pi \Delta t_m \, \xi \left(\vec{X}^m . \vec{e}_1 \, |\kappa_S^{m+1} - \tfrac{1}{\alpha} \, Y^{m+1}|^2, |\vec{X}^m_\rho| \right)^{(h)} \le E(\vec{X}^m). \tag{4.8}$$

Proof. The proof is a simple adaptation of the proof of Theorem 4.2. In particular, choosing $\chi = \Delta t_m \frac{\alpha}{\xi} \kappa_S^{m+1}$ in (4.7a), $\zeta = \Delta t_m \, \alpha \, \kappa_S^{m+1} - Y^{m+1}$ in (4.7b) and $\vec{\eta} = \vec{X}^{m+1} - \vec{X}^m \in \underline{V}^h_\partial$ in (4.7c) yields (4.8). $\qquad \square$

4.3. Willmore flow

Our fully discrete analogue of the scheme $(\mathcal{W}_h)^h$, (3.16), is given as follows.

$(\mathcal{W}_m)^h$: Let $\vec{X}^0 \in \underline{V}^h_\partial$ and $\kappa^0 \in V^h$. For $m = 0, \ldots, M-1$, find $(\vec{X}^{m+1}, \kappa^{m+1}) \in \underline{V}^h_\partial \times V^h$ such that

$$\left(\vec{X}^m . \vec{e}_1 \frac{\vec{X}^{m+1} - \vec{X}^m}{\Delta t_m}, \chi \, \vec{v}^m \, |\vec{X}^m_\rho| \right)^h - \left(\vec{X}^m . \vec{e}_1 \left[\kappa^{m+1} - \mathfrak{R}^m(\kappa^{m+1}) \right]_\rho, \chi_\rho \, |\vec{X}^m_\rho|^{-1} \right)$$

$$= -2 \left(\left[\kappa^m - \frac{\vec{\omega}^m . \vec{e}_1}{\vec{X}^m . \vec{e}_1} - \overline{\varkappa} \right] \kappa^m \, \vec{\omega}^m . \vec{e}_1, \chi \, |\vec{X}^m_\rho| \right)^h - \frac{1}{2} \left(\vec{X}^m . \vec{e}_1 \left(\left[\kappa^m - \frac{\vec{\omega}^m . \vec{e}_1}{\vec{X}^m . \vec{e}_1} \right]^2 - \overline{\varkappa}^2 \right) \left[\kappa^m - \frac{\vec{\omega}^m . \vec{e}_1}{\vec{X}^m . \vec{e}_1} \right], \chi \, |\vec{X}^m_\rho| \right)^h$$

$$\forall \, \chi \in V^h, \tag{4.9a}$$

$$\left(\kappa^{m+1} \, \vec{v}^m, \vec{\eta} \, |\vec{X}^m_\rho| \right)^h + \left(\vec{X}^{m+1}_\rho, \vec{\eta}_\rho \, |\vec{X}^m_\rho|^{-1} \right) = 0 \qquad \forall \, \vec{\eta} \in \underline{V}^h_\partial. \tag{4.9b}$$

We note that, similarly to $(\mathcal{E}_m)^h$, it does not appear possible to prove existence and uniqueness of a solution to $(\mathcal{W}_m)^h$. However, despite the lack of a mathematical proof, in practice the linear systems (4.9) are always invertible.

4.3.1. Helfrich flow

We re-write (4.9a) as

$$\left(\vec{X}^m . \vec{e}_1 \frac{\vec{X}^{m+1} - \vec{X}^m}{\Delta t_m}, \chi \, \vec{v}^m \, |\vec{X}^m_\rho| \right)^h - \left(\vec{X}^m . \vec{e}_1 \left[\kappa^{m+1} - \mathfrak{R}^m(\kappa^{m+1}) \right]_\rho, \chi_\rho \, |\vec{X}^m_\rho|^{-1} \right) = \left(f^m, \chi \, |\vec{X}^m_\rho| \right)^h.$$

Then our fully discrete analogue of the scheme $(\mathcal{W}_h^{A,V})^h$, (3.17), (3.19), is given as follows.

$(\mathcal{W}_m^{A,V})^h$: Let $\vec{X}^0 \in \underline{V}^h_\partial$ and $\kappa^0 \in V^h$. For $m = 0, \ldots, M-1$, find $(\vec{X}^{m+1}, \kappa^{m+1}, \lambda_A^{m+1}, \lambda_V^{m+1}) \in \underline{V}^h_\partial \times V^h \times \mathbb{R}^2$ such that (4.9b) and

$$\left(\vec{X}^m . \vec{e}_1 \frac{\vec{X}^{m+1} - \vec{X}^m}{\Delta t_m}, \chi \, \vec{v}^m \, |\vec{X}^m_\rho| \right)^h - \left(\vec{X}^m . \vec{e}_1 \left[\kappa^{m+1} - \mathfrak{R}^m(\kappa^{m+1}) \right]_\rho, \chi_\rho \, |\vec{X}^m_\rho|^{-1} \right)$$

$$= \left(f^m, \chi \, |\vec{X}^m_\rho| \right) + \lambda_A^{m+1} \left(\vec{X}^m . \vec{e}_1 \left[\kappa^m - \mathfrak{R}^m(\kappa^m) \right], \chi \, |\vec{X}^m_\rho| \right)^h + \lambda_V^{m+1} \left(\vec{X}^m . \vec{e}_1, \chi \, |\vec{X}^m_\rho| \right)^h \qquad \forall \, \chi \in V^h, \tag{4.10a}$$

$$A(\vec{X}^{m+1}) = A(\vec{X}^0), \quad V(\vec{X}^{m+1}) = V(\vec{X}^0), \tag{4.10b}$$

16

hold, where we have recalled (3.19). The system (4.10) can be solved with a suitable nonlinear solution method, see below. In the simpler case of surface area conserving Willmore flow, we need to find $(\vec{X}^{m+1}, \kappa^{m+1}, \lambda_A^{m+1}, \lambda_V^{m+1}) \in \underline{V}_\partial^h \times V^h \times \mathbb{R} \times \{0\}$ such that (4.10) hold. Similarly, for volume conserving Willmore flow, we need to find $(\vec{X}^{m+1}, \kappa^{m+1}, \lambda_A^{m+1}, \lambda_V^{m+1}) \in \underline{V}_\partial^h \times V^h \times \{0\} \times \mathbb{R}$ such that (4.10) hold.

Adapting the strategy in [30], we now describe a Newton method for solving the nonlinear system (4.10). The linear system (4.10a) and (4.9b), with $(\lambda_A^{m+1}, \lambda_V^{m+1})$ in (4.10a) replaced by (λ_A, λ_V), can be written as: Find $(\vec{X}^{m+1}(\lambda_A, \lambda_V), \kappa^{m+1}(\lambda_A, \lambda_V)) \in \underline{V}_\partial^h \times V^h$ such that

$$\mathbb{T}^m \begin{pmatrix} \kappa^{m+1}(\lambda_A, \lambda_V) \\ \vec{X}^{m+1}(\lambda_A, \lambda_V) \end{pmatrix} = \begin{pmatrix} \underline{\mathfrak{g}}^m \\ \vec{0} \end{pmatrix} + \lambda_A \begin{pmatrix} \underline{\mathfrak{K}}^m \\ \vec{0} \end{pmatrix} + \lambda_V \begin{pmatrix} \underline{\mathfrak{N}}^m \\ \vec{0} \end{pmatrix}. \tag{4.11}$$

Assuming the linear operator $\mathbb{T}^m$ is invertible, we obtain that

$$\begin{pmatrix} \kappa^{m+1}(\lambda_A, \lambda_V) \\ \vec{X}^{m+1}(\lambda_A, \lambda_V) \end{pmatrix} = (\mathbb{T}^m)^{-1} \left[\begin{pmatrix} \underline{\mathfrak{g}}^m \\ \vec{0} \end{pmatrix} + \lambda_A \begin{pmatrix} \underline{\mathfrak{K}}^m \\ \vec{0} \end{pmatrix} + \lambda_V \begin{pmatrix} \underline{\mathfrak{N}}^m \\ \vec{0} \end{pmatrix} \right] =: (\mathbb{T}^m)^{-1} \begin{pmatrix} \underline{\mathfrak{g}}^m \\ \vec{0} \end{pmatrix} + \lambda_A \begin{pmatrix} \underline{s}_1^m \\ \underline{\vec{s}}_2^m \end{pmatrix} + \lambda_V \begin{pmatrix} \underline{q}_1^m \\ \underline{\vec{q}}_2^m \end{pmatrix}. \tag{4.12}$$

It immediately follows from (4.12) that

$$\partial_{\lambda_A} \vec{X}^{m+1}(\lambda_A, \lambda_V) = \underline{\vec{s}}_2^m, \quad \partial_{\lambda_V} \vec{X}^{m+1}(\lambda_A, \lambda_V) = \underline{\vec{q}}_2^m.$$

Hence

$$\partial_{\lambda_A} A(\vec{X}^{m+1}(\lambda_A, \lambda_V)) = \left[\frac{\delta}{\delta \vec{X}^{m+1}} A(\vec{X}^{m+1}(\lambda_A, \lambda_V)) \right] (\vec{s}_2^m), \quad \partial_{\lambda_A} V(\vec{X}^{m+1}(\lambda_A, \lambda_V)) = \left[\frac{\delta}{\delta \vec{X}^{m+1}} V(\vec{X}^{m+1}(\lambda_A, \lambda_V)) \right] (\vec{s}_2^m),$$

and similarly for $\partial_{\lambda_V} A(\vec{X}^{m+1}(\lambda_A, \lambda_V))$ and $\partial_{\lambda_V} V(\vec{X}^{m+1}(\lambda_A, \lambda_V))$. Here $\vec{s}_2^m \in \underline{V}_\partial^h$ is the finite element function corresponding to the coefficients in $\underline{\vec{s}}_2^m$ for the standard basis of $\underline{V}^h$. Moreover, we have defined the first variation of $A(\vec{Z}^h)$, for any $\vec{Z}^h \in \underline{V}_\partial^h$, as

$$\left[\frac{\delta}{\delta \vec{Z}^h} A(\vec{Z}^h) \right] (\vec{\eta}) = \lim_{\varepsilon \to 0} \frac{1}{\varepsilon} \left(A(\vec{Z}^h + \varepsilon \vec{\eta}) - A(\vec{Z}^h) \right) = 2\pi \left(\vec{\eta} . \vec{e}_1, |\vec{Z}_\rho^h| \right) + 2\pi \left((\vec{Z}^h . \vec{e}_1) \vec{\eta}_\rho, \vec{Z}_\rho^h |\vec{Z}_\rho^h|^{-1} \right) \quad \forall \vec{\eta} \in \underline{V}_\partial^h,$$

and similarly

$$\left[\frac{\delta}{\delta \vec{Z}^h} V(\vec{Z}^h) \right] (\vec{\eta}) = \lim_{\varepsilon \to 0} \frac{1}{\varepsilon} \left(V(\vec{Z}^h + \varepsilon \vec{\eta}) - V(\vec{Z}^h) \right) = 2\pi \left(\vec{Z}^h . \vec{e}_1, \vec{\eta} . [\vec{Z}_\rho^h]^\perp \right) \quad \forall \vec{\eta} \in \underline{V}_\partial^h.$$

For a given iterate $(\lambda_A^k, \lambda_V^k)$, with corresponding $\vec{X}^{m+1,k} = \vec{X}^{m+1}(\lambda_A^k, \lambda_V^k)$ and $\kappa^{m+1,k} = \kappa^{m+1}(\lambda_A^k, \lambda_V^k)$, we now define the following quantities.

$$[\underline{\vec{k}}^{m+1,k}]_i = \left(\left[\frac{\delta}{\delta \vec{X}^{m+1,k}} A(\vec{X}^{m+1,k}) \right] (\chi_i \vec{e}_\ell) \right)_{\ell=1}^2, \quad [\underline{\vec{n}}^{m+1,k}]_i = \left(\left[\frac{\delta}{\delta \vec{X}^{m+1,k}} V(\vec{X}^{m+1,k}) \right] (\chi_i \vec{e}_\ell) \right)_{\ell=1}^2.$$

Then the Newton update is given by

$$\begin{pmatrix} \lambda_A^{k+1} \\ \lambda_V^{k+1} \end{pmatrix} = \begin{pmatrix} \lambda_A^k \\ \lambda_V^k \end{pmatrix} - \begin{pmatrix} \underline{\vec{k}}^{m+1,k} . \underline{\vec{s}}_2^m & \underline{\vec{k}}^{m+1,k} . \underline{\vec{q}}_2^m \\ \underline{\vec{n}}^{m+1,k} . \underline{\vec{s}}_2^m & \underline{\vec{n}}^{m+1,k} . \underline{\vec{q}}_2^m \end{pmatrix}^{-1} \begin{pmatrix} A(\vec{X}^{m+1,k}) - A(\vec{X}^0) \\ V(\vec{X}^{m+1,k}) - V(\vec{X}^0) \end{pmatrix}. \tag{4.13}$$

In practice, the linear systems (4.11) are always invertible, and the Newton iteration (4.13) converges within a couple of iterations.
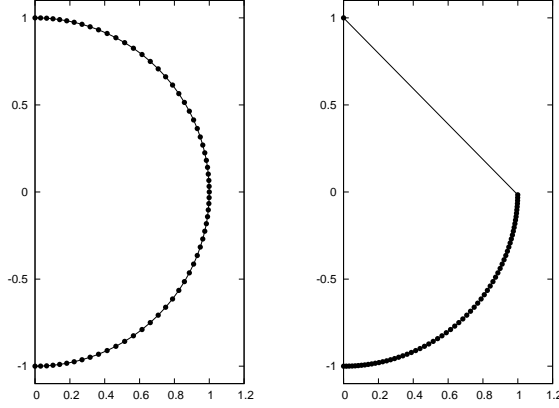
Figure 2: Initial data $\vec{X}^0$ approximating a semicircle with $J = 64$. The initial ratios (5.1) are $\mathfrak{r}^0 = 1.94$ and $\mathfrak{r}^0 = 89.81$, respectively.

5. Numerical results

As the fully discrete energy, we consider $E(\vec{X}^m)$, recall (3.6). Unless otherwise stated, we choose $\widehat{\varrho}_{\partial S}^{(0)} = \widehat{\varrho}_{\partial S}^{(1)} = 0$. We always employ uniform time steps, $\Delta t_m = \Delta t$, $m = 0, \ldots, M - 1$.

We also consider the ratio

$$\mathfrak{r}^m = \frac{\max_{j=1 \to J} |\vec{X}^m(q_j) - \vec{X}^m(q_{j-1})|}{\min_{j=1 \to J} |\vec{X}^m(q_j) - \vec{X}^m(q_{j-1})|} \tag{5.1}$$

between the longest and shortest element of Γ^m, and are often interested in the evolution of this ratio over time.

In practice, we stop the computation when $\vec{X}^m < 0$ for some $\rho \in \bar{I}$, as the computed results would then no longer be physical. However, for sufficiently small discretization parameters this happens only once the computation reaches a singularity for the underlying flow.

5.1. Numerical results for surface diffusion

5.1.1. Sphere

Clearly, a sphere is a stationary solution for surface diffusion. Hence, setting $\partial_0 I = \partial I = \{0, 1\}$ and choosing as initial data $\vec{X}^0$ the approximations of a semicircle displayed in Figure 2, we now investigate the different tangential motions exhibited by the six schemes $(\mathcal{E}_m)^h$, $(\mathcal{E}_m)$, $(\mathcal{F}_m)^h$, $(\mathcal{F}_m)$, $(\mathcal{F}_{m,\star})^h$ and $(\mathcal{F}_{m,\star})$. We set $\Delta t = 10^{-4}$ and integrate the evolution for the initial data on the left of Figure 2 until time $T = 1$, see Figure 3. Of the six schemes, only $(\mathcal{F}_m)^h$ breaks down before reaching the final time. When $(\mathcal{F}_m)^h$ breaks down due to vertices moving to the left of the x_2–axis, the element ratio $\mathfrak{r}^m$ has reached a value of 6058. Hence it appears that $(\mathcal{F}_m)^h$ exhibits an implicit tangential motion towards the x_2–axis, which can lead to coalescence of vertices or to vertices on the left of the x_2–axis. For this reason we do not consider the scheme $(\mathcal{F}_m)^h$ any further. For the remaining five schemes $(\mathcal{E}_m)^h$, $(\mathcal{E}_m)$, $(\mathcal{F}_m)$, $(\mathcal{F}_{m,\star})^h$, $(\mathcal{F}_{m,\star})$ the element ratios $\mathfrak{r}^m$ at time $T = 1$ are $1.00, 1.00, 3.04, 62.21, 3.05$, and the enclosed volume is preserved almost exactly by all the schemes. We show the final distributions of vertices, and plots of $\mathfrak{r}^m$ over time in Figure 3. In addition, we show plots of the $\mathfrak{r}^m$ for the scheme $(\mathcal{F}_{m,\star})$ for different time step sizes in Figure 4. In these experiments it appears that the element ratio asymptotically approaches a value close to 3. The same plots for the scheme $(\mathcal{E}_m)^h$ show $\mathfrak{r}^m$ monotonically decreasing to the value 1 by virtue of the equidistribution property (3.14), with the decrease faster for smaller time step sizes Δt.

In a second set of experiments to investigate the different tangential motions induced by the individual schemes, we repeat the simulations in Figure 3 now for the initial data displayed on the right of Figure 2. We again use $J = 64$ and $\Delta t = 10^{-4}$, and show the relevant results in Figure 5. Once again the scheme $(\mathcal{F}_m)^h$ breaks down due to vertices moving to the left of the x_2–axis. For the remaining five schemes $(\mathcal{E}_m)^h$, $(\mathcal{E}_m)$, $(\mathcal{F}_m)$, $(\mathcal{F}_{m,\star})^h$, $(\mathcal{F}_{m,\star})$ the element ratios $\mathfrak{r}^m$ at time $T = 1$ are $1.06, 1.06, 3.02, 113.13, 3.07$. Due to the very nonuniform initial data, the enclosed volume is only preserved well for the three schemes without numerical integration. In particular, the relative enclosed volume losses for the five schemes are $20.6\%, -1.0\%, -0.9\%, 35.9\%, -0.7\%$.
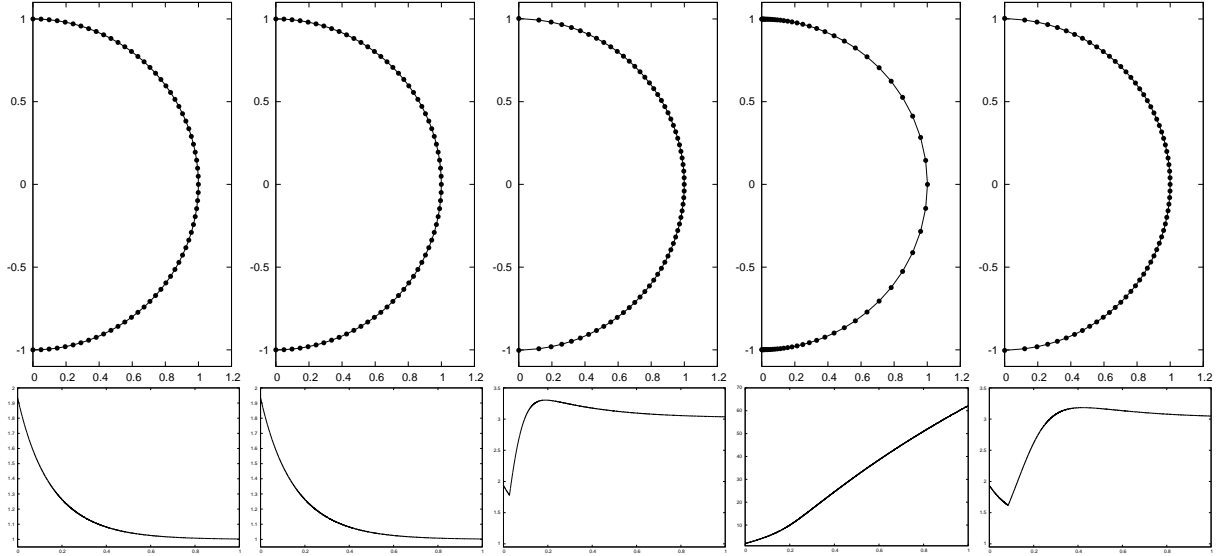
18

Figure 3: Comparison of the different schemes for surface diffusion of the unit sphere. Left to right: $(\mathcal{E}_m)^h$, $(\mathcal{E}_m)$, $(\mathcal{F}_m)$, $(\mathcal{F}_{m,\star})^h$, $(\mathcal{F}_{m,\star})$. Plots are for $\vec{X}^m$ at time $t = 1$ and for the ratio $\mathfrak{r}^m$ over time. The element ratios $\mathfrak{r}^m$ at time $t = 1$ are 1.00, 1.00, 3.04, 62.21, 3.05.
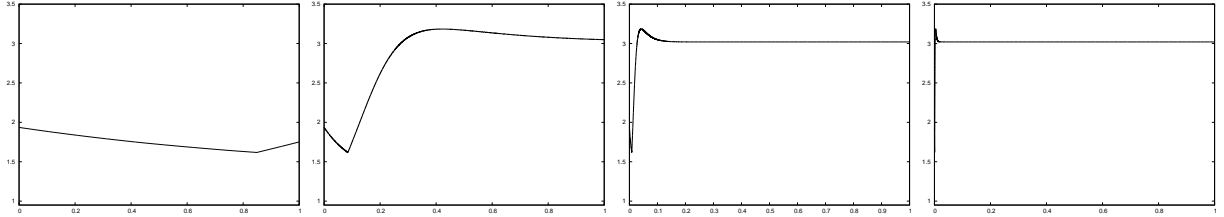
Figure 4: $(\mathcal{F}_{m,\star})$ Plots of the ratio $\mathfrak{r}^m$ for $\Delta t = 10^{-k}$, $k = 3, \dots 6$.

For the remainder of this subsection, we will only present numerical results for the two schemes $(\mathcal{E}_m)^h$ and $(\mathcal{F}_{m,\star})$. Note that the former is a linear fully discrete approximation of $(\mathcal{E}_h)^h$, for which the equidistribution property (3.14) holds. The latter, on the other hand, is a nonlinear scheme that is unconditionally stable, recall Theorem 4.2, and, the semidiscrete scheme $(\mathcal{F}_h)$ that it is based on preserves the enclosed volume exactly. As the results for $(\mathcal{E}_m)^h$ and $(\mathcal{F}_{m,\star})$ are often indistinguishable, we only visualize the numerical results for the former, and will do so from now on in this section.

5.1.2. Genus 0 surface

An experiment for a rounded cylinder of total dimension $1 \times 7 \times 1$ can be seen in Figure 6. Here we have once again that $\partial_0 I = \partial I = \{0, 1\}$. The discretization parameters are $J = 128$ and $\Delta t = 10^{-4}$. The relative volume loss for this experiment for $(\mathcal{E}_m)^h$ is 0.05%, while for $(\mathcal{F}_{m,\star})$ it is 0.00%. If we increase the aspect ratio of the initial data, then pinch-off can occur during the evolution. We visualize this effect in Figure 7, where as initial data we choose a rounded cylinder of total dimension $1 \times 8 \times 1$. The discretization parameters are as before, and the relative volume loss for $(\mathcal{E}_m)^h$ is 0.02%, while for $(\mathcal{F}_{m,\star})$ it is 0.00%. An experiment for a disc shape of total dimension $9 \times 1 \times 9$ is shown in Figure 8. The discretization parameters are $J = 128$ and $\Delta t = 10^{-3}$. The relative volume loss for this experiment for $(\mathcal{E}_m)^h$ is 0.03%, while for $(\mathcal{F}_{m,\star})$ it is 0.04%. We notice that although for the time step size $\Delta t = 10^{-3}$, the element ratio for the scheme $(\mathcal{F}_{m,\star})$ is smaller than for $(\mathcal{E}_m)^h$, this is no longer the case for smaller time step sizes. For smaller time step sizes, the ratio approaches the value 1 very quickly for the scheme $(\mathcal{E}_m)^h$, while for $(\mathcal{F}_{m,\star})$ it can reach much larger values, before eventually approaching a value closer to 4. See Figure 9 for some ratio plots for $(\mathcal{F}_{m,\star})$ when $\Delta t = 10^{-k}$, $k = 4, 5, 6$. We note that this behaviour appears to be generic for all our numerical experiments for surface diffusion.
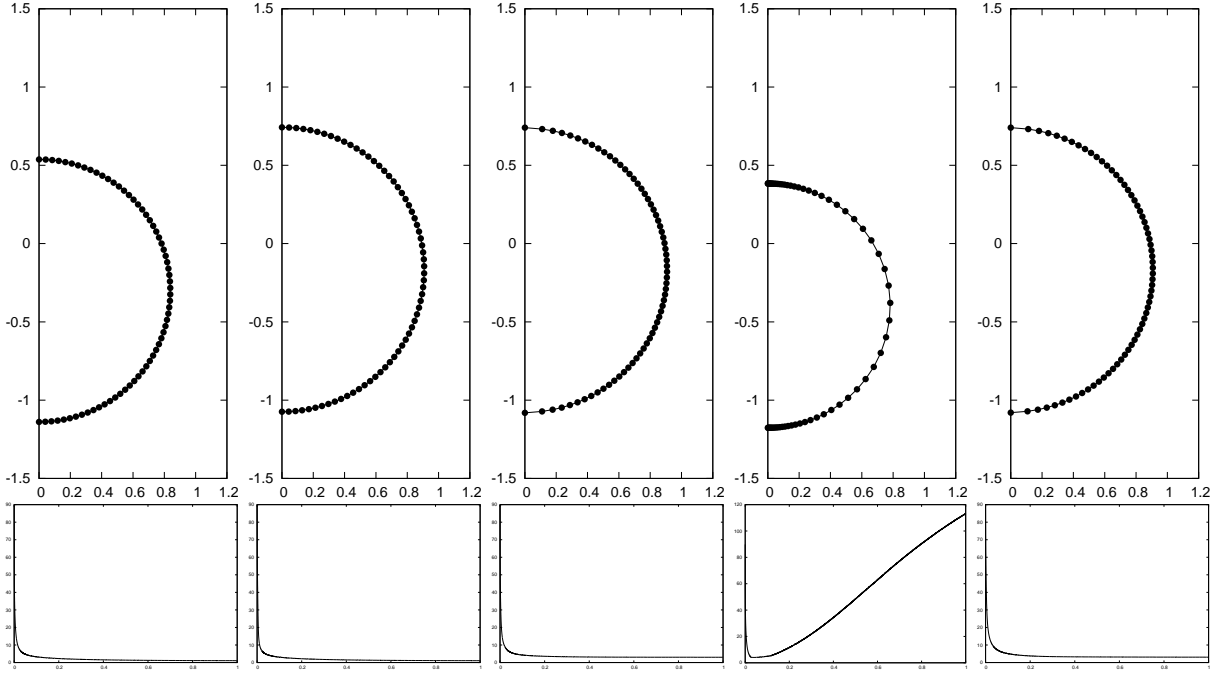
19

Figure 5: Comparison of the different schemes for surface diffusion towards a sphere. Left to right: $(\mathcal{E}_m)^h$, $(\mathcal{E}_m)$, $(\mathcal{F}_m)$, $(\mathcal{F}_{m,\star})^h$, $(\mathcal{F}_{m,\star})$. Plots are for $\vec{X}^m$ at time $t = 1$ and for the ratio $\mathfrak{r}^m$ over time. The element ratios $\mathfrak{r}^m$ at time $t = 1$ are 1.06, 1.06, 3.02, 113.13, 3.07. The relative enclosed volume losses are 20.6%, -1.0%, -0.9%, 35.9%, -0.7%.

5.1.3. Torus

In order to model the evolution of a torus, we set $I = \mathbb{R}/\mathbb{Z}$, so that $\partial I = \emptyset$. For a torus with $R = 1$, $r = 0.25$, we obtain a surface that closes up towards a genus-0 surface, as in [4, Fig. 14]. See Figure 10 for the simulation results, where we note that the surface closing up represents a singularity for the parametric approach. In particular, some vertices of $\vec{X}^m$ are approaching the x_2–axis, which leads to a moderate increase in the element ratio (5.1). The discretization parameters for this experiment are $J = 256$ and $\Delta t = 10^{-5}$. The observed relative volume loss is 0.02% for both the schemes $(\mathcal{E}_m)^h$ and $(\mathcal{F}_{m,\star})$. A detailed view of the vertex distribution at the final time, $t = 0.02392$, for the schemes $(\mathcal{E}_m)^h$ and $(\mathcal{F}_{m,\star})$ is given in Figure 11. Here we note that the element ratios $\mathfrak{r}^m$ at this time are 1.30 and 1.33, respectively. Hence the proximity of the x_2–axis has no dramatic effect on the vertex distribution.

5.1.4. Droplet on a substrate

Here we consider the evolution for a droplet on a substrate, so that e.g. $\partial_2 I = \{0\}$ and $\partial_0 I = \{1\}$. See Figure 12 for a simulation for the choice $\widehat{\varrho}_{\partial S}^{(0)} = -\frac{1}{2}$. Here we use $J = 64$ and $\Delta t = 10^{-3}$. The relative volume loss for this experiment is -0.64% for the scheme $(\mathcal{E}_m)^h$ and -0.61% for the scheme $(\mathcal{F}_{m,\star})$. The same experiment with $\widehat{\varrho}_{\partial S}^{(0)} = 0.9$ can be seen in Figure 13. The relative volume loss for this experiment is -0.13% for the scheme $(\mathcal{E}_m)^h$ and -0.10% for the scheme $(\mathcal{F}_{m,\star})$.

5.1.5. Cut genus 1 surface on a substrate

In this section, we show some experiments for the upper half of a genus 1 surface attached to the hyperplane $\mathbb{R} \times \{0\} \times \mathbb{R}$, so that $\partial_2 I = \partial I = \{0, 1\}$. See Figure 14 for an experiment with $J = 129$ and $\Delta t = 10^{-4}$. The relative volume loss for this experiment is 0.47% for the scheme $(\mathcal{E}_m)^h$ and 0.43% for the scheme $(\mathcal{F}_{m,\star})$. The same experiment with $\widehat{\varrho}_{\partial S}^{(0)} = -\widehat{\varrho}_{\partial S}^{(1)} = \frac{1}{2}$ can be seen in Figure 15. The relative volume loss for this experiment is -0.25% for both schemes $(\mathcal{E}_m)^h$ and $(\mathcal{F}_{m,\star})$.
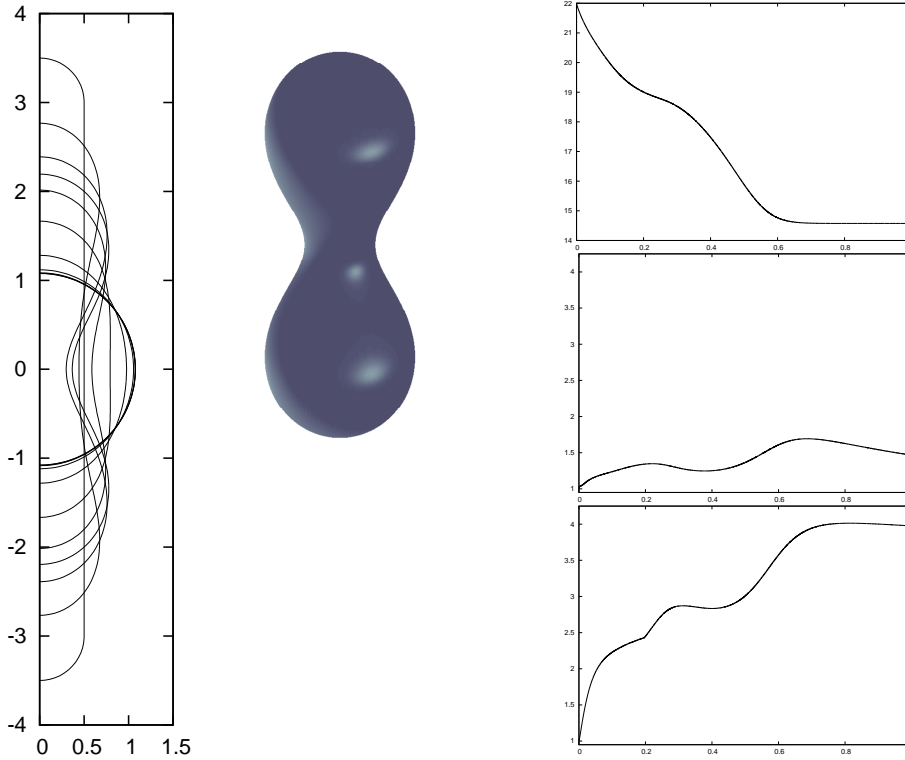
Figure 6: $(\mathcal{E}_m)^h$ Evolution for a rounded cylinder of dimension $1 \times 7 \times 1$. Plots are at times $t = 0, 0.1, \ldots, 1$. We also visualize the axisymmetric surface $\mathcal{S}^m$ generated by Γ^m at time $t = 0.3$. On the right are plots of the discrete energy and the ratio $\mathfrak{r}^m$ and, as a comparison, a plot of the ratio $\mathfrak{r}^m$ for the scheme $(\mathcal{F}_{m,\star})$.

5.1.6. Cut cylinder between two hyperplanes

In this subsection we repeat the computations in [7, Figs. 21, 22] for two open dumbbell-like cylindrical shapes attached to two parallel hyperplanes, see Figures 16 and 17, and so we let $\partial_2 I = \partial I = \{0, 1\}$. In particular, in these experiments the two components of the boundary of $\mathcal{S}^m$ are attached to two distinct parallel hyperplanes. That means that $\vec{X}^m(0)$ is attached to the x_1–axis, while $\vec{X}^m(1)$ remains on the line $\mathbb{R} \times \{a\}$, with $a = 4$ in Figure 16 and $a = 8$ in Figure 17. The initial data are given by $\Gamma(0) = \{(1 + \alpha \cos(2\pi\rho), \rho a)^T : \rho \in [0, 1]\}$, with $\alpha = 0.5$ and $\alpha = 0.25$, respectively. For the discretization parameters we choose $J = 128$ and $\Delta t = 10^{-3}$. The relative volume losses for these experiments are -0.02% and -0.01% for the scheme $(\mathcal{E}_m)^h$, and -0.01% in both cases for the scheme $(\mathcal{F}_{m,\star})$. We note that for the smaller aspect ratio of the shape in Figure 16, the evolution reaches a cylinder. For the larger aspect ratio in Figure 17 the surface would like to undergo pinch-off, which represents a singularity in the parametric approach. As a consequence, the element ratio (5.1) increases to about 1.19 for scheme $(\mathcal{E}_m)^h$, and to about 1.30 for scheme $(\mathcal{F}_{m,\star})$.

5.2. Numerical results for the intermediate evolution law

We repeat the experiment in Figure 6 for the scheme $(\mathcal{I}_{m,\star})$ to approximate the flow (1.4), rather than surface diffusion. We choose the values $\xi = \alpha = 1$, so that the flow interpolates between surface diffusion and conserved mean curvature flow. The results are shown in Figure 18, where we note the slower evolution compared to Figure 6. The discretization parameters are $J = 128$ and $\Delta t = 10^{-4}$. The relative volume loss for this experiment is 0.00%. We mention that for the fully 3d approximation [4, (2.27a–c)] of the intermediate flow (1.4), some transient mesh ringing was observed for a numerical simulation similar to Figure 18, see [4, Fig. 17]. Of course, in the axisymmetric setting considered in this paper, no such mesh effects can ever occur.
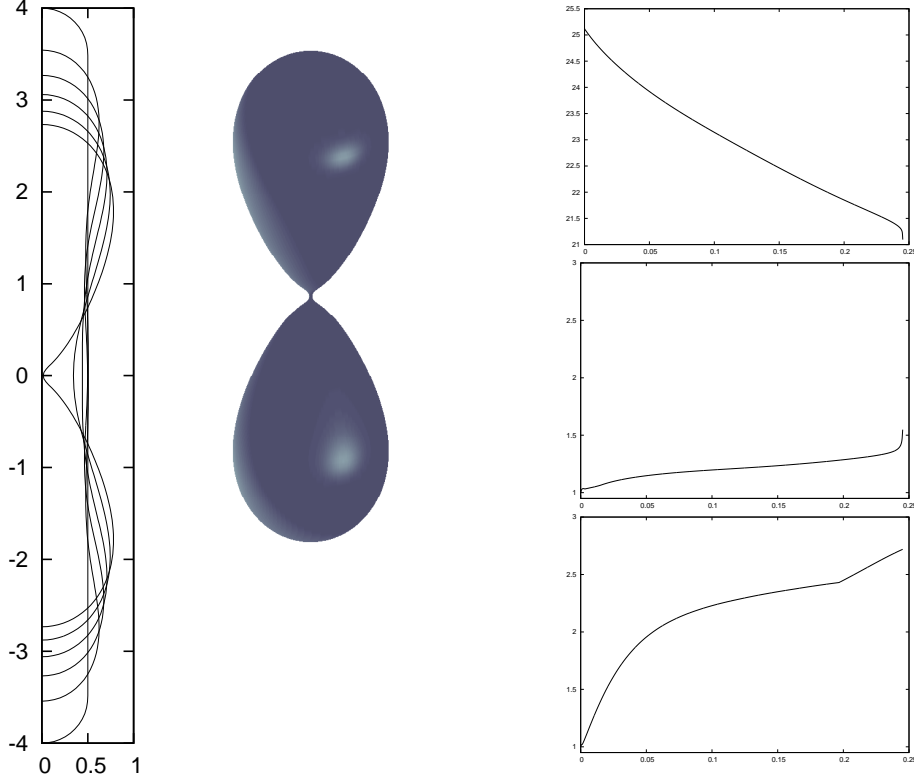
21

Figure 7: $(\mathcal{E}_m)^h$ Evolution for a rounded cylinder of dimension $1 \times 8 \times 1$. Plots are at times $t = 0, 0.05, \ldots, 0.2, 0.2452$. We also visualize the axisymmetric surface $\mathcal{S}^m$ generated by Γ^m at time $t = 0.2452$. On the right are plots of the discrete energy and the ratio $\mathfrak{r}^m$ and, as a comparison, a plot of the ratio $\mathfrak{r}^m$ for the scheme $(\mathcal{F}_{m,\star})$.

5.3. Numerical results for Willmore flow

Here present numerical results for the scheme $(\mathcal{W}_m)^h$, recall (4.9). As the fully discrete energy, we consider

$$W^h(\vec{X}^m) = \pi \left(\vec{X}^m . \vec{e}_1, \left(\kappa^{m+1} - \overline{\varkappa} - \Re^m(\kappa^{m+1}) \right)^2 |\vec{X}_\rho^m| \right)^h . \tag{5.2}$$

On recalling (2.6), and given $\Gamma^0 = \vec{X}^0(\overline{I})$, we define the initial data $\kappa^0 \in V^h$ via $\kappa^0 = \pi^h \left[\frac{\vec{\kappa}^0 . \vec{\omega}^0}{|\vec{\omega}^0|} \right]$, where $\vec{\kappa}^0 \in \underline{V}^h$ is such that

$$\left(\vec{\kappa}^0, \vec{\eta} \, |\vec{X}_\rho^0| \right)^h + \left(\vec{X}_\rho^0, \vec{\eta}_\rho \, |\vec{X}_\rho^0|^{-1} \right) = 0 \qquad \forall \, \vec{\eta} \in \underline{V}^h .$$

Unless otherwise stated, we set $\overline{\varkappa} = 0$.

5.3.1. Sphere

We note that a sphere of radius $r(t)$, where $r(t)$ satisfies

$$r'(t) = -\frac{\overline{\varkappa}}{r(t)} \left(\frac{2}{r(t)} + \overline{\varkappa} \right), \quad r(0) = r_0 \in \mathbb{R}_{>0} , \tag{5.3}$$

is a solution to (1.7). The nonlinear ODE (5.3), in the case $\overline{\varkappa} \neq 0$, is solved by $r(t) = z(t) - \frac{2}{\overline{\varkappa}}$, where $z(t)$ is such that $\frac{1}{2}(z^2(t) - z_0^2) - \frac{4}{\overline{\varkappa}}(z(t) - z_0) + \frac{4}{\overline{\varkappa}^2} \ln \frac{z(t)}{z_0} + \overline{\varkappa}^2 \, t = 0$, with $z_0 = r_0 + \frac{2}{\overline{\varkappa}}$.

We use the true solution (5.3) for a convergence experiment for the scheme $(\mathcal{W}_m)^h$. Here we start with a nonuniform partitioning of a semicircle of radius $r(0) = r_0 = 1$ and compute the flow for $\overline{\varkappa} = -1$ until time $T = 1$. In particular, we have $\partial_0 I = \partial I = \{0, 1\}$ and we choose $\vec{X}^0 \in \underline{V}_{\partial_0}^h$ with

$$\vec{X}^0(q_j) = r_0 \begin{pmatrix} \cos[(q_j - \frac{1}{2})\pi + 0.1 \cos((q_j - \frac{1}{2})\pi)] \\ \sin[(q_j - \frac{1}{2})\pi + 0.1 \cos((q_j - \frac{1}{2})\pi)] \end{pmatrix}, \quad j = 0, \ldots, J,$$
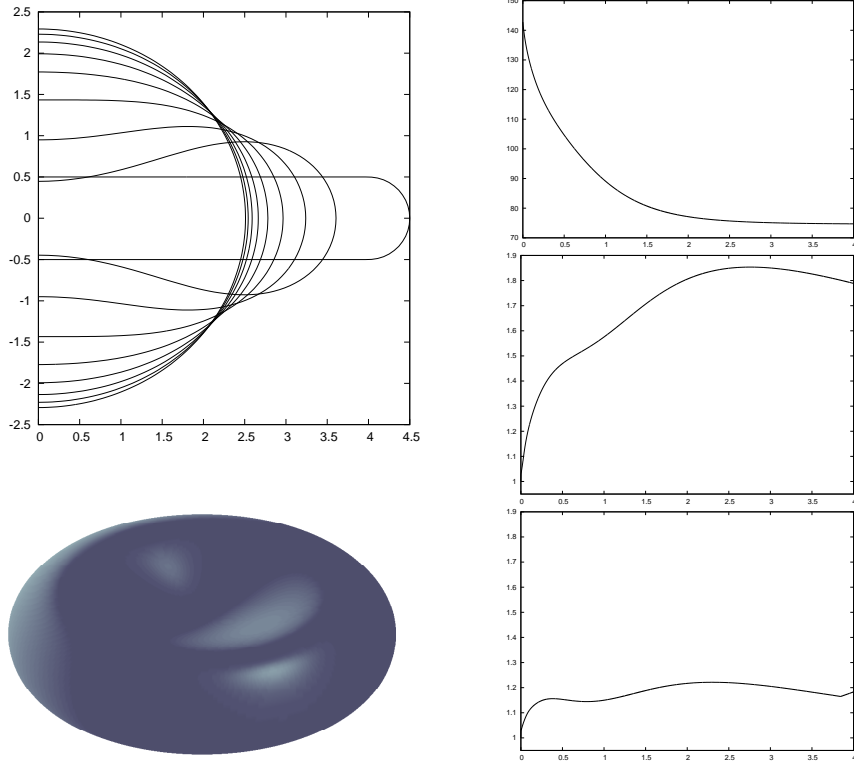
22

Figure 8: $(\mathcal{E}_m)^h$ Evolution for a disc of dimension $9 \times 1 \times 9$. Plots are at times $t = 0, 0.5, \ldots, 4$. We also visualize the axisymmetric surface $\mathcal{S}^m$ generated by Γ^m at time $t = 0.5$. On the right are plots of the discrete energy and the ratio $\mathfrak{r}^m$ and, as a comparison, a plot of the ratio $\mathfrak{r}^m$ for the scheme $(\mathcal{F}_{m,\star})$.
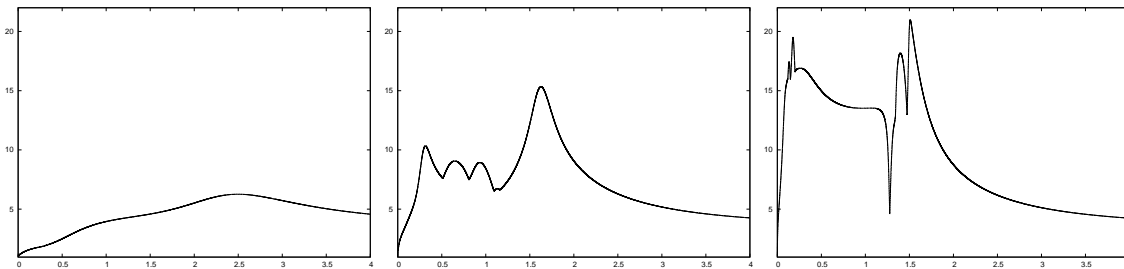
Figure 9: $(\mathcal{F}_{m,\star})$ Plot of the ratio $\mathfrak{r}^m$ for $\Delta t = \Delta t = 10^{-k}$, $k = 4, 5, 6$.

23
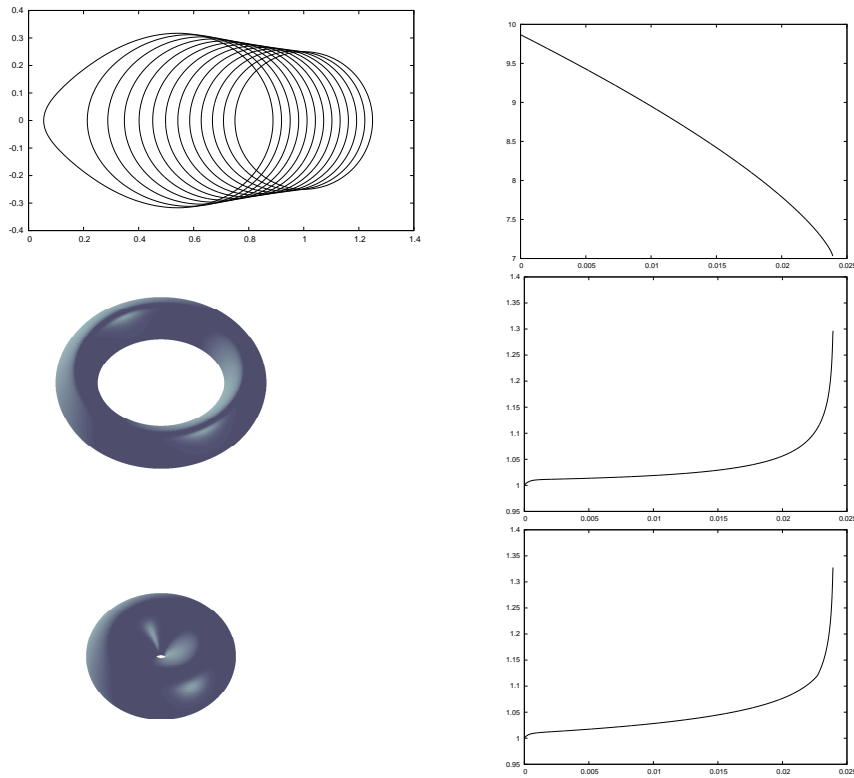
Figure 10: $(\mathcal{E}_m)^h$ Evolution for a torus with $R = 1$ and $r = 0.25$. Plots are at times $t = 0, 0.002, \ldots, 0.022, 0.02392$. We also visualize the axisymmetric surface $\mathcal{S}^m$ generated by Γ^m at times $t = 0$ (above) and $t = 0.02392$ (below). On the right are plots of the discrete energy and the ratio $\mathfrak{r}^m$ and, as a comparison, a plot of the ratio $\mathfrak{r}^m$ for the scheme $(\mathcal{F}_{m,\star})$.
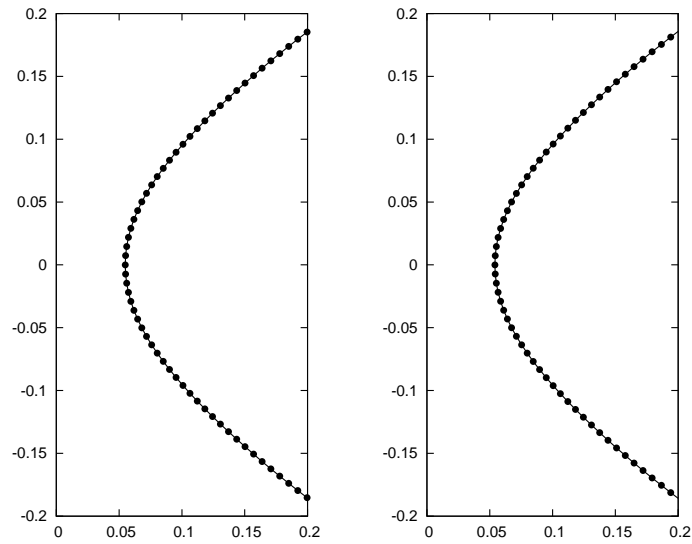
Figure 11: Detail of the vertex distribution at time $t = 0.02392$ for the experiment in Figure 10 for the schemes $(\mathcal{E}_m)^h$ (left) and $(\mathcal{F}_{m,\star})$ (right).
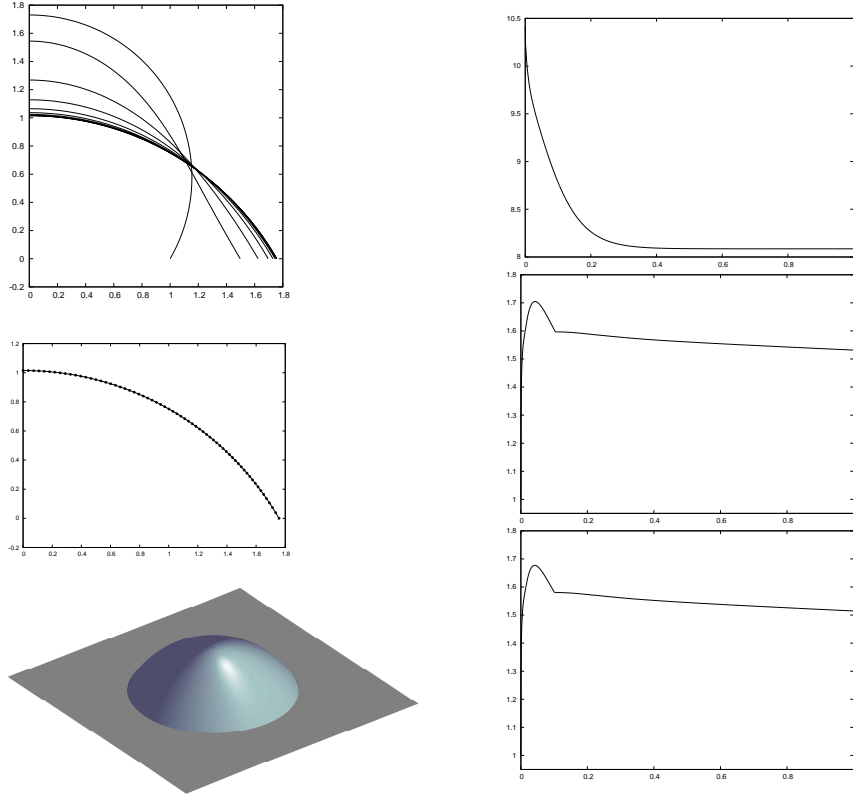
Figure 12: $(\mathcal{E}_m)^h$ $[\partial_0 I = \{1\}, \partial_2 I = \{0\}, \widehat{\varrho}^{(0)}_{\partial S} = -\frac{1}{2}]$ Evolution for a droplet attached to $\mathbb{R} \times \{0\} \times \mathbb{R}$. Solutions at times $t = 0, 0.1, \dots, 1$ and at time $t = 1$. We also visualize the axisymmetric surface $\mathcal{S}^m$ generated by Γ^m at time $t = 1$. On the right are plots of the discrete energy and the ratio (5.1) and, as a comparison, a plot of the ratio $\mathfrak{r}^m$ for the scheme $(\mathcal{F}_{m,\star})$.

recall (3.1). We compute the error $\|\Gamma - \Gamma^h\|_{L^\infty} = \max_{m=1,\dots,M} \max_{j=0,\dots,J} \|\vec{X}^m(q_j)| - r(t_m)|$ over the time interval $[0, T]$ between the true solution and the discrete solutions for the scheme $(\mathcal{W}_m)^h$. Here we use the time step size $\Delta t = 0.1\, h^2_{\Gamma^0}$, where h_{Γ^0} is the maximal edge length of Γ^0. The computed errors are reported in Table 3, where we observe a convergence rate of $O(h^2_{\Gamma^0})$.

5.3.2. Genus 0 surface

The evolution for Willmore flow for the same initial data as in Figure 8 is shown in Figure 19. The discretization parameters for the scheme $(\mathcal{W}_m)^h$ are $J = 128$ and $\Delta t = 10^{-3}$. As expected, the flat disc evolves to a sphere. At time $t = 10$ the discrete Willmore energy (5.2) is 25.330, and continuing the evolution until time $t = 100$ yields an energy of 25.131. This compares well with the value $8\pi = 25.133$, which is the Willmore energy (1.6), for $\overline{\varkappa} = 0$, of a sphere. Repeating the simulation with $\overline{\varkappa} = -2$ yields the results in Figure 20, where we observe that the final steady state now approximates the unit sphere. In fact, the discrete energy (5.2) at time $t = 3$ is 1.8×10^{-5}, which compares

Table 3: $(\mathcal{W}_m)^h$ Errors for the convergence test (5.3) with $\overline{\varkappa} = -1$.

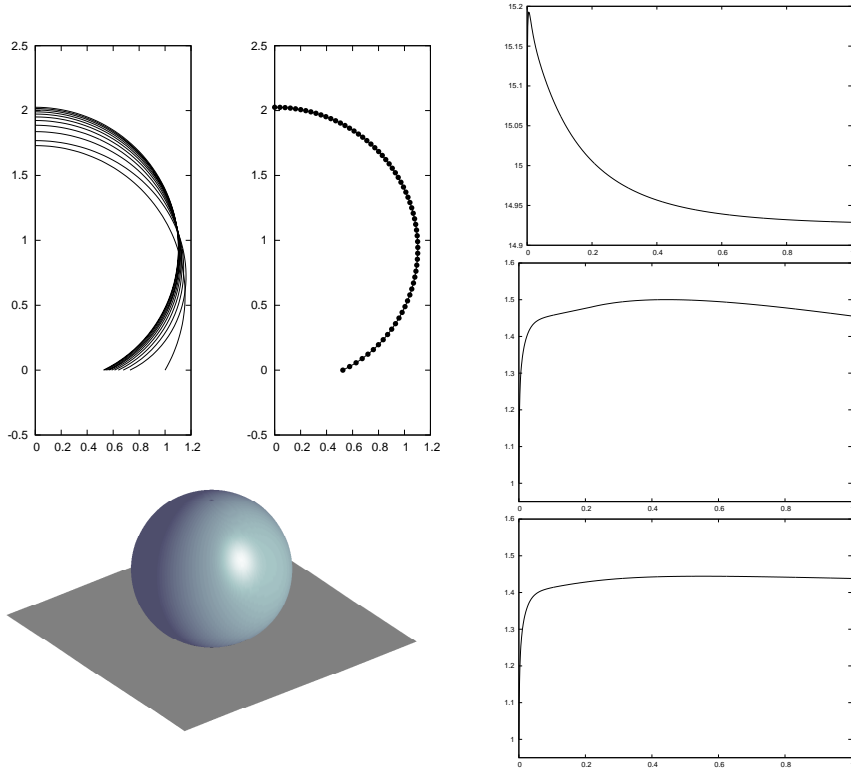| J	h_{Γ^0}	$\|\Gamma - \Gamma^h\|_{L^\infty}$	EOC
32	1.0792e-01	1.9659e-03	—
64	5.3988e-02	5.1262e-04	1.940681
128	2.6997e-02	1.2980e-04	1.981917
256	1.3499e-02	3.2571e-05	1.994737
512	6.7495e-03	8.1512e-06	1.998504

Figure 13: $(\mathcal{E}_m)^h$ $[\partial_0 I = \{1\}, \partial_2 I = \{0\}, \widehat{\varrho}_{\partial S}^{(0)} = 0.9]$ Evolution for a droplet attached to $\mathcal{B}$. Solutions at times $t = 0, 0.1, \ldots, 1$ and at time $t = 1$. We also visualize the axisymmetric surface $\mathcal{S}^m$ generated by Γ^m at time $t = 1$. On the right are plots of the discrete energy and the ratio (5.1) and, as a comparison, a plot of the ratio $\mathfrak{r}^m$ for the scheme $(\mathcal{F}_{m,\star})$.

with the energy (1.6), for $\overline{\varkappa} = -2$, being zero for a unit sphere. We also repeat the computation in [8, Fig. 9] for a rounded cylinder of total dimension $2 \times 6 \times 2$, see Figure 21. Here the surface would like to pinch off into two unit spheres. The discretization parameters are $J = 128$ and $\Delta t = 10^{-3}$. We note that at time $t = 1$, the ratio $\mathfrak{r}^m$ has reached a value of 1.14. Hence, despite the proximity to the x_2–axis, the vertices are still nearly equidistributed.

5.3.3. Genus 1 surface

Using as initial data for Willmore flow the surface generated by the curve $\Gamma(0)$ that is given by an elongated cigar-like shape of total dimension 4×1, with barycentre $(4, 0)^T \in \mathbb{R}^2$, we observe the numerical evolution shown in Figure 22. The discretization parameters are $J = 128$ and $\Delta t = 10^{-3}$. The observed final radius of Γ^m is 2.11, with the centre of the circle at $(3.06, 0)$. Hence the ratio of the two radii of the torus is $R/r = 3.06/2.11 = 1.4488$, which will tend to $\sqrt{2}$ as the evolution continues further. In fact, continuing the evolution until time $t = 10$ yields a ratio $R/r = 3.03/2.15 = 1.4140$ and a discrete energy (5.2) of 39.484. Here we recall that the ratio $\sqrt{2}$ characterizes the Clifford torus, the known minimizer of the Willmore energy (1.6), with $\overline{\varkappa} = 0$, among all genus 1 surfaces, see [37], with Willmore energy equal to $4\pi^2 = 39.478$. Repeating the simulation in Figure 22 with $\overline{\varkappa} = -2$ gives the results in Figure 23. The observed final radius of Γ^m is 0.498, with the centre of the circle at $(4.26, 0)$. Hence the ratio of the two radii of the torus is now $R/r = 4.06/0.498 = 8.15$.

In order to study the development of a singularity under Willmore flow, we consider the evolution from [38, Figs. 8, 9]. In particular, as initial data for the scheme $(\mathcal{W}_m)^h$ we choose a curve that is the union of a circle of radius 0.5, and two quarter circles of radius 2, see Figure 24. The discretization parameters are $J = 1024$ and $\Delta t = 4 \times 10^{-5}$. It can be seen from the numerical results shown in Figure 24 that the scheme $(\mathcal{W}_m)^h$ computes an evolution of a shape with a loop with large curvature and two circular segments that increase in size. We conjecture that as $t \to \infty$, upon rescaling to a shape of fixed diameter, the surface approaches two touching spheres. This would resemble a singularity for Willmore flow. We note that the existence of surfaces that become singular under Willmore flow was proven in
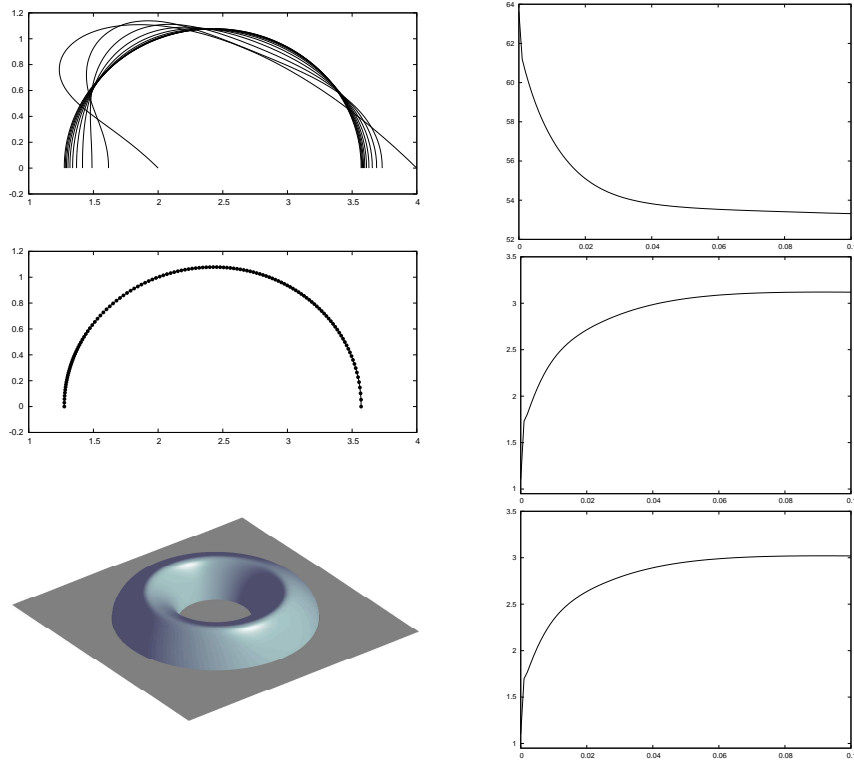
26

Figure 14: $(\mathcal{E}_m)^h$ $[\partial_2 I = \partial I = \{0,1\}, \widehat{\varrho}_{\partial\mathcal{S}}^{(0)} = \widehat{\varrho}_{\partial\mathcal{S}}^{(1)} = 0]$ Evolution for the upper half of a genus 1 surface attached to $\mathbb{R} \times \{0\} \times \mathbb{R}$. Solutions at times $t = 0, 0.01, \ldots, 0.1$ and at time $t = 0.1$. We also visualize the axisymmetric surface $\mathcal{S}^m$ generated by Γ^m at time $t = 0.1$. On the right are plots of the discrete energy and the ratio (5.1) and, as a comparison, a plot of the ratio $\mathfrak{r}^m$ for the scheme $(\mathcal{F}_{m,\star})$.

[15]. More precisely, it was shown that either a finite time singularity occurs, or that a rescaled infinite time solution becomes singular for large times. It is stated in [15, p. 408] that "either a small quantum of the curvature concentrates or the diameter of the surface does not stay bounded under the Willmore flow". Our simulations indicate that the latter can happen and in contrast to [38] we did not found any indication for a finite time singularity. Here we remark that the authors in [38, Fig. 8], who also exploit an additional symmetry and only compute the evolution for half the generating curve, appear to have performed a topological change to yield two touching spheres at a finite time. Given our numerical results we believe that this heuristical topological change was not justified, and the simulation should have been continued normally. Repeating the simulation in Figure 24 for $J = 2048$ and $\Delta t = 10^{-5}$ until time $t = 100$ yields very good agreement between the shapes of the curves for our two experiments, and so we are satisfied that the evolution shown in Figure 24 approximates Willmore flow of the initial data. We remark that the discrete energy (5.2) at time $t = 1000$ for the run in Figure 24 is 50.739, with the Willmore energy, (1.6) for $\overline{\varkappa} = 0$, for two touching spheres being equal to $16\pi = 50.265$. Finally, in order to better understand the long-time behaviour of the "radius" of the two approximate expanding spheres, we plot in Figure 25 the quantities $\max_{\overline{I}} \vec{X}^m \cdot \vec{e}_1$ and $\frac{1}{4}(\max_{\overline{I}} \vec{X}^m \cdot \vec{e}_2 - \min_{\overline{I}} \vec{X}^m \cdot \vec{e}_2)$ over time. We fit both curves to a function of the form $f(t) = a t^p$. For the former curve, we obtain a value $p = 0.222$, while for the second curve we obtain the power $p = 0.232$.

5.4. Numerical results for Helfrich flow

Here we present some simulations for the scheme $(\mathcal{W}_m^{A,V})^h$, recall (4.10).

5.4.1. Genus 0 surface

We repeat the computation in [8, Fig. 6] for Helfrich flow with $\overline{\varkappa} = 0$ of a rounded cylinder of total dimension $1 \times 4 \times 1$. The discretization parameters are $J = 128$ and $\Delta t = 10^{-3}$. We observe relative surface area and volume losses of 0.00%, and we obtain the evolution in Figure 26 towards a mild dumbbell-like shape.
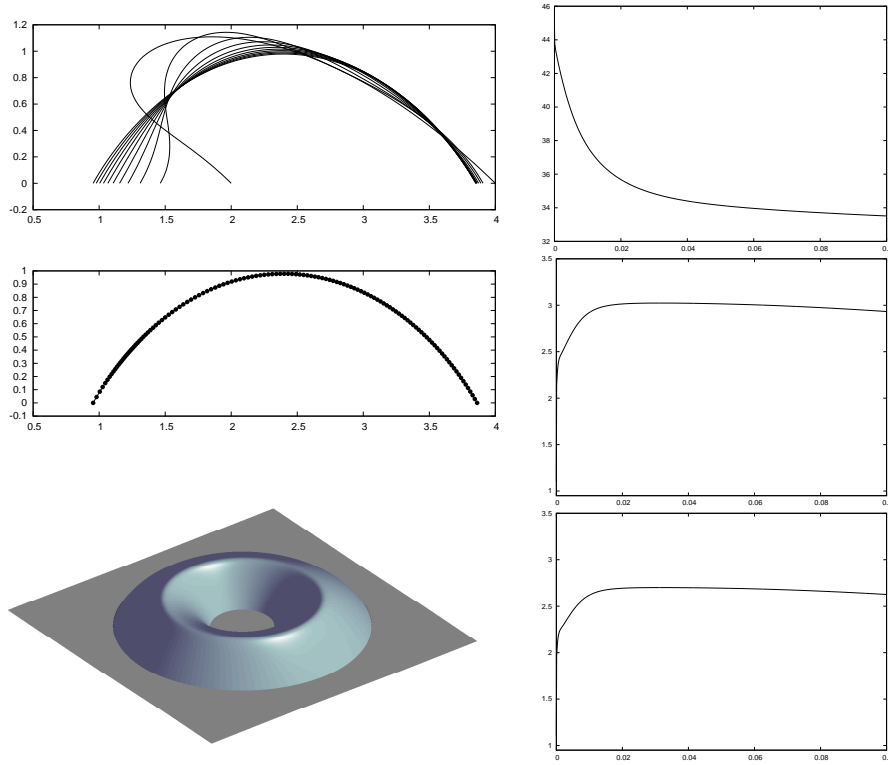
27

Figure 15: $(\mathcal{E}_m)^h$ $[\partial_2 I = \partial I = \{0, 1\}, \widehat{\varrho}_{\partial S}^{(0)} = -\widehat{\varrho}_{\partial S}^{(1)} = \frac{1}{2}]$ Evolution for the upper half of a genus 1 surface attached to $\mathbb{R} \times \{0\} \times \mathbb{R}$. Solutions at times $t = 0, 0.01, \ldots, 0.1$ and at time $t = 0.1$. We also visualize the axisymmetric surface $\mathcal{S}^m$ generated by Γ^m at time $t = 0.1$. On the right are plots of the discrete energy and the ratio (5.1) and, as a comparison, a plot of the ratio $\mathfrak{r}^m$ for the scheme $(\mathcal{F}_{m,\star})$.

5.4.2. Genus 1 surface

Repeating the experiment in Figure 22 for Helfrich flow, until the earlier time of $T = 0.5$, we observe a relative surface area loss of 0.12% and a relative volume loss of 0.00%. The evolution is shown in Figure 27, where we note that the evolution is very different from the one in Figure 22. In particular, the toroidal surface would like to undergo a change of topology, and close the hole at the origin to become a genus 0 surface. For the smaller time steps $\Delta t = 10^{-4}$ and $\Delta t = 10^{-5}$, the relative surface area loss is reduced to 0.01% and 0.00%, respectively, while the relative volume losses remain zero to the displayed number of digits.

Conclusions

We have derived and analysed various numerical schemes for the parametric approximation of surface diffusion, an intermediate flow between surface diffusion and conserved mean curvature flow, Willmore flow and Helfrich flow.

As regards surface diffusion, we propose a choice between two practical and robust schemes. A very practical linear scheme is given by $(\mathcal{E}_m)^h$. In practice the scheme is stable, and it asymptotically distributes the vertices uniformly. A nonlinear scheme, for which an unconditional stability bound can be shown, is given by $(\mathcal{F}_{m,\star})$. The nonlinearity in $(\mathcal{F}_{m,\star})$ is only very mild, and so a Newton solver never takes more than three iterations in practice. Moreover, coalescence of vertices does not occur in practice, and the ratio of largest element/smallest element appears to asymptotically approach some value that is significantly larger than 1, but smaller than 10. Similarly to $(\mathcal{F}_{m,\star})$, we presented the scheme $(\mathcal{I}_{m,\star})$ for the approximation of the intermediate flow. Once again, the scheme is unconditionally stable and can be easily solved for with a Newton method

Lastly, for Willmore flow and Helfrich flow we propose the fully practical linear schemes $(\mathcal{W}_m)^h$ and $(\mathcal{W}_m^{A,V})^h$, respectively. Like the scheme $(\mathcal{E}_m)^h$, they also enjoy an asymptotic equidistribution property.
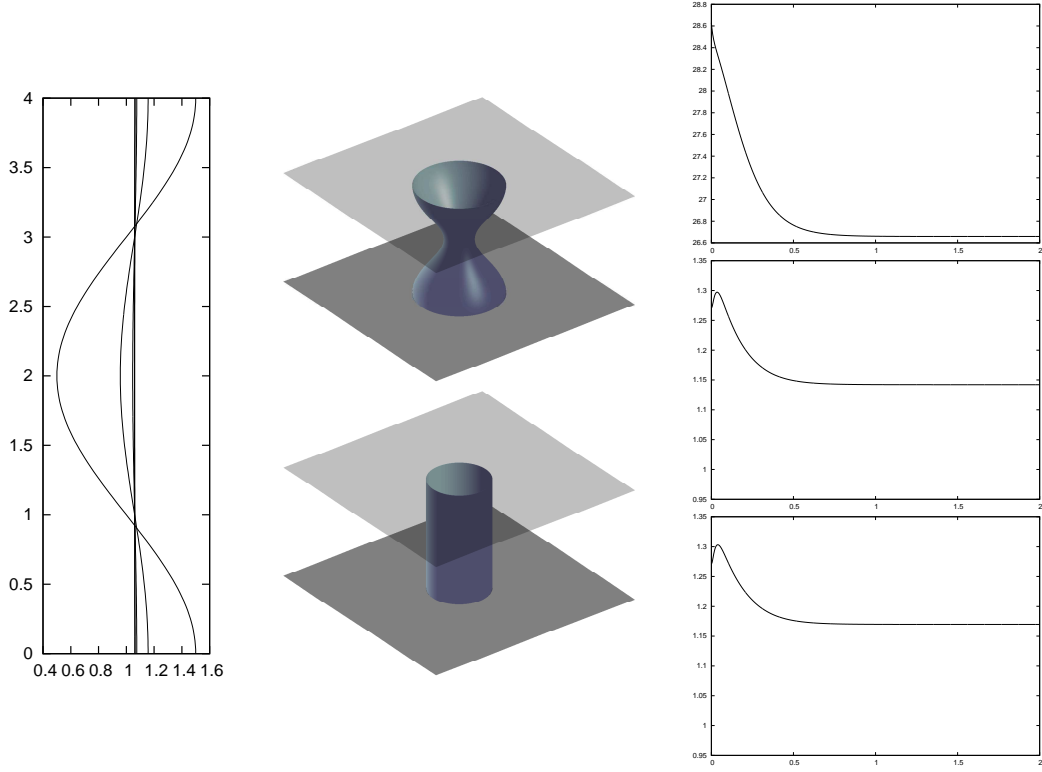
28

Figure 16: $(\mathcal{E}_m)^h$ $[\partial_2 I = \partial I = \{0, 1\}, \widehat{\varrho}_{\partial\mathcal{S}}^{(0)} = \widehat{\varrho}_{\partial\mathcal{S}}^{(1)} = 0]$ Evolution for an open dumbbell-like cylindrical shape attached to $\mathbb{R} \times \{0\} \times \mathbb{R}$ and $\mathbb{R} \times \{4\} \times \mathbb{R}$. Solution at times $t = 0, 0.5, \ldots, 2$. We also visualize the axisymmetric surface $\mathcal{S}^m$ generated by Γ^m at times $t = 0$ (above) and $t = 2$ (below). On the right are plots of the discrete energy and the ratio (5.1) and, as a comparison, a plot of the ratio r^m for the scheme $(\mathcal{F}_{m,\star})$.

Appendix A. Derivation of (2.20) on $\partial_0 I$

Here we demonstrate that (2.21a) and (2.24a) weakly impose (2.20) on $\partial_0 I$. These proofs are an extension of the proof in [12, Appendix A], where it is shown that (2.24b) weakly imposes (2.16). First we consider (2.24a) and the case $\rho_0 = 0 \in \partial_0 I$.

We assume for almost all $t \in (0, T)$ that $\vec{x}(t) \in [C^1(\overline{I})]^2$, $\varkappa_S(t) \in C^1(\overline{I})$ and $\vec{x}_t(t) . \vec{\nu}(t) \in L^\infty(I)$. These assumptions and (2.3) imply that

$$C_1 \rho \le |\vec{x}(\rho, t) . \vec{e}_1| \le C_2 \rho \qquad \forall \, \rho \in [0, \overline{\rho}], \tag{A.1}$$

for $\overline{\rho}$ sufficiently small, and for almost all $t \in (0, T)$.

Let $t \in (0, T)$. For a fixed $\overline{\rho} > 0$ and $\varepsilon \in (0, \overline{\rho})$, we define

$$\chi_\varepsilon(\rho) = \begin{cases} (\overline{\rho})^{-1} \int_\varepsilon^{\overline{\rho}} (\vec{x}(z, t) . \vec{e}_1)^{-1} \, \mathrm{d}z & 0 \le \rho < \varepsilon, \\ (\overline{\rho})^{-1} \int_\rho^{\overline{\rho}} (\vec{x}(z, t) . \vec{e}_1)^{-1} \, \mathrm{d}z & \varepsilon \le \rho < \overline{\rho}, \\ 0 & \overline{\rho} \le \rho. \end{cases}$$

We observe that (A.1) implies that $(\vec{x} . \vec{e}_1) \chi_\varepsilon$ is integrable in the limit $\varepsilon \to 0$. On choosing $\chi = \chi_\varepsilon \in H^1(I)$ in (2.24a), we obtain in the limit $\varepsilon \to 0$ that

$$(\overline{\rho})^{-1} \int_0^{\overline{\rho}} (\vec{x} . \vec{e}_1) \, \vec{x}_t . \vec{\nu} \left(\int_\rho^{\overline{\rho}} (\vec{x} . \vec{e}_1)^{-1} \, \mathrm{d}z \right) |\vec{x}_\rho| \, \mathrm{d}\rho = -(\overline{\rho})^{-1} \int_0^{\overline{\rho}} (\varkappa_S)_\rho \, |\vec{x}_\rho|^{-1} \, \mathrm{d}\rho. \tag{A.2}$$
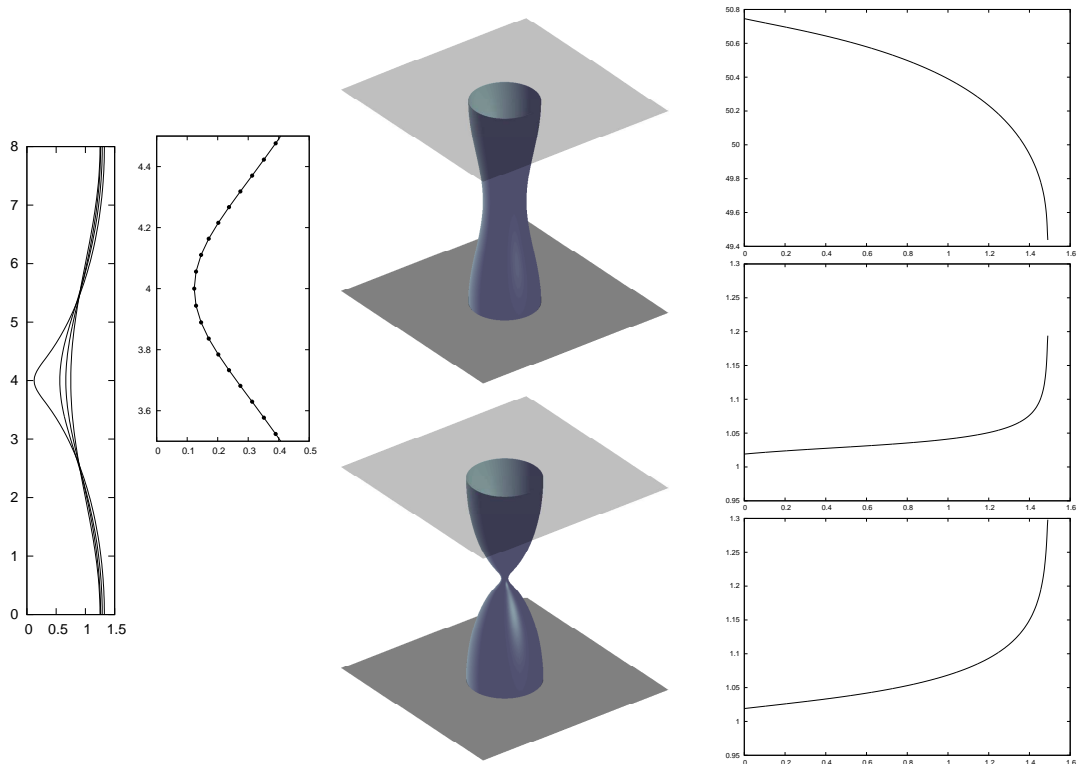
29

Figure 17: $(\mathcal{E}_m)^h$ $[\partial_2 I = \partial I = \{0, 1\}, \widehat{\varrho}_{\partial S}^{(0)} = \widehat{\varrho}_{\partial S}^{(1)} = 0]$ Evolution for an open dumbbell-like cylindrical shape attached to $\mathbb{R} \times \{0\} \times \mathbb{R}$ and $\mathbb{R} \times \{8\} \times \mathbb{R}$. Solution at times $t = 0, 0.5, 1, 1.49$, and a detail of the vertex distribution at time $t = 1.49$. We also visualize the axisymmetric surface $\mathcal{S}^m$ generated by Γ^m at times $t = 0$ (above) and $t = 1.49$ (below). On the right are plots of the discrete energy and the ratio (5.1) and, as a comparison, a plot of the ratio $\mathfrak{r}^m$ for the scheme $(\mathcal{F}_{m,\star})$.
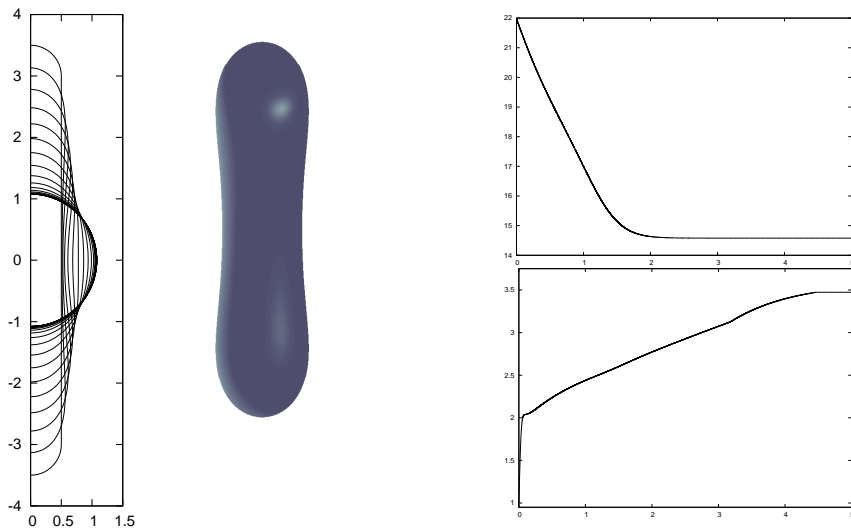
Figure 18: $(\mathcal{I}_{m,\star})$ Evolution for a rounded cylinder of dimension $1 \times 7 \times 1$. Plots are at times $t = 0, 0.2, \ldots, 5$. We also visualize the axisymmetric surface $\mathcal{S}^m$ generated by Γ^m at time $t = 0.4$. On the right are plots of the discrete energy and the ratio $\mathfrak{r}^m$.

30

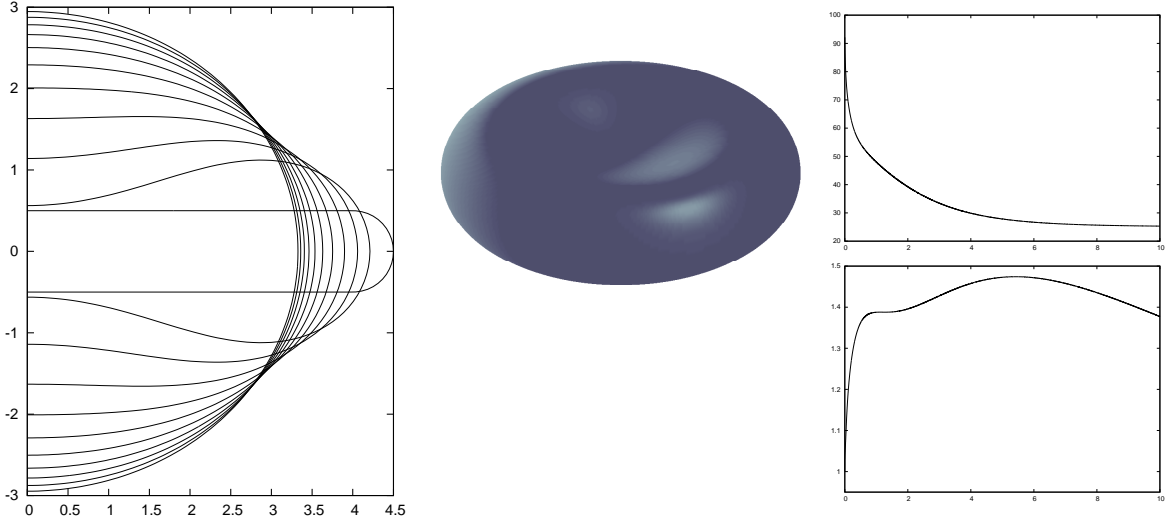Figure 19: $(\mathcal{W}_m)^h$ Willmore flow for a disc of dimension $9 \times 1 \times 9$. Solution at times $t = 0, 1, \ldots, 10$. We also visualize the axisymmetric surface $\mathcal{S}^m$ generated by Γ^m at time $t = 1$. On the right a plot of the discrete energy and of the ratio (5.1).
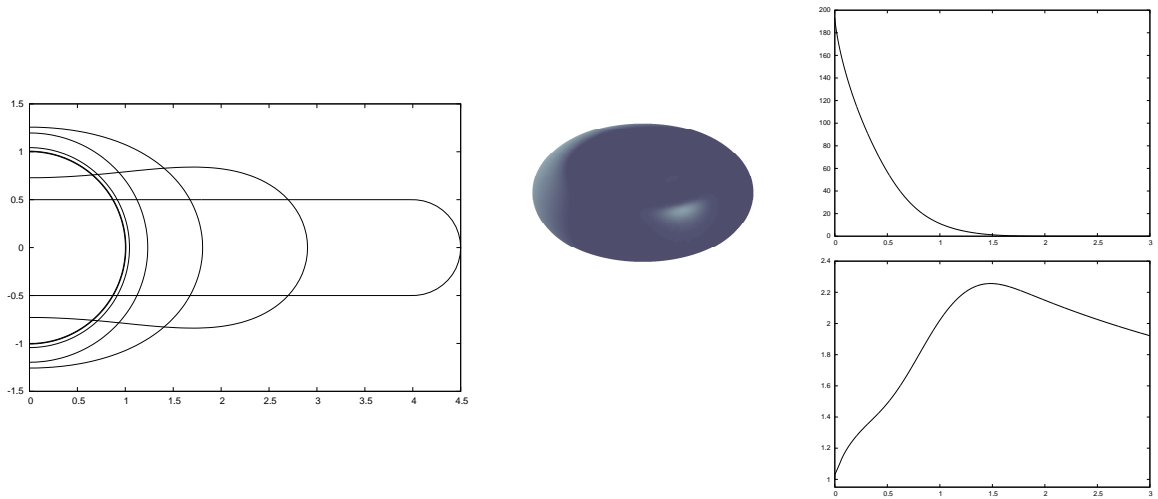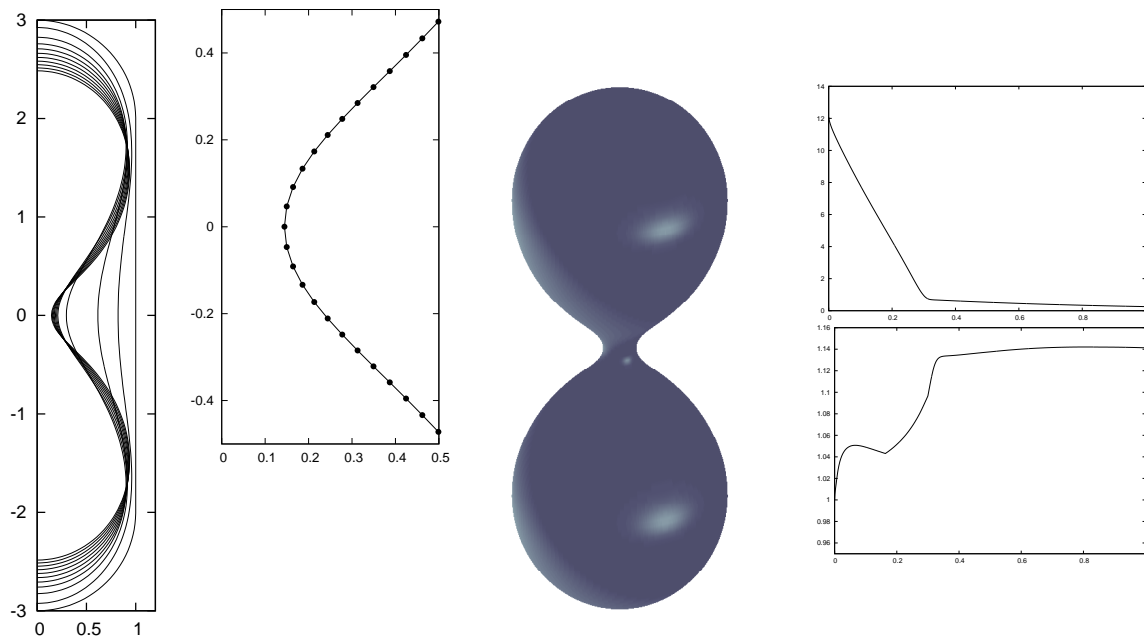

Figure 20: $(\mathcal{W}_m)^h$ Willmore flow with $\overline{\varkappa} = -2$ for a disc of dimension $9 \times 1 \times 9$. Solution at times $t = 0, 0.5, \ldots, 3$. We also visualize the axisymmetric surface $\mathcal{S}^m$ generated by Γ^m at time $t = 0.5$. On the right a plot of the discrete energy and of the ratio (5.1).

31

Figure 21: $(\mathcal{W}_m)^h$ Willmore flow with $\overline{\varkappa} = -2$ for a rounded cylinder of dimension $2 \times 6 \times 2$. Solution at times $t = 0, 0.1, \ldots, 1$, and a detail of the vertex distribution at time $t = 1$. We also visualize the axisymmetric surface $\mathcal{S}^m$ generated by Γ^m at time $t = 1$. On the right are plots of the discrete energy and of the ratio (5.1).
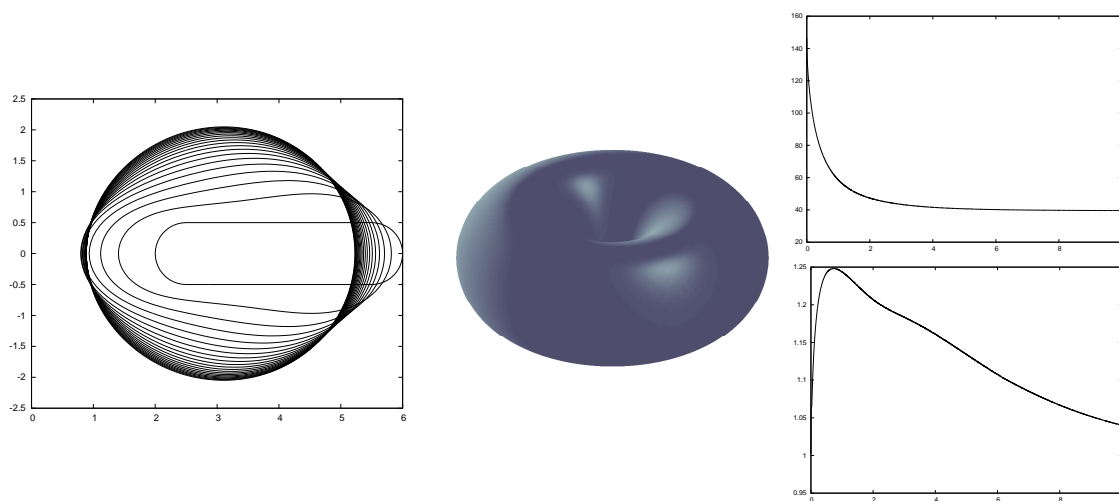
Figure 22: $(\mathcal{W}_m)^h$ Willmore flow towards a Clifford torus. Solution at times $t = 0, 0.5, \ldots, 10$. We also visualize the axisymmetric surface $\mathcal{S}^m$ generated by Γ^m at time $t = 10$. On the right a plot of the discrete energy and of the ratio (5.1).
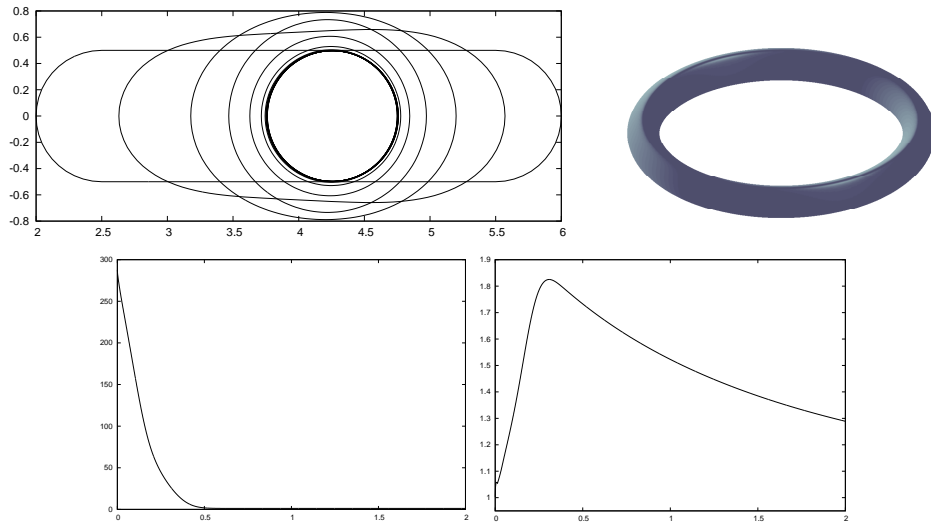
Figure 23: $(\mathcal{W}_m)^h$ Willmore flow with $\overline{\varkappa} = -2$ towards a torus. Solution at times $t = 0, 0.1, \ldots, 2$. We also visualize the axisymmetric surface $\mathcal{S}^m$ generated by Γ^m at time $t = 2$. Below a plot of the discrete energy and of the ratio (5.1).

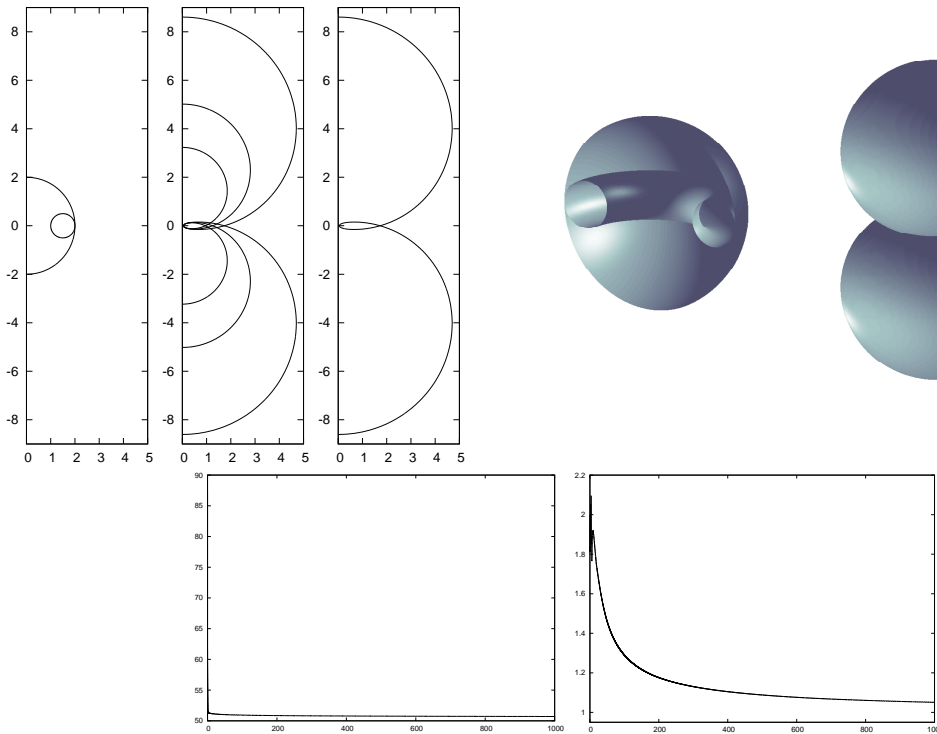Figure 24: $(\mathcal{W}_m)^h$ Willmore flow towards two touching spheres. In the first three plots we show the initial data, the solution at times $t = 10, 100, 1000$, and again at time $t = 1000$. We also visualize parts of the axisymmetric surface $\mathcal{S}^m$ generated by Γ^m at time $t = 0$ and at time $t = 10$. Below a plot of the discrete energy and of the ratio (5.1).
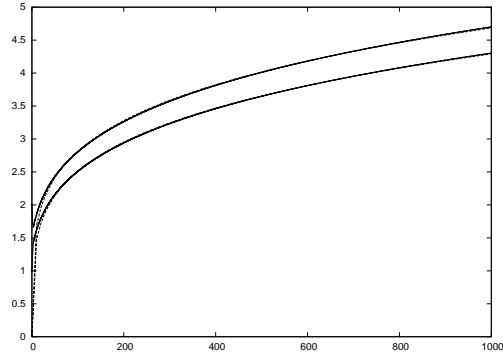
33

Figure 25: A plot of $\max_{\mathcal{I}} \vec{X}^m \cdot \vec{e}_1$ (upper graph) and $\frac{1}{4} (\max_{\mathcal{I}} \vec{X}^m \cdot \vec{e}_2 - \min_{\mathcal{I}} \vec{X}^m \cdot \vec{e}_2)$ (lower graph) over time, for the simulation in Figure 24, together with the functions $f_i(t) = a_i t^{p_i}$, $i = 1, 2$, with $(a_1, p_1) = (1.013, 0.222)$ and $(a_2, p_2) = (0.863, 0.232)$.
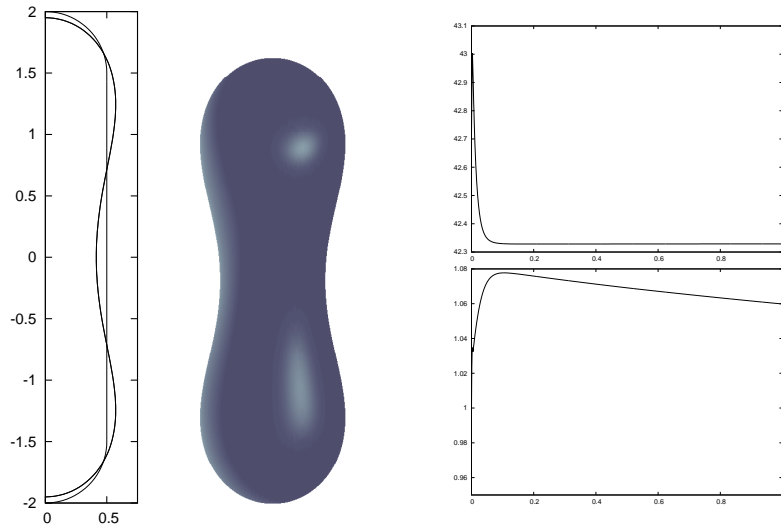

Figure 26: $(\mathcal{W}_m^{A,V})^h$ Helfrich flow for $\overline{\varkappa} = 0$ for a rounded cylinder of dimension $1 \times 4 \times 1$. Solution at times $t = 0, 0.5, 1$. We also visualize the axisymmetric surface $\mathcal{S}^m$ generated by Γ^m at time $t = 1$. On the right are plots of the discrete energy and of the ratio (5.1).

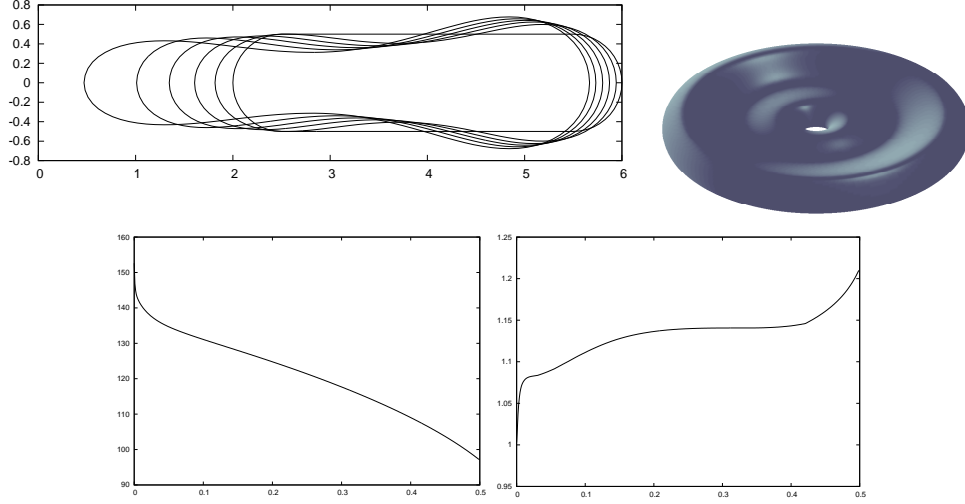Figure 27: $(\mathcal{W}_m^{A,V})^h$ Helfrich flow for a toroidal surface. Solution at times $t = 0, 0.1, \ldots, 0.5$. We also visualize the axisymmetric surface $\mathcal{S}^m$ generated by Γ^m at time $t = 0.5$. Below a plot of the discrete energy and of the ratio (5.1).

Applying Fubini's theorem and noting (A.1), as well as the boundedness of $|\vec{x}_\rho|$ and $\vec{x}_t \cdot \vec{v}$, yields that

$$\left| (\overline{\rho})^{-1} \int_0^{\overline{\rho}} (\vec{x} \cdot \vec{e}_1) \, \vec{x}_t \cdot \vec{v} \left(\int_\rho^{\overline{\rho}} (\vec{x} \cdot \vec{e}_1)^{-1} \, \mathrm{d}z \right) |\vec{x}_\rho| \, \mathrm{d}\rho \right| = \left| (\overline{\rho})^{-1} \int_0^{\overline{\rho}} (\vec{x} \cdot \vec{e}_1)^{-1} \left(\int_0^z (\vec{x} \cdot \vec{e}_1) \, \vec{x}_t \cdot \vec{v} \, |\vec{x}_\rho| \, \mathrm{d}\rho \right) \mathrm{d}z \right| \to 0 \quad \text{as } \overline{\rho} \to 0 \,. \tag{A.3}$$

On the other hand, the right hand side in (A.2) converges to $(\varkappa_\mathcal{S})_\rho(0,t) \, |\vec{x}_\rho(0,t)|^{-1}$ as $\overline{\rho} \to 0$, on recalling the smoothness assumptions on $\varkappa_\mathcal{S}$ and $\vec{x}$. Combining this with (A.3) and (2.3) yields the boundary condition (2.20) for $\rho = 0 \in \partial_0 I$. The proof for $\rho = 1 \in \partial_0 I$ is analogous.

The proof for (2.21a) is identical, on assuming that $(\varkappa - \frac{\vec{v} \cdot \vec{e}_1}{\vec{x} \cdot \vec{e}_1})(t) \in C^1(\overline{I})$ for almost all $t \in (0, T)$. Finally we note that the above proof also shows that (2.28a) weakly imposes (2.27) on $\partial_0 I$, on assuming that $y(t) \in C^1(\overline{I})$ for almost all $t \in (0, T)$.

Appendix B. Some axisymmetric differential geometry

Let $\vec{x} : \overline{I} \to \mathbb{R}^2$ parameterize Γ, the generating curve of a surface $\mathcal{S}$. Then $\vec{y} : \overline{I} \times [0, 2\pi) \to \mathbb{R}^3$ parameterizes $\mathcal{S}$, where

$$\vec{y}(\rho, \theta) = (\vec{x}(\rho) \cdot \vec{e}_1 \, \cos\theta, \, \vec{x}(\rho) \cdot \vec{e}_2, \, \vec{x}(\rho) \cdot \vec{e}_1 \, \sin\theta)^T \,. \tag{B.1}$$

On recalling that $\partial_s = |\vec{x}_\rho|^{-1} \, \partial_\rho$, we note that

$$|\vec{y}_s|^2 = 1 \,, \quad |\vec{y}_\theta|^2 = (\vec{x} \cdot \vec{e}_1)^2 \,, \quad \vec{y}_s \cdot \vec{y}_\theta = 0 \,. \tag{B.2}$$

In what follows, we often identify a function f defined on $\overline{I} \times [0, 2\pi)$ with the function $f \circ \vec{y}^{-1}$, defined on $\mathcal{S}$. For example, it follows from (B.2) that

$$\nabla_\mathcal{S} f = f_s \, \vec{y}_s + (\vec{x} \cdot \vec{e}_1)^{-2} \, f_\theta \, \vec{y}_\theta \,.$$

Similarly,

$$\nabla_\mathcal{S} \cdot \vec{f} = \vec{f}_s \cdot \vec{y}_s + (\vec{x} \cdot \vec{e}_1)^{-2} \, \vec{f}_\theta \cdot \vec{y}_\theta \,,$$

and so, on noting $((\vec{x} \cdot \vec{e}_1)^{-1} \vec{y}_\theta)_s = \vec{0}$ and $(\vec{y}_s)_\theta \cdot \vec{y}_\theta = (\vec{x} \cdot \vec{e}_1) \, \vec{x}_s \cdot \vec{e}_1$, we obtain that

$$\Delta_\mathcal{S} f = \nabla_\mathcal{S} \cdot (\nabla_\mathcal{S} f) = f_{ss} + \frac{\vec{x}_s \cdot \vec{e}_1}{\vec{x} \cdot \vec{e}_1} \, f_s + (\vec{x} \cdot \vec{e}_1)^{-2} \, f_{\theta\theta} \,.$$

35

For a radially symmetric function f, with $f(\rho, \theta) = f(\rho, 0)$ for all $(\rho, \theta) \in \overline{I} \times [0, 2\pi)$, it follows that

$$\Delta_{\mathcal{S}} f = (\vec{x} . \vec{e}_1)^{-1} (\vec{x} . \vec{e}_1 f_s)_s . \tag{B.3}$$

We remark that a derivation of (2.13), recall also (1.2), is obtained by combining (B.1) and (B.3) to yield, on recalling (2.6), (2.4) and (2.5), that

$$
\begin{aligned}
\Delta_{\mathcal{S}} \vec{y} = \vec{y}_{ss} + \frac{\vec{x}_s . \vec{e}_1}{\vec{x} . \vec{e}_1} \vec{y}_s + (\vec{x} . \vec{e}_1)^{-2} \vec{y}_{\theta\theta} &= \begin{pmatrix} \vec{x}_{ss} . \vec{e}_1 \cos\theta \\ \vec{x}_{ss} . \vec{e}_2 \\ \vec{x}_{ss} . \vec{e}_1 \sin\theta \end{pmatrix} + (\vec{x} . \vec{e}_1)^{-1} \begin{pmatrix} (\vec{x}_s . \vec{e}_1)^2 \cos\theta \\ (\vec{x}_s . \vec{e}_1) \, \vec{x}_s . \vec{e}_2 \\ (\vec{x}_s . \vec{e}_1)^2 \sin\theta \end{pmatrix} - (\vec{x} . \vec{e}_1)^{-1} \begin{pmatrix} \cos\theta \\ 0 \\ \sin\theta \end{pmatrix} \\
&= \varkappa \begin{pmatrix} \vec{\nu} . \vec{e}_1 \cos\theta \\ \vec{\nu} . \vec{e}_2 \\ \vec{\nu} . \vec{e}_1 \sin\theta \end{pmatrix} - (\vec{x} . \vec{e}_1)^{-1} \begin{pmatrix} (\vec{x}_s . \vec{e}_2)^2 \cos\theta \\ -(\vec{x}_s . \vec{e}_1) \, \vec{x}_s . \vec{e}_2 \\ (\vec{x}_s . \vec{e}_2)^2 \sin\theta \end{pmatrix} = \varkappa \begin{pmatrix} (\vec{\nu} . \vec{e}_1) \cos\theta \\ \vec{\nu} . \vec{e}_2 \\ (\vec{\nu} . \vec{e}_1) \sin\theta \end{pmatrix} - \frac{\vec{x}_s . \vec{e}_2}{\vec{x} . \vec{e}_1} \begin{pmatrix} \vec{x}_s . \vec{e}_2 \cos\theta \\ -\vec{x}_s . \vec{e}_1 \\ \vec{x}_s . \vec{e}_2 \sin\theta \end{pmatrix} \\
&= \left(\varkappa - \frac{\vec{\nu} . \vec{e}_1}{\vec{x} . \vec{e}_1} \right) \begin{pmatrix} \vec{\nu} . \vec{e}_1 \cos\theta \\ \vec{\nu} . \vec{e}_2 \\ \vec{\nu} . \vec{e}_1 \sin\theta \end{pmatrix} = \left(\varkappa - \frac{\vec{\nu} . \vec{e}_1}{\vec{x} . \vec{e}_1} \right) \vec{\nu}_{\mathcal{S}} .
\end{aligned}
\tag{B.4}
$$

Acknowledgements

References

[1] E. Bänsch, P. Morin, R.H. Nochetto, A finite element method for surface diffusion: the parametric case, J. Comput. Phys. 203 (2005) 321–343.

[2] J.W. Barrett, H. Garcke, R. Nürnberg, A parametric finite element method for fourth order geometric evolution equations, J. Comput. Phys. 222 (2007) 441–462.

[3] J.W. Barrett, H. Garcke, R. Nürnberg, On the variational approximation of combined second and fourth order geometric evolution equations, SIAM J. Sci. Comput. 29 (2007) 1006–1041.

[4] J.W. Barrett, H. Garcke, R. Nürnberg, On the parametric finite element approximation of evolving hypersurfaces in $\mathbb{R}^3$, J. Comput. Phys. 227 (2008) 4281–4307.

[5] J.W. Barrett, H. Garcke, R. Nürnberg, Parametric approximation of Willmore flow and related geometric evolution equations, SIAM J. Sci. Comput. 31 (2008) 225–253.

[6] J.W. Barrett, H. Garcke, R. Nürnberg, Finite element approximation of coupled surface and grain boundary motion with applications to thermal grooving and sintering, European J. Appl. Math. 21 (2010) 519–556.

[7] J.W. Barrett, H. Garcke, R. Nürnberg, Parametric approximation of surface clusters driven by isotropic and anisotropic surface energies, Interfaces Free Bound. 12 (2010) 187–234.

[8] J.W. Barrett, H. Garcke, R. Nürnberg, Computational parametric Willmore flow with spontaneous curvature and area difference elasticity effects, SIAM J. Numer. Anal. 54 (2016) 1732–1762.

[9] J.W. Barrett, H. Garcke, R. Nürnberg, A stable numerical method for the dynamics of fluidic biomembranes, Numer. Math. 134 (2016) 783–822.

[10] J.W. Barrett, H. Garcke, R. Nürnberg, Stable variational approximations of boundary value problems for Willmore flow with Gaussian curvature, IMA J. Numer. Anal. 37 (2017) 1657–1709.

[11] J.W. Barrett, H. Garcke, R. Nürnberg, Stable approximations for axisymmetric Willmore flow for closed and open surfaces, 2018. (in preparation).

[12] J.W. Barrett, H. Garcke, R. Nürnberg, Variational discretization of axisymmetric curvature flows, 2018. http://arxiv.org/abs/1805.04322.

[13] P. Basa, J.C. Schön, P. Salamon, The use of Delaunay curves for the wetting of axisymmetric bodies, Quart. Appl. Math. 52 (1994) 1–22.

[14] A.J. Bernoff, A.L. Bertozzi, T.P. Witelski, Axisymmetric surface diffusion: dynamics and stability of self-similar pinchoff, J. Statist. Phys. 93 (1998) 725–776.

[15] S. Blatt, A singular example for the Willmore flow, Analysis 29 (2009) 407–430.

[16] J.W. Cahn, J.E. Taylor, Surface motion by surface diffusion, Acta Metall. Mater. 42 (1994) 1045–1063.

[17] P.B. Canham, The minimum energy of bending as a possible explanation of the biconcave shape of the human red blood cell, J. Theor. Biol. 26 (1970) 61–81.

[18] B.D. Coleman, R.S. Falk, M. Moakher, Stability of cylindrical bodies in the theory of surface diffusion, Phys. D 89 (1995) 123–135.

[19] B.D. Coleman, R.S. Falk, M. Moakher, Space-time finite element methods for surface diffusion with applications to the theory of the stability of cylinders, SIAM J. Sci. Comput. 17 (1996) 1434–1448.

[20] G. Cox, J. Lowengrub, The effect of spontaneous curvature on a two-phase vesicle, Nonlinearity 28 (2015) 773–793.

[21] A. Dall'Acqua, A. Spener, The elastic flow of curves in the hyperbolic plane, 2017. http://arxiv.org/abs/1710.09600.

[22] A. Dall'Acqua, A. Spener, Circular solutions to the elastic flow in hyperbolic space, in: Proceedings of Analysis on Shapes of Solutions to Partial Differential Equations, (2017), volume 2082 of *RIMS Kôkyûroku*, Kyoto, Japan.

[23] K. Deckelnick, G. Dziuk, C.M. Elliott, Error analysis of a semidiscrete numerical scheme for diffusion in axially symmetric surfaces, SIAM J. Numer. Anal. 41 (2003) 2161–2179.

[24] K. Deckelnick, G. Dziuk, C.M. Elliott, Computation of geometric partial differential equations and mean curvature flow, Acta Numer. 14 (2005) 139–232.

[25] K. Deckelnick, F. Schieweck, Error analysis for the approximation of axisymmetric Willmore flow by C^1-finite elements, Interfaces Free Bound. 12 (2010) 551–574.

[26] G. Dziuk, Finite elements for the Beltrami operator on arbitrary surfaces, in: S. Hildebrandt, R. Leis (Eds.), Partial Differential Equations and Calculus of Variations, volume 1357 of *Lecture Notes in Math.*, Springer-Verlag, Berlin, 1988, pp. 142–155.

[27] G. Dziuk, An algorithm for evolutionary surfaces, Numer. Math. 58 (1991) 603–611.

[28] G. Dziuk, B. Kawohl, On rotationally symmetric mean curvature flow, J. Differential Equations 93 (1991) 142–149.

[29] C.M. Elliott, H. Garcke, Existence results for diffusive surface motion laws, Adv. Math. Sci. Appl. 7 (1997) 465–488.

[30] C.M. Elliott, B. Stinner, Modeling and computation of two phase geometric biomembranes using surface finite elements, J. Comput. Phys. 229 (2010) 6585–6612.

[31] R. Finn, Equilibrium Capillary Surfaces, Grundlehren der Mathematischen Wissenschaften 284, Springer-Verlag, New York, 1986.

[32] M.E. Gurtin, M.E. Jabbour, Interface evolution in three dimensions with curvature-dependent energy and surface diffusion: interface-controlled evolution, phase transitions, epitaxial growth of elastic films, Arch. Ration. Mech. Anal. 163 (2002) 171–208.

[33] W. Helfrich, Elastic properties of lipid bilayers: Theory and possible experiments, Z. Naturforsch. 28c (1973) 693–703.

[34] G. Huisken, Asymptotic behavior for singularities of the mean curvature flow, J. Differential Geom. 31 (1990) 285–299.

[35] Y. Kohsaka, Stability analysis of Delaunay surfaces as steady states for the surface diffusion equation, in: Geometric properties for parabolic and elliptic PDE's, volume 176 of *Springer Proc. Math. Stat.*, Springer, [Cham], 2016, pp. 121–148.

[36] E. Kuwert, R. Schätzle, Gradient flow for the Willmore functional, Comm. Anal. Geom. 10 (2002) 307–339.

[37] F.C. Marques, A. Neves, Min-max theory and the Willmore conjecture, Ann. of Math. 179 (2014) 683–782.

[38] U.F. Mayer, G. Simonett, A numerical scheme for axisymmetric solutions of curvature-driven free boundary problems, with applications to the Willmore flow, Interfaces Free Bound. 4 (2002) 89–109.

[39] W.W. Mullins, Theory of thermal grooving, J. Appl. Phys. 28 (1957) 333–339.

[40] F.A. Nichols, On the spheroidization of rod-shaped particles of finite length, J. Mater. Sci. 11 (1976) 1077–1082.

[41] F.A. Nichols, W.W. Mullins, Morphological changes of a surface of revolution due to capillarity-induced surface diffusion, J. Appl. Phys. 36 (1965) 1826–1835.

[42] U. Seifert, Configurations of fluid membranes and vesicles, Adv. Phys. 46 (1997) 13–137.

[43] G. Simonett, The Willmore flow near spheres, Differential Integral Equations 14 (2001) 1005–1014.

[44] K. Sudoh, R. Hiruta, H. Kuribayashi, Shape evolution of high aspect ratio holes on Si(001) during hydrogen annealing, J. Appl. Phys. 114 (2013) 183512.

[45] J.E. Taylor, J.W. Cahn, Linking anisotropic sharp and diffuse surface motion laws via gradient flows, J. Statist. Phys. 77 (1994) 183–197.

[46] T.J. Willmore, Note on embedded surfaces, An. Şti. Univ. "Al. I. Cuza" Iaşi Secţ. I a Mat. (N. S.) 11B (1965) 493–496.

[47] Q. Zhao, A sharp-interface model and its numerical approximation for solid-state dewetting with axisymmetric geometry, 2017. `http://arxiv.org/abs/1711.02402`.